UNIVERSITÀ DI PISA

RESERCH DOCTORATE IN BIOMATERIALS
XIX Cycle (2004–2006)

Ph.D. Thesis

Characterization of Biomaterials by Atomic Force Microscopy

Candidate: Dr. Michele Alderighi

Supervisors: Prof. Roberto Solaro
University of Pisa – Italy

Prof. Maria Allegrini
University of Pisa – Italy

– May 2007 –

ACKNOWLEDGMENTS

I would like to thank prof. Emo Chiellini for the possibility he gave me to participate in the Bios school for Biomaterials. He involved me in a new exciting research group in which I was received with enthusiasm. For this reason I want to acknowledge also other people responsible for the Bios course: in particular prof. Galli and prof. Maria Rosaria Tinè, whose discussions about block polymers and peptides were very helpful to me in the draft preparation. I want to express all my gratitude to prof. Solaro who assisted me in every situation from the beginning, when the lab and also the AFM microscope were not yet present in the Chemistry Department, until the end of the period of the doctorate school. He always sustained me with precious information and fruitful discussions about any kind of experimental and fundamental issues. I would also like to mention prof. Allegrini from Physics department with whom I have maintained a strong and fruitful collaboration during all my Ph.D. studies. She suggested new lines of research for my Ph.D. work and provided fundamental advices for the choice and the operation of the microscope. Moreover prof. Fuso was always available for discussions about the experiments I was carrying out. He could not even realize how much I have learned from him. I'm particularly grateful to prof. Ciulli and prof. Bassani of the Engineering Department who provided me with the special steel samples and let me enter the fascinating field of tribology and mechanical properties of engineering materials.

Naturally I spent three years of my life here in the Chemistry department and I met a lot of people: first of all my colleague and friend Vincenzo Ierardi with whom I used to share rage when the system didn't properly function, but also satisfaction in successful experiments (I refer to pasta with sardella). Many thanks also to mrs. Celia Duce for the peptide samples, but above all for the pleasant coffee breaks which helped scientific researches.

I would like to thank all the people of the biomaterials school and the Chemistry department including Matteo, Laura, Dario, Elisa, Sara, Antonella and of course Maria Viola. Many kindly regards also to the buddies from physics department: I would like to mention Carlo, Donatella, Alessandro, Francesco, Antonio, Andrea and everybody who helped me in those fantastic years.

Now it's the moment to express my friendship to all my high school mates including Cappels (where are you?) Drago (lost in Varese), Dome (Rammstein), Tommy (El Toro), Maya (Pearl Jam supporter), Benetz (Gioielleria bxxxtti alè), Burghy (let's go for a dinner in Sarzana) Lenzo the future bridegroom, and the other pals from Pisa like Bale dj, Matteo, Leo, Pelo etc (sorry if I forget someone).

A special thanks to the friends of my childhood Luca and Renzo with whom I've shared a lot of happy-go-lucky moments.

Last but not least a kiss to my beloved Giulia who is very precious to me and represents a shiny light in dark moments. A sincere regard to all my relatives including my uncles, the old tata and of course my cousin (the carps cacher). Finally I want to express my gratitude to my parents that have supported me in all I have done and for their guidance in the long road of life.

The financial support by PRIN and FIRB MIUR programs is gratefully acknowledged.

Summary

Atomic force microscopy (AFM) is a very promising and powerful tool for investigating biological materials. A commercial AFM instrument was used to investigate different kinds of soft biomaterials such as oligopeptides, organic polymers, and proteins as well some hard materials, such as silicon and metals. The AFM consists of a microsized cantilever with a sharp tip (probe) at its end that is used to scan the specimen surface. The cantilever is typically made of silicon or silicon nitride with a tip radius of curvature on the order of few nanometres. When the tip is brought into proximity of a sample surface, forces between the tip and the sample lead to a relatively small deflection of the cantilever ruled by Hooke's law. Forces that are measured in AFM include mechanical contact force, Van der Waals forces, capillary forces, chemical bonding, electrostatic forces, and so on. Traditionally, the sample is mounted on a piezoelectric scanner that can move the object under examination in the z direction for maintaining a constant force, and in the x and y directions for scanning the sample. Surface images are obtained by mechanically moving the probe in a raster scan over the specimen (or the other way round), line by line, and recording the probe–surface interaction as a function of position. Although this is the typical AFM operating mode, there are several more exotic techniques, which have been implemented and used during this research. In particular, the present thesis was focused on four main research lines: installation and set up of a new AFM instrument, phase imaging, mechanical characterization of materials, and chemical force microscopy.

The first task was aimed at the selection and installation of a new AFM instrument. Accordingly a Nanoscope IV Veeco AFM was purchased and installed at the Department of Chemistry and Industrial Chemistry of the University of Pisa. The AFM was equipped with a cell for measurements in liquid, variable temperature and PicoForce modules. All modules were set up and thoroughly tested.

The second topic entailed the characterization of selected oligopeptides that self–aggregate to give different complex structures depending on the concentration and the composition of the starting solution. Indeed, the AFM, developed first to explore atomic details of hard materials, has evolved to an imaging method capable of achieving fine structural details on biological samples and soft matter. The measurements were performed in the so–called “tapping mode” which is capable of acquiring both morphological and phase maps. This mode is a powerful extension of AFM that provides nanometre–scale information about surface structure and properties often not readily

available by conventional techniques. In phase imaging, the phase lag of the cantilever oscillation, relative to the drive signal, is simultaneously monitored with topography data. The phase lag is very sensitive to variations in several material properties such as viscoelastic properties and this allows for instance for a precise determination of the presence and features of organic materials.

These measurements gave information on the dependence of oligopeptide aggregate size and shape from both the peptide structure and concentration. Basically, both the mean size and the dispersion of aggregates increased on increasing the oligopeptide concentration. A similar behaviour was found also for peptide samples prepared from buffer solution. However, in this case the size distribution was quite narrow. For a better understanding of the aggregation process it would be interesting to monitor the dynamics of peptide aggregation during solvent casting and to make more measurements of samples from solution at different concentration.

Investigation of the mechanical properties of materials constituted the third objective of the present research. Tissues are a challenging class of materials as they are composed in hierarchical structures with important features down to the nanometre scale. A technique that can probe mechanical properties at these scales has the potential to answer numerous questions that are relevant in the field of nanotribology and nanomechanics. In this respect, nanoindentation is particularly appealing. Nanoindentation, also known as depth sensing indentation (DSI), involves the application of a controlled load over the surface to induce local deformations. Load and displacement are monitored during the loading–unloading curves enabling the calculation of the mechanical properties of interest. Continuing developments in indentation data models and analysis will increase the usefulness of this method for the characterisation of biomaterials and in particular for tissue regeneration. In the development of the present investigation, different materials including poly(methyl methacrylate), polystyrene, silicon, gold, and Balinit, a very hard material used as antiwear coating in special engines, were tested. These measurements gave information of two of the most important mechanical properties, i.e. the hardness and the Young modulus, at the nanoscale. In order to get a better understanding of phenomena involved during the indentation process, several theoretical models were considered and new ones were developed. Moreover, in–depth studies allowed for investigating other important mechanical features, such as stiffness and the dependence of hardness on indentation depth. However, the experimental results are not yet fully understood because of the large variety of theories and methods of data analysis. The instrument data distortion and the different material response to indentation must be also taken into proper account.

In the last research topic, chemical force microscopy was exploited to monitor the forces involved in protein swelling experiments. Indeed, the potential of AFM to reveal ultra low forces at high lateral resolution has opened an exciting way for measuring inter and intra molecular forces at the single molecule level. The idea is to detect and study the binding of ligands on tips to surface–bound receptors by applying an increasing force to the complex that reduces its lifetime until it dissociates at a measurable unbinding force. Accordingly, the behaviour of human serum albumin was tested by linking the protein to both the AFM tip and functionalized silicon surface. Several measurements were collected in order to gather statistically significant data. The loading–unloading curves presented two sequential steps that were attributed to the detachment of the protein from the surface and to albumin uncoiling, respectively.

TABLE OF CONTENTS

1. INTRODUCTION

1.1. BIOMATERIALS

In the last years biomaterials science has become a new promising research area due to its particular connection with several important disciplines such as engineering, medicine, molecular and cell biology and other key research fields as tissue replacement and/or regeneration. The increasing knowledge and development of these fields, and the constant demand for new products have driven the biomaterials science to be one of the most exciting and promising areas of scientific and technological interest.

Biomaterial research area is rather varied and complex and hence it is not easy to formulate an adequate and unique definition that can cover the entire concept of biomaterials. In general, biomaterials are naturals or synthetic materials. Therefore, during the last years different definitions have been developed and accepted. The two most wise and correct definitions are reported below:

- *A biomaterial is a nonviable material used in a medical device, intended to interact with biological systems.*[1]
- *A biomaterial is a material intended to interface with biological systems to evaluate, treat, augment or replace any tissue, organ or function of the body.*[2]

By taking into account those two definitions, a large variety of materials can be considered biomaterials, including all natural or synthetic materials that are applied in biological environments. They comprise a large variety of materials such as metals, ceramics composites, and natural or synthetic polymers. Indeed, besides natural materials like collagen or cellulose, synthetic polymers have been increasingly designed and used as a biomaterials, due to the possibility of attaining a wide range of chemical, physical, and mechanical properties by structure modulation.

According to a general classification, the previous groups can be categorized as based on the chemical nature of biomaterials:

- **Biologically derived materials** include naturally occurring proteins (collagen, elastin, gelatine), polysaccharides (hyaluronic acid, chitosan, dextran, cellulose), and proteins produced with biotechnological techniques (genetic engineering), as well as entire cells and natural tissues amongst others. They are often used in combination with other synthetic biomaterials, especially in dermatology.

- **Synthetic polymers** can be employed in a wide range of applications, either intracorporeal or extracorporeal. The most common uses include short–term devices (sutures, adhesives, artificial tendons, and contact lenses), long–term cardiac valves, complex systems aimed at substituting the function of body organs (such as artificial kidney, heart, pancreas), catheters, filters for haemodialysis, orthopaedic material, and drug delivery devices.
- **Metals** are mainly used in orthopaedic and dental implants, and in the production of pacemakers and heart valves. The most commonly used metals are stainless steel, cobalt–based alloys, titanium and its alloys.
- **Composites** can be manufactured by the combination of polymers, ceramics, and metals. Composites currently used in biomaterial applications include reinforced methyl methacrylate bone cement with bone particle or carbon fibres–and ultra–high–molecular–weight polyethylene, porous surface orthopaedic implants, and dental filling composites.
- **Ceramics** are widely employed in orthopaedic implants, as bone fillers, and in dental and ear–nose–throat implants. The most common bioceramics are aluminium oxides, calcium phosphates, titanium oxides, zirconium oxides, and glass–ceramics.

A lot of features have to be satisfied for the design and the production of those materials. In particular, a deep investigation of the chemical and of the biological characteristics of the environment in which the material is expected to perform its action is of utmost importance. Indeed, this knowledge may allow for a better understanding of the main factors that determine the final performances of materials, therefore allowing for the optimization of their design.

The fundamental characteristic of biomaterials is their capabilities of interacting with organic issues and biological fluids without inducing alterations or damaging processes to the living organism where they are placed. From a more restrictive point of view, when placed in contact with a tissue or organ, biomaterials should not cause toxic, inflammatory, or carcinogenic responses (biocompatible) and their interactions with blood should not elicit coagulative or cell–disruptive activities (hemocompatible). Until the 1970's, the term "biocompatibility" was related to the biological inertness of the material, since an inert material does not interact chemically with the biologically tissues it comes into contact with, and develops no reaction capable of compromising the life of the implant and the health of the biological environment. At present, the concept of inertia is questionable because there is no material that does not elicit a response when in contact with body compartments. Moreover, with the improvements in material technology and instrumentation, particular materials have appeared on the scientific horizon that can degrade in the biological tissues and whose degradation products can interact “positively” with the living cells and their metabolism, thus bringing about favourable biological reactions for the implant life and its functionality. Accordingly, there is now a general agreement in defining a biomaterial as “*a material that has suitable characteristics for its intended application and that elicits specific interactions with the tissues it is in contact with*”.

1.2. MOLECULAR SELF–ASSEMBLY

Self–assembly is ubiquitous in nature at both macroscopic and microscopic scales, for example, from assembly of schools of fish in the ocean, flocks of birds in the sky, herds of wild animals to oil droplets in water. Self–assembly describes the spontaneous association of numerous individual entities into a coherent organization and well–defined structures to maximize the benefit of the individual without external instruction.

Molecular self–assembly, by definition, is the spontaneous organization of molecules under thermodynamic equilibrium conditions into structurally well–defined and rather stable arrangements through a number of non–covalent interactions.[3] These molecules undergo self–association forming hierarchical structures. The key engineering principle for molecular self–assembly is to artfully design the molecular building blocks that are able to undergo spontaneously stepwise interactions and assemblies through the formations of numerous non–covalent weak chemical bonds. These typically include hydrogen bonds, ionic bonds and van der Waals' bonds[4] to assemble these molecules into some well–defined and stable hierarchical macroscopic structures. Although each of the bonds is rather weak, the collective interactions can result in very stable structures and materials. The key elements in molecular self–assembly are chemical complementarity and structural compatibility.

1.2.1. Molecular self–assembly in nature

Biomimicry and designing nature–inspired materials through molecular self–assembly is an emerging field in the coming years of the 21st century. Nature is a grand master at designing chemically complementary and structurally compatible constituents for molecular self–assembly through eons of molecular selection and evolution. Chemical evolution from the first groups of primitive molecules through countless iterations of molecular self–assembly and disassembly has ultimately produced more and more complex molecular systems.

In the last decade, considerable advances have been made in the use of peptides, phospholipids, and DNA as building blocks to produce potential biological materials for a wide range of applications.[5] The constituents of biological origins, such as phospholipids, amino acids, and nucleotides have not been generally considered to be useful materials for traditional material science and engineering. The advent of biotechnology and genetic engineering coupled with the recent advancement in chemistry of nucleic acids and peptide syntheses has resulted in a conceptual change. Molecular self–assembly is emerging as a new route to produce novel materials and to complement other materials, i.e. ceramics, metals and alloys, synthetic polymers and other composite materials. Several recent discoveries and rapid developments in biotechnology, however, have rekindled the field of biological materials engineering.[6]

There are ample examples of molecular self–assembly in nature. One of the well–known examples is the silk assembly. The monomeric silk fibroin protein is approximately 1 μm but a single silkworm can spin fibroins into silk materials over 2 km in length, two billion times longer.[7,8] Likewise, spiders are grand master materials engineers who can produce many types of spider silks through self–assembly of the building blocks in a variety of ways, thus, producing spider silk fibre with tremendous strength and flexibility. The power of molecular self–assembly can never be underestimated. Molecular self–assembly can also build sophisticated structures and materials. For example, collagen and keratin can self–assemble into ligaments and hair, respectively. In cells, many individual chaperone proteins assembly into a well–defined ring structure to sort out, fold, and refold proteins.[9] The same is true for other protein systems, such as seashell biomineralization.[10,11] Likewise, mammals build their teeth through self–assembly of a protein scaffold that is made of many individual proteins first and recruit calcium ions to the sites for biomineralization.

1.2.2. Self–assembling peptide systems

A new class of peptide–based biological materials was serendipitously discovered in yeast from the self–assembly of ionic self–complementary peptides.[12] A number of peptide molecular self–assembly systems have been designed and developed. This class of biological materials has considerable potential for a number of applications, including scaffolding for tissue repair and tissue engineering, drug delivery of molecular medicine, as well as biological surface engineering. Similar systems have also been described wherein these peptide systems undergo self–assembly to form gel with regular beta sheet tapes of well–defined structures.[13,14] The self–assembly of peptide nanotubes that allow ions to pass through and to insert themselves into lipid bilayer membranes was also described[15,16]). Furthermore, a number of fascinating biomimetic peptide and protein structures have been engineered, such as helical coil–coils, di–, tri– and tetrahelical bundles.[17,18] However, their applications for materials science and engineering remain under explored.

1.2.2.1. Type I self–assembling peptides

Type I peptides, also called “molecular Lego”, form beta sheet structures in aqueous solution because they contain two distinct surfaces, one hydrophilic, and the other one hydrophobic. Like Lego bricks that have pegs and holes and can only be assembled into particular structures, these peptides can do so at the molecular level. The unique structural feature of these peptides is that they form complementary ionic bonds with regular repeats on the hydrophilic surface.[19] The complementary ionic sides have been classified into several modules, i.e. modulus I, II, III, IV, *etc.*, and mixed modules. This classification is based on the hydrophilic surface of the molecules that have alternating + and – charged amino acid residues. For example, molecules of modulus I have – + – + – + – +, modulus II, – – + + – – + +, modulus, IV – – – –+ + + +. These well–defined sequences allow them to undergo ordered self–assembly, resemblance of some situation found in well–studied polymer assemblies.

In physiological media, these oligopeptides spontaneously assemble to form microscopic and macroscopic structures (Fig. 1) that can be fabricated into various geometric shapes.[20,21] SEM and AFM reveals that the matrices are made of interwoven nanofibres having 10–20 nm in diameter and pores about 50–200 nm in diameter.[22]

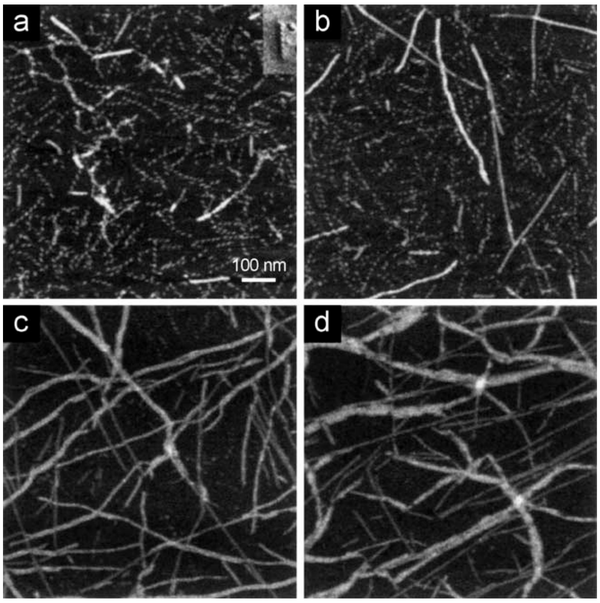

Fig. 1 – AFM images of intermediate structures in the self–assembly of KFE8 in aqueous solution at different times after preparation of the solution. (a) After 8 min; (b) 35 min after preparation; (c) 2 h; (d) 30 h.[5]

A number of mammalian cell types have been tested and all have been found to form stable attachments with the peptide materials.[20] Several peptide materials have been used to test for their ability to support cell proliferation and differentiation. These results suggested that the peptide materials cannot only support various types of cells attachments, but can also allow the attached cells to proliferate and differentiate.

1.2.2.2. Type II self–assembling peptides

Several Type II peptides have been developed as "Molecular Switches" in which the peptides could drastically change their molecular structure (Fig. 2). One of the peptides with 16 amino acids has a beta–sheet structure at ambient temperature with 5 nm in length but can undergo an abrupt structural transition at high temperatures to form a stable alpha–helical structure with 2.5 nm length.[23,24] Similar structural transformations can be induced by changes of pH. This suggests that secondary structures of some sequences, especially flanked by clusters of negative charges on the N–terminus and positive charges on the C–terminus, may undergo drastic conformational transformations under the appropriate conditions. These findings cannot only provide insights into protein–protein interactions during protein folding and the pathogenesis of some protein conformational disease, including scrapie, prion, kuru, Huntington's, Parkinson's, and Alzheimer's diseases, but can also be developed as molecular switches for a new generation of nanoactuators and nanoswitches.

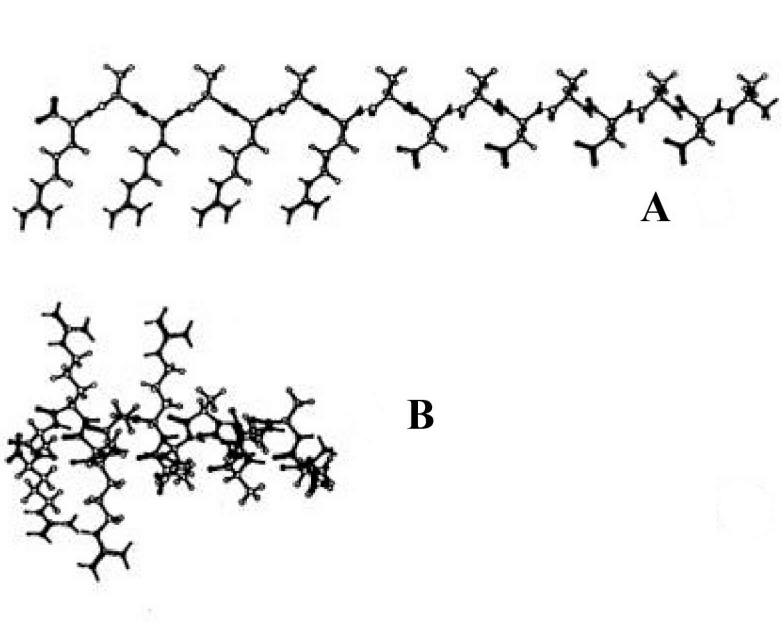

Fig. 2– Type II peptides. Temperature effect on DAR16–IV structural transition. (A) Structures of DAR16–IV* at 25 °C. (B) DAR16–IV at 90 °C.*

1.2.2.3. Type III self–assembling peptides

Type III peptides, like "Molecular Paint" and "Molecular Velcro" undergo self–assembly onto surfaces rather with among themselves. They form monolayers on surfaces for specific cell pattern formations or to interact with other molecules. These peptides have three distinct features. The first feature is the terminal segment of ligands that incorporate a variety of functional groups for recognition by other molecules or cells. The second feature is the central linker where a variable spacer is not only used to allow freedom of interaction at a specified distance away from the surface but also rules the flexibility or rigidity. The third feature is the surface anchor where a chemical group on the peptide can react with the surface to form a covalent bond.

This simple system using Type III self–assembling peptides and other substances to engineer surfaces is an emerging technology that will be a useful tool in biomedical engineering and biology. This biological surface engineering technique will provide new methods to study cell–cell communication and cell behaviour.[25] Similar kinds of molecular self–assembly systems, through incorporating a segment of organic linker for surface anchoring, have been developed.[26]

1.2.2.4. Type IV self–assembling peptides

Several surfactant–like peptides undergo self–assembly to form nanotubes and nanovesicles having an average diameter of 30–50 nm.[27] Dynamic light scattering studies showed structures with very discrete size. The structures showed some tail sequence preference. The distribution becomes broader over time, indicating a very dynamic process of assembly and disassembly. Imaging with transmission electron microscopy of quick–freeze/deep–etch sample preparation revealed a network of open–ended nanotubes with a helical twist (Fig. 3). Many three–way junctions that may act as links between the nanotubes have also been observed (Fig. 4). Studies of peptide surfactant molecules have significant implications in the design of non–lipid biological surfactants and understanding the complexity and dynamics of self–assembly processes.

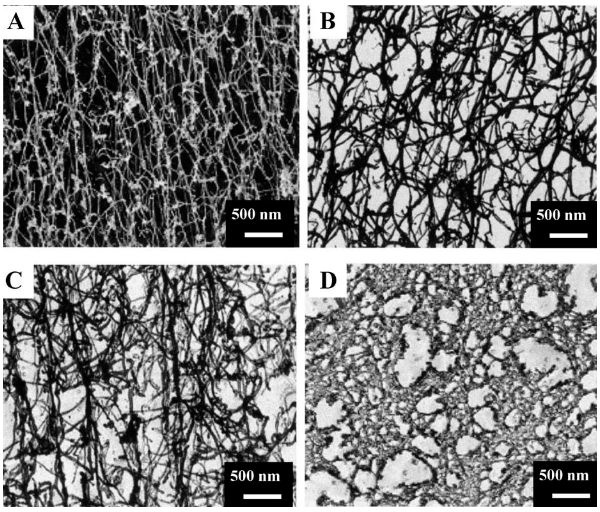

Fig. 3 – Quick–freeze/deep–etch TEM images of surfactant peptides in water: (A) A_6D, (B) V_6D, (C) V_6D_2, and (D) L_6D_2. Bar is 500 nm (see ref. 27).

These surfactant peptide monomers contain seven to eight amino acid residues and have a hydrophilic head composed of aspartic acid and a tail of hydrophobic amino acids, such as alanine, valine or leucine. The length of each peptide is approximately 2 nm, similar to that of biological phospholipids. There are molecular and chemical similarities between lipids and the peptides since both have a hydrophilic head and a hydrophobic tail. The packing between lipids and peptides are likely to be quite different, however. In lipids, the hydrophobic tails pack tightly against each other to completely displace water, precluding the formation of hydrogen bonds. On the other hand, in addition to hydrophobic tail packing between the amino acid side chains, surfactant peptides may also interact through intermolecular hydrogen bonds along the backbone.

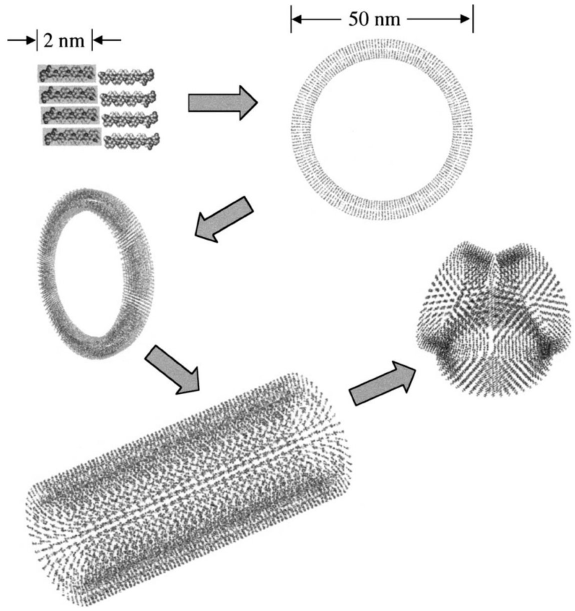

Fig. 4 – Potential packing pathway of V_6D peptide nanotube formation. Each peptide monomer is 2 nm, and the diameter of the modelled bilayer nanotube is 50 nm. Each peptide may interact with one another to form a closed ring, which in turn would stack upon top of one another, ultimately yielding a nanotube. Three nanotubes are connected to each other through a three–way junction.

1.2.2.5. Additional self–assembling peptide systems

Several other types of self–assembling peptide systems are currently being developed as emerging materials. In one of these systems, part of the peptide binds to and condenses nucleic acids; the other parts facilitate membrane trafficking to translocate them across the cellular lipid membranes.[28] This system will likely have applications for delivery of molecular drugs, including DNA and RNA for gene therapy, as well as protein therapy and delivery of other therapeutics. The other system is aimed to produce new biological scaffolding material to facilitate biomineralization.[29] In such a system, the material has a peptide and a polymer segment. The peptide is negatively charged with a molecular recognition site and the polymer is a hydrophobic tail. The hydrophobic segments of the chain in aqueous solutions can self–assemble into regular intersections of the scaffold, much like the joints in the construction of buildings; therefore forming negatively charged compartments. These negative compartments can then attract the positively charged ions, thus building the mineral phases.

1.3. BIOMATERIAL CHARACTERISATION BY ATOMIC FORCE MICROSCOPY

Nanoscale sciences and techniques are strongly driven by scanning probe microscopy (SPM), which allow for the investigation and manipulation of surfaces down to the atomic scale. Atomic force microscopy (AFM) is a powerful tool to study surfaces properties of different materials at very small scales. This technique was born in 1985 [32] as a logical consequence of the scanning tunnelling microscopy (STM) that can be addressed only to conductive or semi–conductive materials. With AFM it was possible for the first time to observe also dielectric samples with a very good spatial resolution. This technique is now widely used since it does not require conductive specimens and it is suitable for almost all kind of surfaces. Particularly interesting is the study of biological materials that can be analyzed also in their physiological environment such as water and other biological fluids.

The atomic force microscope consists of a microsized cantilever with a sharp tip (probe) at its end that is used to scan the specimen surface. The cantilever is typically made of silicon or silicon nitride with a tip radius of curvature on the order of few nanometres. When the tip is brought into proximity of a sample surface, forces between the tip and the sample lead to a deflection of the cantilever ruled by Hooke's law. Depending on the situation, forces that are measured in AFM include mechanical contact force, Van der Waals forces, capillary forces, chemical bonding, electrostatic forces, *etc*. Typically, the sample is mounted on a piezoelectric scanner that can move the object under examination in the z direction for maintaining a constant force, and in the x and y directions for scanning the sample. An image of the surface is obtained by mechanically moving the probe in a raster scan (that is the pattern of image detection and reconstruction in a computer image) over the specimen, line–by–line, and recording the probe–surface interaction as a function of the probe position relative to the sample surface.

The AFM can operate in a number of modes, depending on the application. In general, possible imaging modes are divided into static (also called contact) modes and a variety of dynamic modes.

The primary modes of operation are static (contact) mode and dynamic tapping mode. In the static mode operation, the static tip deflection is used as a feedback signal. Because the measurement of a static signal is prone to noise and thermal drift, low stiffness cantilevers are used to boost the deflection signal. However, close to the surface of the sample, attractive forces can be quite strong, causing the tip to 'snap–in' to the surface. Thus static mode AFM is almost always done in contact (few Ångstroms from the tip to the surface) where the overall force is repulsive. Consequently, this technique is typically called 'contact mode'. In contact mode, the force between the tip and the surface is kept constant during scanning by maintaining a constant deflection.

In the dynamic mode, the cantilever is externally oscillated at or close to its mechanical resonance frequency. The oscillation amplitude, phase, and resonance frequency are modified by tip–sample interaction forces; these changes in oscillation with respect to the external reference oscillation provide information about interaction forces, hence on the sample characteristics. Schemes for dynamic mode operation include frequency modulation and the more common amplitude modulation. In frequency modulation, changes in the oscillation frequency due to damping forces provide information about tip–sample interactions. Frequency can be measured with very high sensitivity and thus the frequency modulation mode allows for the use of very stiff cantilevers (which provide a high resonant frequency allowing for fast scan). Stiff cantilevers provide stability very close to the surface and, as a result, this technique was the first AFM technique to provide true atomic resolution in ultra–high vacuum conditions.[30]

AFM is a versatile tool for true mapping and morphology recreation of the structure of specimens under examination. Several AFM techniques have been exploited. Some of these became standard routine in the last decade, while others are more complicated and still require a careful attention in the preparation of samples and data analysis.

Surface imaging is of great help in understanding the shape and more in detail the spatial conformation of particular biological systems, such as proteins, DNA, polymers, and other types of macromolecules. This methodology allows for investigating the conformation and the shape of particular biomolecules, such as, oligopeptides that can aggregate in different shapes and morphologies depending on their structural features and on the concentration of the starting solutions from which they were prepared.

Phase imaging is a powerful extension of AFM that provides nanometre–scale information about surface structures and properties not often revealed by traditional techniques. For this reason, it is a very common technique that is widely used in a large variety of experiments. By mapping the phase of the cantilever oscillation during the tapping mode scan (a common operation mode in which the cantilever is mechanically excited to vibrate either at or close to its resonant frequency), phase imaging goes beyond simple topographical mapping to detect variations in chemical composition, adhesion, and other properties involved in energy dissipation between the tip and the sample. In tapping mode AFM, the cantilever is excited into resonance oscillation by a piezoelectric driver. The oscillation amplitude is used as a feedback signal to measure topographic variations of the sample. In phase imaging, the phase lag of the cantilever oscillation, relative to the drive signal, is simultaneously monitored with topography data. The phase lag is very sensitive to variations in many material properties. The resolution of the phase imaging is comparable to the full resolution of tapping mode AFM. Moreover, phase imaging can also act as a real–time contrast enhancement technique. Phase imaging highlights edges and it is not affected by large–scale height differences. Therefore, it provides clearer observation of fine features, such as grain edges, which can be obscured by a rough topography. The AFM, developed first to explore atomic details on hard materials, has evolved to an imaging method capable of achieving fine structural details of biological samples and soft matter. Its particular advantage in biochemistry is that the measurements can be carried out in liquid environments.

Chemical force microscopy is a technique used especially in molecular swelling experiments. The potential of AFM to reveal ultra low forces at high lateral resolution has opened an exciting way for measuring inter– and intra–molecular forces at a single molecule level. Molecular recognition AFM studies have opened the possibility to detect specific ligand–receptor forces and the processes involved in polymers and proteins swelling. AFM is widely used in fundamental research, although it, like other scanning probe microscopes, provided only limited information about the chemical nature of the investigated systems. Modification of force microscope probe tips by covalent linking of organic molecules that terminate with well–defined functional groups enables direct probing of molecular interactions and imaging with chemical sensitivity. This new chemical force microscopy technique has been used to probe adhesion between distinct chemical groups in organic and aqueous solvents.

1.4. AIM OF THE THESIS

The main goal of the present thesis is to exploit the application of several AFM techniques to the characterization of materials of biomedical interest. Some of the selected methods became standard routine in the last decade, while others are more complicated and still require careful attention in sample preparation, experimental set up, and data analysis.

The investigation addressed in this thesis will entail three main research topics:

- surface imaging
- mechanical analysis of materials
- chemical force microscopy

The first research line is aimed at investigating self–assembling oligopeptides. AFM is a versatile tool for the real mapping and morphology recreation of the structure of specimens under examination. The surface image is of great help in understanding the shape and more in detail the spatial conformation of particular biological systems, such as proteins, DNA, polymers, and other types of macromolecules. This methodology allows for investigating the conformation and the shape of particular biomolecules, such as, oligopeptides that can aggregate in different shapes and morphologies depending on their structural features and on the concentration of the starting solutions from which they were prepared. Investigation of oligopeptide aggregates will be performed not only by morphology but also by phase imaging, which is a powerful extension of AFM that provides nanometre–scale information about surface structures and properties not often revealed by traditional techniques. In phase imaging, the phase lag of the cantilever oscillation, relative to the drive signal, is very sensitive to variations in many material properties. By mapping the phase of the cantilever oscillation during the tapping mode scan, phase imaging goes beyond simple topographical mapping to detect variations in chemical composition, adhesion, and other properties involved in energy dissipation between the tip and the sample. The resolution of the phase imaging is comparable to the full resolution of tapping mode AFM. Moreover, phase imaging can also act as a real–time contrast enhancement technique. Phase imaging highlights edges and it is not affected by large–scale height differences. Therefore, it provides clearer observation of fine features, such as grain edges, which can be obscured by a rough topography.

The second research line is of aimed at the mechanical characterization of materials. The objective of this study is to find a way to determine some of the most relevant properties in the field of nanomechanics, such as hardness, Young's modulus, and stiffness.

Mechanical characterization of tissues and other biological material is of outmost significance in the field of clinical medicine and biomaterials. Tissues are a challenging class of materials as they are composed in hierarchical structures with important features down to the nanometre scale. Continuing developments in indentation data model and analysis can increase the usefulness of the method for the characterisation of biomaterials, in particular for tissue regeneration. The nanoindentation, also known as depth sensing indentation (DSI), involves the application of a controlled load over the surface to induce local deformations. Load and displacement are monitored during the loading–unloading process thus enabling the evaluation of the mechanical properties of interested. Some theoretical models will be considered and new ones will be developed in order to get a better understanding of the phenomena involved during the indentation process. A technique that can probe mechanical properties at nanometre scale has the potential to answer several questions that are relevant to the field of nanotribology and nanomechanics.

The last topic deals with chemical force microscopy, a technique used especially in molecular swelling experiments. The potential of AFM to reveal ultra low forces at high lateral resolution has opened an exciting way for measuring inter– and intra–molecular forces at a single molecule level. Molecular recognition AFM studies have opened the possibility to detect specific ligand–receptor forces and the processes involved in polymers and proteins swelling. AFM is widely used in fundamental research, although it, like other scanning probe microscopes, provided only limited information about the chemical nature of the investigated systems. Modification of force microscope probe tips by covalent linking of organic molecules that terminate with well–defined functional groups enables direct probing of molecular interactions and imaging with chemical sensitivity. This new chemical force microscopy technique has been used to probe adhesion between distinct chemical groups in organic and aqueous solvents.

The thesis is divided into five chapters, including the present one. The first chapter gives a quick overview of the entire work and explain the importance of probe microscopy in getting a deeper understanding of biological systems, with particular consideration of morphology, conformation, shape, and mechanical properties. The second chapter is devoted to the description of atomic force microscopy, by considering both theoretical aspects and technical details adopted in the selected commercial microscope. Detailed explanation is provided of the basic operation modes, the capabilities of the instrument to collect different kinds of data that can be used to find heterogeneous properties of the samples under investigation. The third chapter provides a details description of the performed experiments, including environmental conditions, microscope settings, and so on. The fourth chapter reports a discussion of the obtained results, whereas the fifth and final chapter is dedicated to the concluding remarks.

2. ATOMIC FORCE MICROSCOPY

2.1. INTRODUCTION

In the early 1980's, scanning probe microscopy dazzled the world with the first real–space images of the surface of silicon at atomic resolution.[31] The history of scanning probe microscopy was born with the scanning tunnelling microscope (STM) invented by Gerd Binnig and Heinrich Rohrer, who in 1986 have shared the Nobel Prize for their invention. In the same year of the awarded prize, a new microscope was developed:[32] the AFM was created in Quate's laboratory in Stanford thanks to the work of Binning, Quate, and Gerber. The above two microscopes are considered the archetypes of a large variety of SPMs. In fact, SPMs are used now in a wide variety of disciplines, including fundamental surface science, routine surface roughness analysis, and true three–dimensional imaging, from surface atoms to micron–sized protrusions on the surface of a living cell, measurement of magnetic, electric, and chemical forces, and so on.

Three parts essentially compose an AFM instrument:

- A piezoelectric scanner
- A probe which consist of very sharp tip (that could ends with only few atoms)
- An electronic system consisting of a computer that records signals and sets up the parameters for the experiments and a controller that is able to detect signals from the microscope, allows for the movement of the sample, realize the feedback, *etc.*

The scanner is used to move the sample in a raster scan under and in proximity (typically a few nanometres or even less) of the tip. The probe interacts physically with the sample; it provides information about the topography and the mechanical properties of the surface. It represents the "heart" of the system, whereas electronics are used for detecting the tip–sample interactions and for recording signals of interest.

In classical optical microscopy, the sample is observed in its whole entirety by a unique measurement: so every point of the sample is treated at the same time and in parallel with the others. On the contrary, in scanning probe microscopy the interested portion of the sample is analysed point by point with a measure that affects only locally the object under study. Basically, the idea behind such a microscope is, in general, to move the sample with a translator, on which the specimen lies while the probe fixed in space is used to make the measure. The translator is usually made of a piezoelectric material that could be a crystal, a polymer, or more commonly a ferroelectric ceramic. The most widely used geometry for the piezoelectric scanner is the hollow tube shape even if the use of linearised piezoelectric tablets is growing up and is gaining space.

The translator must be able to execute movements in the order of micrometers with a precision of at least a few Ångstroms. This actuating process is obtained by using the piezoelectric effect of the translator, which consists in the material controlled deformation by the application of an electric field. By applying a voltage varying between few mV to hundreds of V at the electrodes, it is possible to modify the geometry of the scanner in a precise and controlled way. Typically, the range of the piezo motion in the x–y plane is about dozens of microns, while in the z direction, the movement is limited to a few microns. The piezo movement is commonly called raster scan, because of characteristics probe walk shown in Fig. 5.

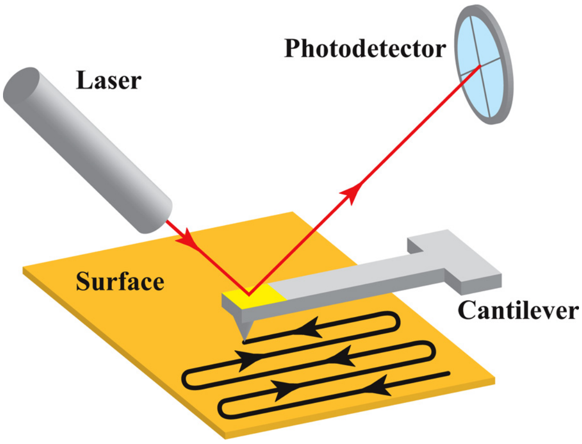

Fig. 5 – Schematic representation of raster scanning.

Measurements performed with piezoelectric materials are subjected to various kinds of distortions and it is very important to recognise those artefacts in order to avoid false conclusions. Common artefacts exist in almost all SPM techniques while other are specifically related to the type of probe utilized. The hysteretic behaviour typical of all ferroelectrics is the main drawback of using piezoelectric materials. In fact, some minor nuisances due to the hysteretic cycle of the material affect AFM measurements. Once the voltage is applied, inside the piezo there is a formation of permanent dipoles that maintain the polarization even in the absence of an applied potential. As a result, the geometry remains deformed. In order to minimize errors caused by the hysteresis, each line of the scan is sampled twice (forward and backward) and the piezo is previously calibrated by using a xy grid reference and a z step of known height. Further possibilities include software–based linearization, and the use of independent systems to evaluate the piezo displacement, for instance by capacitive or interferometric measurements.

Scanning probe microscopy studies surface properties via the physical interaction between the sample surface and the probe tip. The main difference between these families of microscopy techniques resides in the probe. For instance, in STM a conductive subnanometric tip is maintained at a constant voltage in respect to the sample surface that, as said before, must be conducting or semi conducting. When the tip is kept at a small distance (often less than one nanometre) from the surface, electrons can flow due to the tunnel effect. This flow is measured point by point during the scanning so that electronic surface properties can be reconstructed and information about the morphology can be gathered. In AFM instruments, on the contrary, the probe is used in contact or quasi–contact with the sample surface. In this way, it is possible to collect information on the repulsive force between the specimen surface and the apical atoms of the probe. More in general, the tip–sample interaction allows for rebuilding the distance between the two elements and the topography or a measure of the height of every single point analyzed during scanning can be acquired.

The tip of AFM instruments is generally micro integrated on an elastic lever called "cantilever". This element can have different shapes and elastic constants depending on the use it is made for. Most SPM works are done using cantilevered probes. These consist of a flexible cantilever extending from a rigid substrate, to which a tip has been attached or microfabricated. In contact AFM, the cantilever flexibility acts as a nanometric spring, allowing the tip to measure surface forces. In Tapping Mode, the probe is forced to swing up and down at its resonant frequency while oscillation amplitude and phase are monitored.

2.2. BRIEF DESCRIPTION OF AFM INSTRUMENT

A commercial atomic force microscope has been used in every experiment and analysis described in this thesis. The instrument is a Multimode microscope equipped with a Nanoscope IV Controller produced by Veeco Metrology (Santa Barbara, Ca –USA). As mentioned above different parts compose the microscope; Fig. 6 shows a scheme of the microscope body.

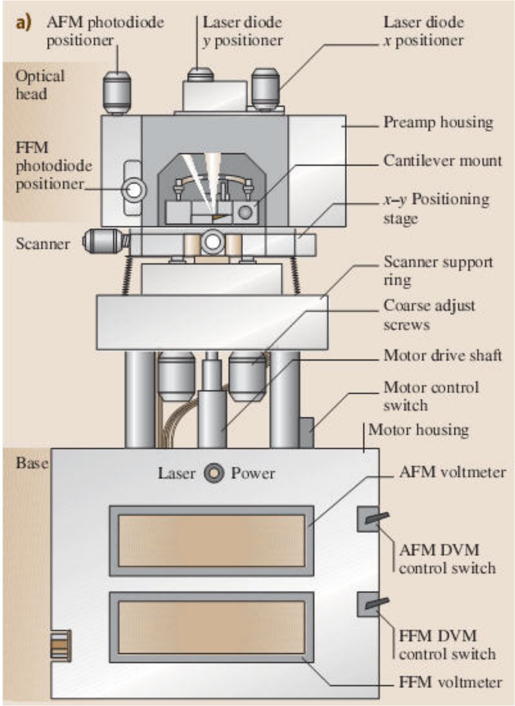

Fig. 6 – Basic scheme of Multimode IV AFM.

This AFM is based on the original design of Meyer and Amer.[33] It has a scanning range from about 0.7 μm (for atomic resolution) to about 125 μm. Basically the AFM scans the sample in a raster pattern while outputting the cantilever deflection signal to the control station. A probe tip is integrated in a microfabricated force–sensing cantilever. A variety of silicon and silicon nitride cantilevers are commercially available with micron–sized dimensions, spring constants ranging from 0.01 to 100N/m, and resonant frequencies ranging from 5 to over 400 kHz.

Acquisition of the AFM images of a surface topography is connected to the registration of small bends of the probe elastic cantilever. For this purpose optical methods (Fig. 7) are widely used in atomic force microscopy. The optical AFM system is aligned so that radiation of the semi–conductor laser is focused on the probe cantilever, and the reflected beam hits the centre of a photosensitive area of a photodetector. Four–section semi–conductor photodiodes are used as position–sensitive detectors (Fig. 7).

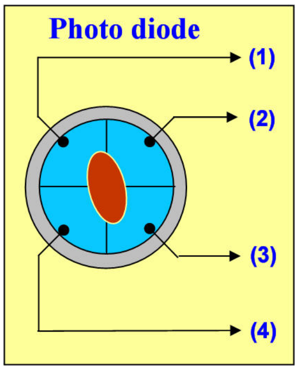

Fig. 7 – Schematic representation of a four–quadrant photodiode.

The cantilever deflection is detected by optical beam deflection, as illustrated in Fig. 8. A laser beam bounces off the back of the cantilever and, after reflection, is centred on a four quadrants photodiode. Cantilever deflections are proportional to the difference signal V_A–V_B measured by quadrants A and B of the photodiode, respectively. Sub–angstrom deflections can be detected and, therefore, forces down to tens of pico Newtons (pN) can be measured.

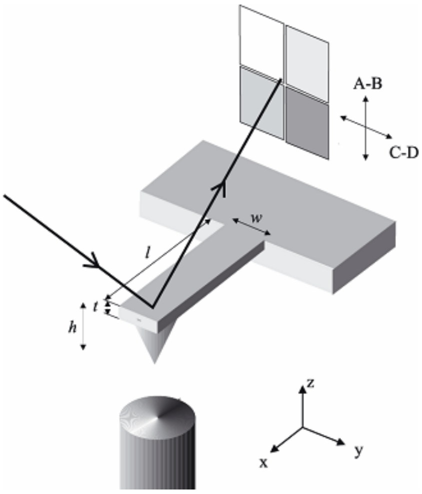

Fig. 8 – Schematic representation of the optical detection system for cantilever deflection.

A piezoelectric scanner rasterises the sample under the tip while the forces are measured through deflections of the cantilever. To achieve more controlled imaging conditions, a feedback loop, fed by duly conditioned photodiode output monitors the tip–sample force and adjusts the sample z–position to hold the force constant. The topographic image of the sample is then taken from the sampled z–position data. The mode described is called contact mode, in which the tip is deflected by the sample due to repulsion or "contact" forces. It is generally used only for flat samples that can withstand lateral forces during scanning.

To minimise lateral forces and sample damage, two AC modes have been developed. In these modes, the cantilever is driven into oscillation near its resonant frequency (tens to hundreds of kHz) with amplitudes of 5 to 10 Å. When the tip approaches the sample, the oscillation is damped, and the reduced amplitude becomes the feedback signal, rather than the DC deflection. Again, topography is taken from the varying z–position of the sample required to keep the tip oscillation amplitude constant. The two AC modes can be envisioned with a difference only in the nature of the interaction. In intermittent contact mode, also called tapping mode, the tip contacts the sample on each cycle, so that the amplitude is reduced by ionic repulsion as in contact mode. In non–contact mode, long–range van der Waals forces reduce the amplitude by effectively shifting the effective spring constant experienced by the tip and changing its resonant frequency.

The basic parameters registered by the optical system are the bending deformation of the cantilever under influence of z components of attraction or repulsion forces (F_Z) and deformations of cantilever torsion under influence of lateral components (F_L) of interaction forces of the tip with the surface. If the photocurrent reference values in the photodiode sections are designated as I_{01}, I_{02}, I_{03}, I_{04} and the photocurrent values after the change of cantilever position are I_1, I_2, I_3, I_4, then differential currents from various sections of the photodiode $\Delta I_i = I_i - I_{0i}$ will identically characterize the value and direction of the bend of the probe cantilever. In fact, the differential current:

$$\Delta I_Z = (\Delta I_1 + \Delta I_2) - (\Delta I_3 + \Delta I_4)$$

is proportional to the cantilever bend under influence of the force acting normally to the sample surface, and the combination of differential currents:

$$\Delta I_L = (\Delta I_1 + \Delta I_4) - (\Delta I_3 + \Delta I_2)$$

is proportional to the cantilever torsion under influence of lateral forces.

As already stated, the ΔI_Z value is used as an input parameter in the feedback loop of the atomic force microscope. This system provides $\Delta I_Z = const.$ (the constant value is set by the operator depending on experimental conditions) with the help of the piezoelectric actuating element, which controls the tip–sample distance and hence keeps the cantilever bend ΔI_Z equal to the reference value ΔI_{Z0} set by the operator. Fig. 9 presents a schematic representation of the microscope head with the laser pattern highlighted in orange several micrometer translators are used to steer the laser beam onto the cantilever and to focus the reflected beam onto the photodiode in order to achieve optimal performance. When scanning a sample in $\Delta z = const.$ mode, the tip moves along the surface, thus the voltage (proportional to height) of the scanner z–electrode is recorded by the electronics as a surface topography $z = f(x, y)$.

In atomic force microscopy, assessment of the resolution can be a rather complicated issue. As an initial approximation, resolution is often considered strictly in geometrical terms that assume rigid tip–sample contact. The topographical image of a feature is broadened or narrowed by the size of the probe tip, so the resolution is approximately the width of the tip. Accordingly, the resolution of AFM with standard commercially available tips is of the order of 5 to 10 nm (in contact mode topographical imaging).

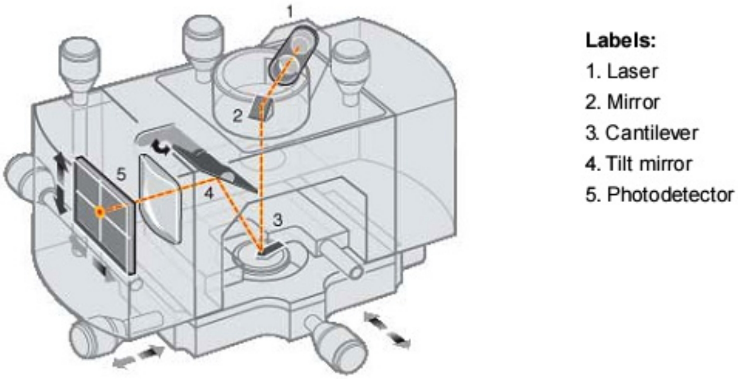

Fig. 9 – Basic scheme of the AFM head.

Bustamante and Keller[34] introduced a geometrical model by drawing an analogy with the resolution in optical systems. Consider two sharp spikes separated by a distance d to be point objects imaged by AFM (Fig. 10).

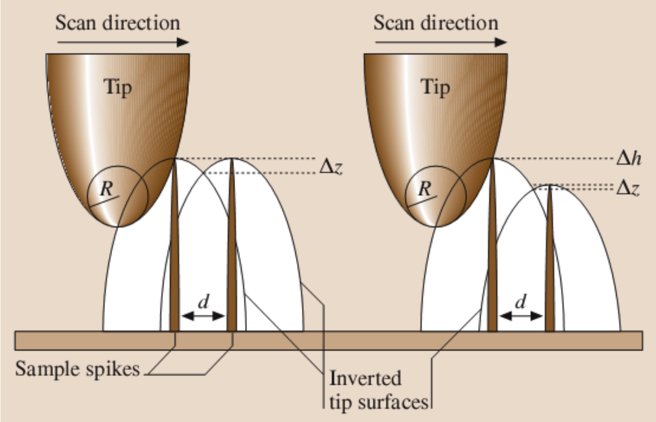

Fig. 10 – Factors that affects the AFM resolution in contact mode.

Assume the tip has a parabolic shape with an end radius R. The tip–broadened image of these spikes will appear as inverted parabolas. There will be a small depression between the images of depth z. The two spikes are considered "resolved" if Δz is larger than the instrumental noise in the z direction. Defined in this manner, the resolution *d*, the minimum separation at which the spikes are resolved, is

$$d = 2\sqrt{2R\Delta z}$$

where one must enter a minimal detectable depression for the instrument (Δz) to determine the resolution. For a silicon tip with 5 nm radius and a minimum detectable Δz of 0.5 nm, the resolution is about 4.5 nm. However, the above model assumes the spikes are of equal height. Bustamante and Keller[34] went on to point out that if the height of the spikes is not equal, the resolution will be affected. Assuming a height difference of Δh, the resolution becomes:

$$d = \sqrt{2R}\left(\sqrt{\Delta z} + \sqrt{\Delta z + \Delta h}\right)$$

For a pair of spikes with 2 nm height difference, the resolution drops at 7.2 nm for a 5 nm tip and 0.5 nm minimum detectable Δz. While geometrical considerations are a good starting point for defining resolution, they ignore factors such as the possible compression and deformation of the tip and the sample, as well as the occurrence of contrast mechanisms that may improve the effective resolution.

2.3. IMAGING OPERATION MODES

Roughly speaking, several modes of operation have been introduced in force microscopy, with a variety of names describing their characteristic features (Fig. 11).

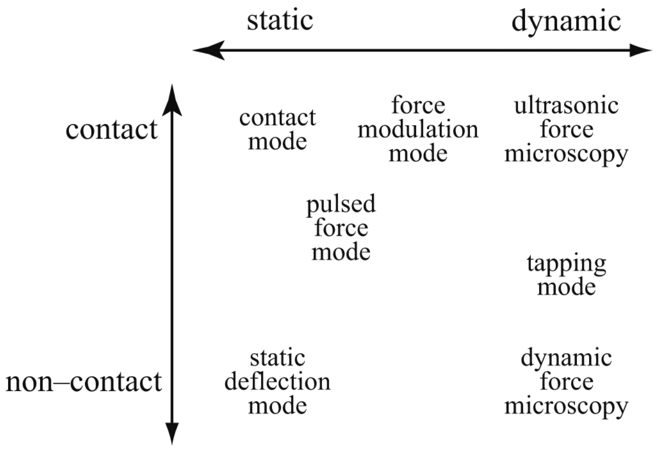

Fig. 11 – Different kinds of AFM operation modes.

In a first approximation the interaction between the tip apex of the probe and the surface can be described by a Lennard–Jones potential: this exponential function is described by the following equation:

$$U_{LJ}(r) = U_0 \left(-2\left(\frac{r_0}{r}\right)^6 + \left(\frac{r_0}{r}\right)^{12} \right)$$

where the first term of the sum describes the long–distance attraction caused mainly by dipole–dipole interaction of atoms. The second term takes into account the atom repulsion at small distances. The r_0 parameter is the equilibrium distance and U_0 the energy value in the minimum of potential as in Fig. 12.

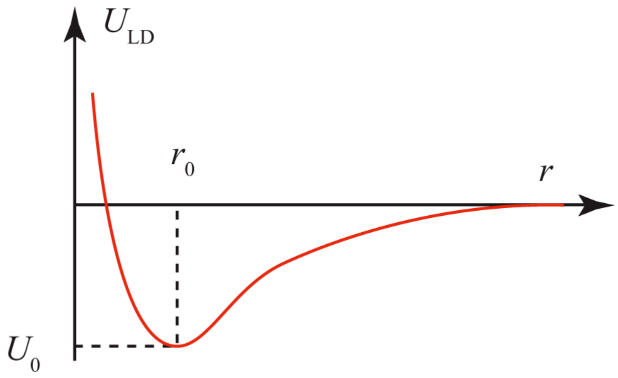

Fig. 12 – Qualitative shape of the Lennard–Jones potential.

The above–mentioned forces are due to the interaction among the electronic clouds of atoms belonging to atoms at the end of the tip and those of the surface in proximity of the tip. The common energy of the system can be derived by summing the elementary interactions for each atom of tip and sample (Fig. 13).

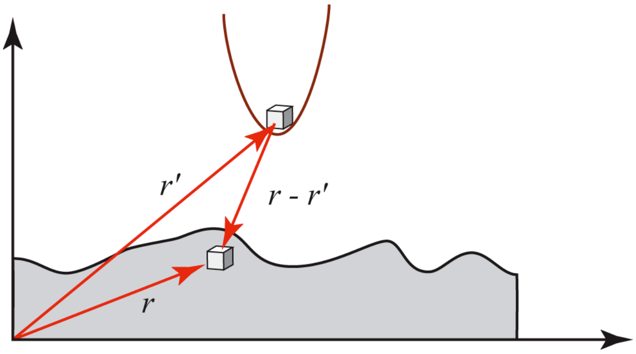

Fig. 13 – Representation of tip–sample interaction for energy calculation.

For the interaction energy we get:

$$W_{SP} = \int_{V_P}\int_{V_S} U_{LJ}(r - r')n_P(r')n_S(r)dVdV'$$

where $n_S(r)$ and $n_P(r')$ are the densities of atoms in the sample and the tip, respectively. Accordingly, the force affecting the tip due to surface can be calculated as follows:

$$\vec{F}_{PS} = -\nabla \cdot (W_{PS})$$

Generally, this force has both a normal to a surface component as well as a lateral one (laying in the plane of the sample surface). The actual interaction of the tip with the sample has a more complex character. However, the basic features of the given interaction are the same: the AFM tip experiences attraction from the sample at larger distances and repulsion at smaller ones.

2.3.1. Interaction forces

The forces relevant to AFM are ultimately of electromagnetic origin. However, different intermolecular, surface, and macroscopic effects give rise to interactions with distinctive distance dependence. In the absence of external fields, the dominant forces are van der Waals interactions, short–range repulsive interactions, adhesion and capillary forces.

Long–range van der Waals interactions stem from electromagnetic field fluctuations that could arise from thermal and/or zero–point quantum fluctuations. Field fluctuations are universal which makes van der Waals forces ever–present, independent of the chemical composition of the surface or the medium. van der Waals forces are amenable to several theoretical treatments of varying complexity. Here, only simple approximations for a geometry (sphere–flat) that resembles the tip–surface interface will be taken into account. By assuming additivity, the van der Waals force for a sphere–flat geometry is

$$F_{WdV} = -\frac{HR}{6d^2}$$

where H is the Hamaker constant, R is the tip radius, and d is the instantaneous tip–surface separation.

Repulsive forces among atoms or molecules arise from Pauli and ionic repulsion. However, if the contact area between two objects involves tens or hundreds of atoms, the description of the effective repulsive force can be obtained without considering Pauli and ionic repulsion. The surfaces of two bodies are deformed when they are brought into mechanical contact. The deformation depends on the applied load and the properties of the material. Continuum elasticity theories describe the contact and adhesion between finite bodies under an external load. Hertz provided the first model in 1881. It described the problem for elastic spheres without adhesion forces. Since then, a variety of approximations and models have been developed. Johnson–Kendall–Roberts (JKR)[35] and Derjaguin–Muller–Toporov (DMT)[36] models provide analytical relationships between deformation and applied force. They have become the standard models for contact AFM studies. Maugis[37] and Muller et al.[38] developed more sophisticated and self–consistent descriptions of the deformation, stress, and interaction between surfaces.

The forces listed above are due to an electrostatic interaction in vacuum among the end atoms of the tip and the surface, but the situation is quite different in the presence of other forces like magnetic, chemical, capillary, *etc.*

2.3.2. Repulsive contact mode

In the static contact mode under a repulsive regime, the tip at the end of the cantilever is brought very close to the surface and maintained over the sample that has to be analyzed. Prevailing forces whose effect is at the basis for the operation of the microscope in this mode are the core repulsive forces among nearest atoms of the tip–sample heterogeneous system, and the quantum repulsive forces due to Pauli exclusion principle. These forces have mean values equal to about 10^{-9} N.

In contact mode, the cantilever deflection is revealed and compared to a value preset by the operator. If the measured deflection differs from the deflection set point, the feedback provides a correction for the voltage applied to the piezo scanner in order to constraint the cantilever at the desired deflection, and correction are used to get topographical information.

The force on the tip due to its interaction with the sample is sensed by detecting the deflection of the compliant lever with a known spring constant. This cantilever deflection (displacement smaller than 0.1 nm) has been measured by detecting a tunnelling current similar to that used in the STM in the pioneering work of Binnig *et al.*,[31] by capacitance,[39] piezoresistive,[40] and piezoelectric detection and by optical techniques, namely by optical interferometry[41] with the use of optical fibres,[42] and by optical (laser) beam deflection[43] (Fig. 14); the latter is by far the most common method in commercial systems, and it is exploited also in the microscope used in this thesis work.

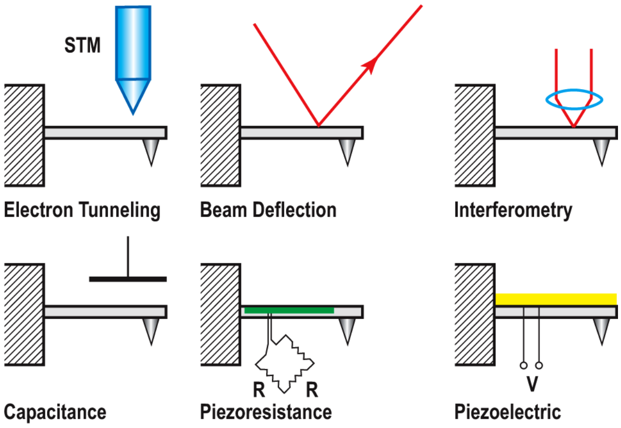

Fig. 14 – Schematics of common methods for the measurements of cantilever deflection.

2.3.3. Static non Contact Mode

This scanning mode opened the way for a new kind of AFM measurements. In this mode, the tip is kept at a distance of 50–150 Å from the surface thus avoiding damage of the surface; at this height the tip feels long–range attractive forces. Unfortunately, these forces are much weaker than the repulsive forces involved in contact mode operation, and can be easily masked by noise or unavoidable fluctuations. For this reason this method is not so useful and it is preferable to use the dynamic mode.

2.3.4. Dynamic Mode

In the last decade AFM experienced a significant evolution when a vibrating probe was used to explore the surface topography. Since then, dynamic AFM methods emerged as powerful and versatile techniques for atomic and nanoscale characterization and manipulation of a wide variety of surfaces. High–resolution images of DNA, proteins, and polymers have been obtained in air and liquids.[44] True atomic resolution images of several semiconductor and insulator surfaces have also been reported.[45] The interest and the sophistication of dynamic modes stem from different factors: the possibility of imaging soft samples while avoiding their damage; the existence of several parameters sensitive to the tip–sample interaction (amplitude, frequency, phase shift, and cantilever deflection); the potential to develop quantitative methods to characterize material properties at nanometre scale.

The amplitude, the resonant frequency, and the phase shift of the oscillation link vibrating tip dynamics to tip–sample interaction. Any of them could be used as a feedback parameter to track the topography of a surface and to unravel local variations in a variety of surface properties. Depending on the regime of forces involved in the interaction between the probe and the surface, dynamic modes can be divided in two major classes:

- Tapping mode
- Dynamic non contact mode

The first one consists in keeping the cantilever at large oscillation amplitude that can feels both attractive and repulsive forces. For instance, if the cantilever is kept oscillating according to an equation of the type $A = A_0 \cos \omega t$, the size of the oscillation amplitude is such that $A_0 \gg r_0$ (where r_0 is the distance at the minimum energy in the Lennard–Jones potential as reported in Fig. 12).

In dynamic non–contact mode, the condition to be satisfied is that $A_0 \ll r_0$. Accordingly, this small amplitude AFM is a dynamic technique in which the AFM cantilever is vibrated at very small amplitudes, typically less than 1 Å and the amplitude, phase and/or resonance frequency of the lever are measured. Small amplitudes serve to linearise measurements of tip–surface interactions. Consequently, experimental values can be directly related to interaction stiffness (negative if the force gradient is negative) and energy dissipation. Because of the small amplitudes, the measurement is local, and interactions can be mapped point–by–point. This eliminates ambiguities present in large amplitude techniques.

Martin *et al.*[46] pioneered the use of a force microscope operated in oscillating mode. They proposed an analytical model that allows for very small vibration amplitudes (say below 1 nm), to connect changes of the oscillation amplitude with variations of the derivative of the force along the normal to the surface. In H. K. Wickramasinghe and co–workers experiments,[47] the amplitude changes were dominated by long–range attractive forces of van der Waals type. They also suggested the use of the amplitude as feedback signal for imaging applications. A few years later Zhong *et al.*[48] reintroduced the use of the amplitude as the signal feedback. They proposed two modifications. Firstly, the cantilever was excited with large oscillation amplitudes up to 100 nm. Secondly, relatively stiff cantilevers with spring constants of about 40 $\mathrm{N\,m^{-1}}$ were used. They thought that those values were needed to avoid the trapping of the tip by surface forces. It was also believed that short–range repulsive forces (contact forces) were responsible for the amplitude reduction. Their method was named tapping–mode AFM (or intermittent contact AFM). Since then, both approaches have evolved separately.

2.3.4.1. Experimental methods to excite the cantilever

Acoustic and magnetic excitation modes have been developed to excite the microcantilever–tip ensemble. In the acoustic excitation mode, a piezoelectric actuator holding the cantilever–tip ensemble is attached below the substrate.[49] The application of an oscillating voltage to the actuator produces its vibration and this in turn gives rise to the oscillation of the microcantilever. This excitation mode is widely used in air and in liquids, although in liquids it also excites the fluid. Other researchers[50] have directly excited the tip by applying an oscillating magnetic field to a magnetised cantilever.

A thorough understanding of dynamic AFM operation requires solving the equation of motion of the cantilever–tip ensemble under the influence of tip–surface forces. A complete rigorous approach is a formidable task that involves the solution of the equation of motion of a three–dimensional object, a vibrating cantilever. Symmetry considerations allow for approximating the microcantilever beam by a one–dimensional object, then:

$$EI\frac{\partial^4 w(x,t)}{\partial x^4}+\mu\frac{\partial^2 w}{\partial t^2}=F(x,t)$$

Here $w(x, t)$ is the transverse displacement of the cantilever beam; E, I, and μ are the Young's modulus, the moment of inertia, and the mass per length unit of the cantilever, respectively; $F(x, t)$ is a term that contains all of the forces per length unit acting on the tip. The above equation implicitly assumes that the tip is a massless object. The difficulty in tackling the above equation can be grasped by following the works of Butt and Jaschke,[51] Sader,[52] and Stark and Heckl.[53]

To gain some insight into the tip motion, several authors have considered the cantilever–tip ensemble as a point–mass spring; then the tip motion could be approximately described by a non–linear, second–order differential equation:

$$m\frac{\partial^2 z}{\partial t^2}+kz+\frac{m\omega_0}{Q}\frac{\partial z}{\partial t}=F_{ts}+F_0\cos(\omega t) \qquad \text{Eq. 1}$$

where F_0 and ω are the amplitude and the angular frequency of the driving force respectively, Q, ω_0, and k are the quality factor, angular resonance frequency and elastic constant of the free cantilever, respectively. F_{ts} contains the tip–surface interaction forces.

In the absence of tip–surface forces, Eq. 1 describes the motion of a forced harmonic oscillator with damping.

2.3.4.2. Dynamics of a vibrating tip in the proximity of a surface

The aim of this section is to provide fundamental concepts and theories required for the understanding of the oscillating tip in dynamic mode AFM. The description takes into account the tip–surface interactions including interaction potential with long range Van der Waals forces and contact repulsive forces. Even with simplified assumptions, those forces have power law dependencies on the tip–surface separation. The non–linearity of interactions has deep implications in the resulting tip motion. It also makes difficult to find analytical solutions. The harmonic approximations are discussed in the following.

In the absence of tip–surface forces ($F_{ts} = 0$), Eq. 1 is the equation of a forced harmonic oscillator with damping. The study of the motion of a harmonic oscillator can be considered as a prerequisite for understanding the complex tip motion in dynamic mode AFM.

Let us start with some qualitative considerations about the asymptotic limits of the oscillation amplitude as a function of the excitation frequency. At low driving frequencies with respect to the free resonant frequency, the response is controlled by the stiffness of the spring. The oscillator moves along with the driving force at an amplitude close to F_0/k. At frequencies very large compared to the free resonant frequency, the term kz is small compared to d^2z/dr^2; hence, the response is controlled by inertia. Then relatively small oscillation amplitude should be expected with a phase shift of 180°. The acceleration of the harmonic oscillator is 180° out of phase with the displacement.

The solution of a harmonic oscillator with damping can be found as:

$$z = Be^{-\alpha t}\cos\left(\omega_r t + \beta\right) + A\cos\left(\omega t - \phi\right)$$

where α is the damping coefficient. The solution has a transient term and a steady component. The steady term is a sinusoidal function (harmonic) with a phase lag with respect to the excitation force. The dependence of the amplitude with the excitation frequency can be calculated by the Lorentzian expression:

$$A(\omega) = \frac{F_0/m}{\left[\left(\omega_0^2 - \omega^2\right)^2 + \left(\omega\omega_0/Q\right)^2\right]^{1/2}} \qquad \text{Eq. 2}$$

and the phase shift is:

$$\tan\phi = \frac{\omega\omega_0/Q}{\omega_0^2 - \omega^2}$$

where ϕ is the angle by which the driving force leads the displacement. The above expression are simplified by exciting the oscillator at its resonance frequency in the absence of damping ($\omega = \omega_0$):

$$A_0 = \frac{QF_0}{k}$$

Moreover, the damping modifies the resonance frequency of the cantilever. Resonance and natural (free resonance) frequencies are related by:

$$\omega_r = \omega_0 \left(1 - \frac{1}{2Q^2}\right)^{1/2}$$

Eq. 2 shows that the oscillation amplitude depends on the driving force F_0, the hydrodynamic damping, and the position of the excitation frequency with respect to the free natural frequency. If we assume that the tip (the harmonic oscillator) is under the influence of a parabolic tip surface interaction potential, then the total force acting on the tip F includes the elastic response kz and the interaction force F_{ts}. For small displacements with respect to the equilibrium position, the total force can be expressed by

$$F = F_0 + \left(\frac{dF}{dz}\right)_{z_0} (z - z_0) \qquad \text{Eq. 3}$$

with

$$k_e = -\frac{dF}{dz} = \left(k - \frac{dF_{ts}}{dz}\right)_{z_0} \qquad \text{Eq. 4}$$

Eq. 3 describes the motion of a harmonic oscillator with an effective spring constant given by Eq. 4, then the new effective resonance frequency is calculated by

$$\omega_e = \left(\frac{k - (dF_{ts}/dz)}{m}\right)^{1/2} \qquad \text{Eq. 5}$$

Eq. 5 shows that the resonant frequency of a weakly perturbed harmonic oscillator depends on the (vertical) gradient of the interaction force. A change in the effective resonance frequency implies a whole shift of the resonant curve according to Eq. 2, where ω_0 is replaced by ω_e. The dependence of the amplitude on the excitation and the effective resonance frequencies introduces a possible mechanism to explain the dependence of the oscillation amplitude on the strength of the interaction force, or in other words, on the tip–surface separation.

If the tip is excited at the natural frequency, the approach of the tip towards the surface will modify the resonance frequency thus giving rise to a change of the oscillation amplitude. The actual oscillation amplitude will be given by the value of the new resonant curve at the excitation frequency of the oscillator. As a consequence, the new oscillation amplitude will be smaller than the free amplitude. However, if the excitation frequency is just off resonance to the left, the oscillation amplitude can decrease or increase depending on the position of the new resonant frequency with respect to the natural frequency.

2.3.5. Common operating modes

Even if a large variety of imaging modes are available, the most common operating modes used in a large variety of experiments are essentially *contact mode* and *tapping mode*. The first method allows for rapid scans and better resolution but can give also some problems, such as sample damage (Fig. 15) or displacement of specimens if not firmly fixed to the surface.[54]

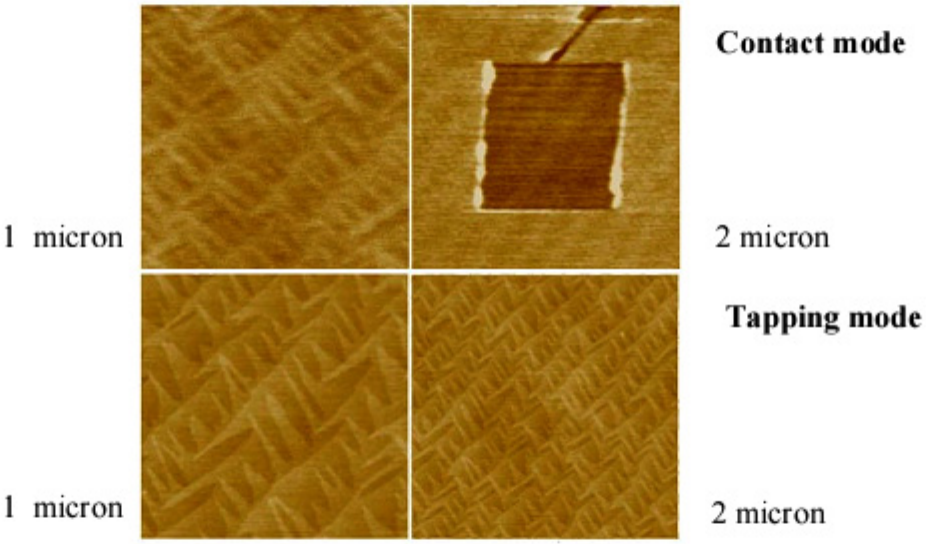

Fig. 15 – Contact and tapping mode images of the same Si (100) epitaxial wafer. The left images were taken first, then the scan size was doubled and the sample was immediately re–scanned to include the area imaged in the first scan. Tapping mode images show no surface alteration and better resolution.

On the other hand, contact mode offers the possibility to monitor both the topography and the friction (the lateral force) while scanning, thus giving more detailed information regarding the wear friction. In this mode the lateral deflection of the cantilever is measured as the tip is scanned across the sample. Changes in lateral deflection represent relative frictional forces between the probe tip and the sample surface. This type of measurement allowed for monitoring the formation of an alkylthiol monolayer over gold (Fig. 16).

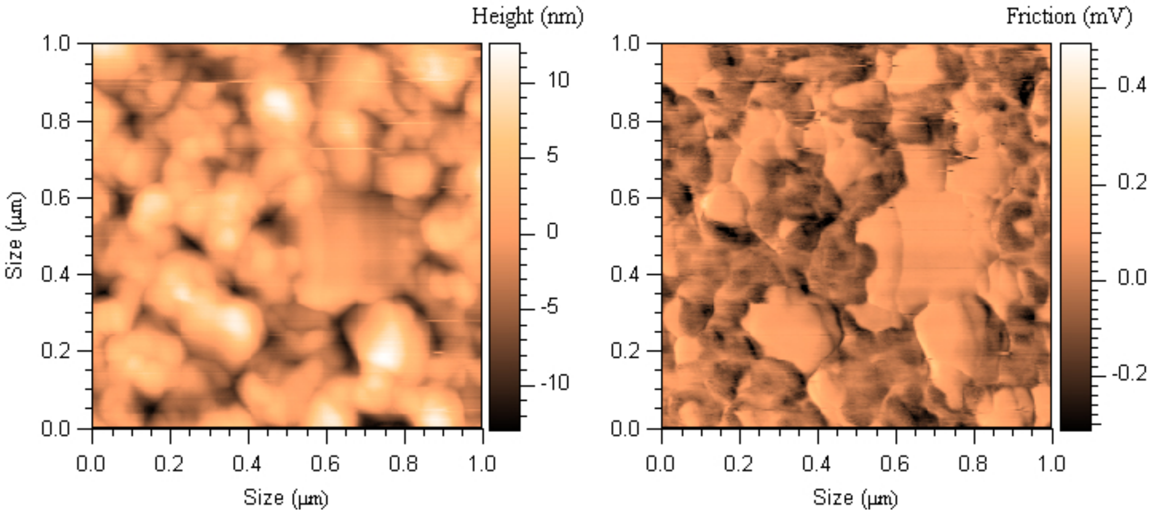

Fig. 16 – Topography (left) and friction (right) maps of an alkylthiol molecular layer on gold surface. Darker areas in the right image correspond to alkylthiol monolayer.

2.4. FORMATION AND PROCESSING OF AFM IMAGES

The scanning of a surface in a scanning probe microscope is similar to the movement of an electronic beam across the screen of TV electron ray tube. The tip goes along the line (row) first in forward (Fig. 17), and then in the reverse direction (horizontal scanning), then passes to the next line (frame scanning). Tip movement is done by a saw tooth voltage formed by digital–to–analog converters; this voltage is used to feed the scanner. As a rule, registration of the information on the surface topography is made in the forward pass.

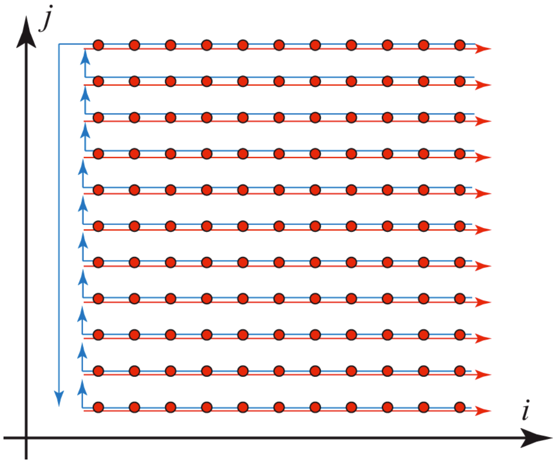

Fig. 17 – Schematic representation of the scanning process. Red arrows indicate the scanner forward motion direction, whereas blue arrows show the scanner reverse motion. Registration of the information is composed by points recorded during the scan.

The information gained with the aid of a scanning probe microscope is stored as a bidimensional frame composed by a_{ij} values. The physical meaning of these values is determined by what was digitized during the scan. To each value of an *ij* couple corresponds a point of the surface within the scanning area borders. The real coordinates of a surface points are calculated with the help of a single multiplication between the index and the distance between points:

$$x_i = x_0 \cdot i, \quad y_i = y_0 \cdot j$$

Here x_0 and y_0 are the distances between successive points along x and y axes, where the information was recorded. As a rule, AFM images are 2^n square matrixes (e.g. 256x256 or 512x512 elements). Visualization of AFM maps is done by computer graphics, basically as three–dimensional (3D) and bi–dimensional (2D) images. In 3D visualization, the topography (or whatever the acquired signal) of the surface is reproduced by plotting

$z = f(x, y)$ in axonometric prospective. In 2D visualization, the surface is reconstructed as a bi–dimensional brightness image: a given colour corresponds to $z = f(x, y)$ for each surface point. Gradient palettes, where colouring of images is made by the tone of a selected colour according to the height of surface points, are most widely used.

AFM images, alongside with the helpful main information, contain also a lot of secondary effects deforming the data on the morphology and surface properties. Possible imperfection of the equipment and external parasitic influences that can cause distortions in SPM surface images are schematically presented on the following list:

- Hardware noises
- Constant inclination
- Scanner imperfection
- Instability of tip–sample contact
- Noise due to external vibrations.

2.4.1. Subtraction of a constant component and of a plane

As a rule, AFM images contain a constant component, which does not bear useful information about the surface topography, but reflects the accuracy of sample approach to the centre of the dynamic range of scanner movement along the z axis. The constant component is removed from the SPM frame by using software tools so the new values of the topography heights in the frame are equal to

$$z'_{ij} = z_{ij} - \bar{z} \text{ where } \bar{z} = \frac{1}{N^2}\sum_{ij} z_{ij}$$

2.4.1.1. Subtraction of a constant inclination

Generally, surface images acquired by using probe microscopes have common inclination. It can be caused by several reasons. The inclination may appear as a result of incorrect installation of the sample on the tip or non–flatness of the sample. The inclination might be connected with a temperature drift, which results in tip shifting with respect to the sample. It might be due to a non–linearity of the piezo–scanner movement. Inclination imaging takes a large volume of useful space in the SPM frame, so that the small image details become not visible. To eliminate this imperfection, subtraction of the constant inclination is performed in data post–processing. For this purpose, the least squares method is used at first to find an approximating plane $P^{(1)}(x, y)$, which has minimal deviations from the topography of the surface $z = f(x, y)$. Then the given plane is subtracted from the AFM image, as schematically depicted in Fig. 18. If the inclination in the AFM image is caused by an inclination of the sample relatively to the tip axis, it is expedient to turn the plane on an angle corresponding to the angle between the $\vec{n}$ normal to the plane and the z axis; thus the coordinates of a surface $z = f(x, y)$ are reconstructed according to transformations of a spatial turn. The procedure of inclination subtraction implies the subtraction of the fitted plane coordinates from the coordinates of the original AFM image as stated below:

$$z'_{ij} = z_{ij} - P^{(1)}_{ij}$$

This allows for keeping correct geometrical relations in the x, y plane among the objects in the AFM image (Fig. 18).

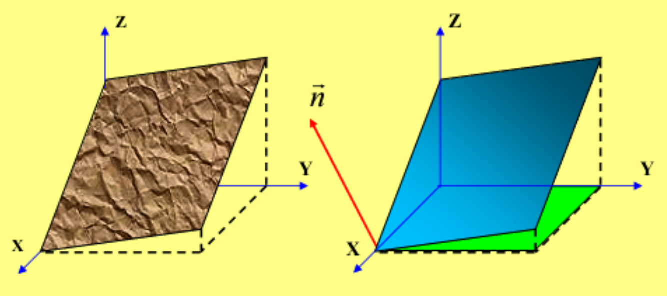

Fig. 18 – Subtraction of a constant inclination from SPM images of a surface: original image (left) and plane P_{ij} (in cyan, right).

Thus, a new array with smaller range of values is obtained, and more contrasted fine details of the image are displayed (Fig. 19).

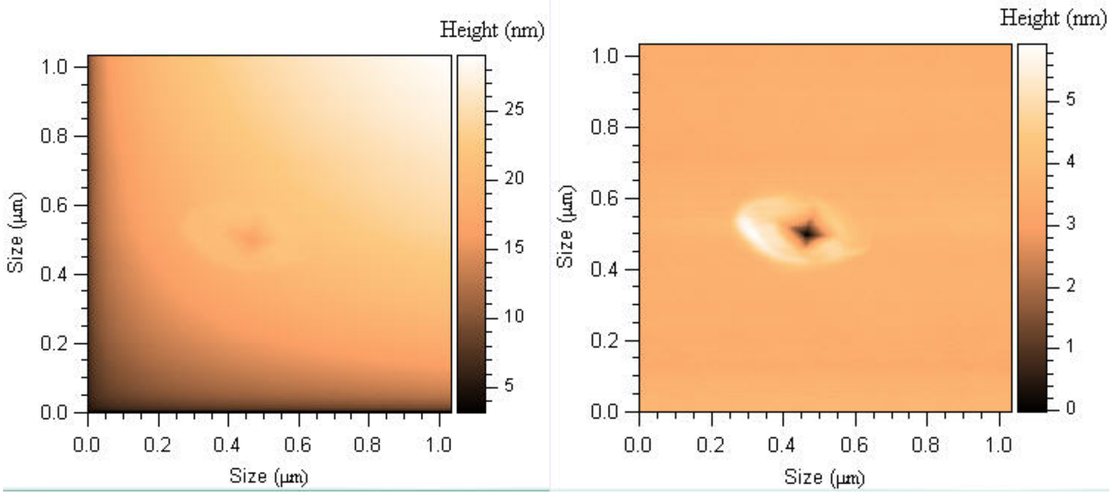

Fig. 19 – An approximating plane P(x, y) was found by least square method and removed from the original image (left) in order to obtain an image with previously "hidden" detailed features (right).

2.4.2. Removal of distortions due to scanner imperfections

Imperfection of the piezo–scanner leads to a number of specific artefacts in SPM images. Scanner imperfections, such as inequity of scanner direct and reverse motions (hysteresis), creep, and nonlinearity of piezoceramics are partially compensated by the hardware and by the selection of the most favourable scanning modes. However, despite of it, the AFM images contain distortions, which are difficult to remove at the hardware level. In particular, since the scanner movement in the plane of the sample affects the tip location over the surface (along the z–axis), AFM images represent a superposition of the actual topography plus some surface of the second (and sometimes of higher) order. An approximation plane of the second order $P^{(2)}(x, y)$ is found by using the least–squares method to eliminate such sort of artefacts. This surface has minimal deviations from initial function $z = f(x, y)$; it is subtracted from the initial AFM image:

$$z'_{ij} = z_{ij} - P^{(2)}_{ij}$$

Another type of distortions is connected to nonlinearity and non–orthogonality of movements of the scanner in x, y planes. These effects result in distortion of geometrical proportions in various parts of the surface SPM image Fig. 20.

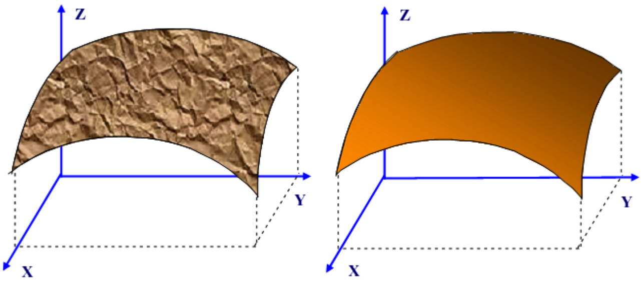

Fig. 20 – Subtraction of a second order surface from the SPM image of a surface.

Procedure of correction of the SPM images with the help of a file of correction coefficients, which is created during the scanning of test structures with a well–known topography by a specific scanner, is used to eliminate such distortions.

2.4.3. Filtering AFM images

Hardware noise, instabilities of the tip–sample contact during scanning, external acoustic clatter and vibrations lead to the situation when AFM images contain both useful information and noise components. The noise can be partially removed from AFM images by using software tools, in particular filters of different types.

2.4.3.1. Median filtering

Median filtering provides good results in the removal of high–frequency random noise from AFM images. This is a nonlinear method of image processing that basically can be explained as follows. First the working window (consisting of n × n points) of the filter is selected (Fig. 21). During filtering this window moves across the frame from point to point, and the following procedure is performed.

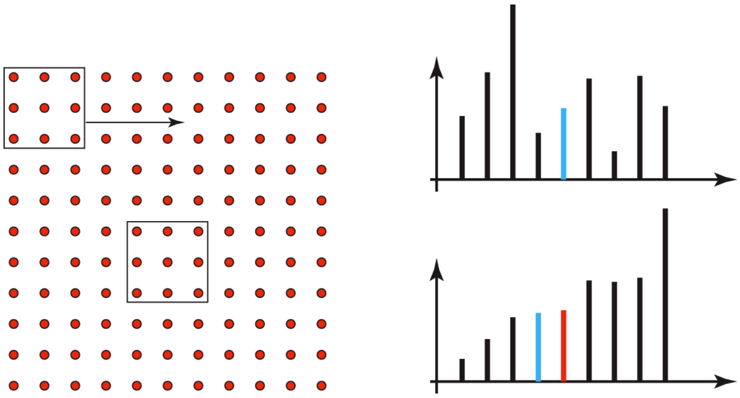

Fig. 21 – On the left is showed the path of the window filter over the image. On the right are reported on top the elements in an unsorted array (centre element) and below the data in the sorted array (new centre element).

Values of the SPM image amplitude in points of this window are lined up in ascending order, and the value in the centre of the sorted line is moved to the central point of a window. Then the window is shifted to the next point, and the procedure is repeated. Thus, major random emissions and dips are shifted at the ends of a sorted file and do not enter the final (filtered) image. It is worth noting that during the filtering process, at the edges of the frame there are unfiltered areas, which are discarded, in the final image.

2.4.3.2. Averaging over lines

The process of scanning a surface in a scanning tip microscope occurs in such a way that the frequency of registration of the information within a line strongly differs (at least, hundred times) from the frequency of registration of lines. It turns out that high–frequency noise is contained basically in lines of the SPM image, and low–frequency noises change the average level of line scans. Moreover, the tip–sample distance changes frequently during scanning due to micro movements of the constitutive elements of the microscope measuring head or because of a change of condition in a tip working part, for instance, capture by the apex of the tip of a micro particle from a surface, *etc*. This leads to the appearance of steps parallel to the direction of fast scanning in the SPM image. These steps are caused by the bias of one part of the SPM frame relative to another. It is possible to get rid of such defects in SPM images by using the alignment procedure of the frame over the lines. The average topography value is determined in every scanning line:

$$\bar{z}_j = \frac{1}{N}\sum_i z_{ij}$$

then the corresponding average values are subtracted from the recorded values in every line of the frame:

$$z'_{ij} = z_{ij} - \bar{z}_j$$

so that in the new frame the average value in every line is equal to zero. This leads to the removal from the frame of the steps connected to sharp changes of average values in lines.

2.4.3.3. Fourier filtration of the AFM images

The spectral filtration based on Fourier transformations is one of the most powerful methods of SPM image correction. It is well known that any function can be presented as a Fourier series. In case of the SPM frame, the Fourier transformation is made with discrete values. Fourier image of the surface can be found using the following formula:

$$F_{\alpha\beta} = \frac{1}{N^2}\sum_{ij} z_{ij} \exp\left[2\pi\Im\left(\frac{\alpha \cdot i}{N} + \frac{\beta \cdot j}{N}\right)\right]$$

where the imaginary unit is designated as $\sqrt{-1} = \Im$, α and β are the values of the square matrix respectively in *i* and *j* positions, and *N* represents the number of points in each line and row of the matrix. The reverse Fourier transformation is defined as:

$$z_{ij} = \sum_{\alpha\beta} F_{i\alpha\beta} \exp\left[-2\pi\Im\left(\frac{\alpha \cdot i}{N} + \frac{\beta \cdot j}{N}\right)\right]$$

During the Fourier–filtration the transformations are made with a spatial spectrum of the surface. The Fourier–transformed image of the surface can be written as:

$$F'_{\alpha\beta} = F_{\alpha\beta} \cdot H_{\alpha\beta}$$

where $H_{\alpha\beta}$ represents the spectral function of the applied filter. Then the filtered image is obtained by reverse Fourier transformation of the processed spectrum of the surface:

$$z'_{ij} = \sum_{\alpha\beta} F_{\alpha\beta} \cdot H_{\alpha\beta} \exp\left[-2\pi\Im\left(\frac{\alpha \cdot i}{N} + \frac{\beta \cdot j}{N}\right)\right]$$

The filters of low and high frequencies with circular and square windows are most widespread. For low frequency filters, the spectral filter functions are defined as:

$$H_{\alpha\beta}^{cir} = \begin{cases} 1 & for \quad \sqrt{\alpha^2 + \beta^2} \le R \\ 0 & for \quad \sqrt{\alpha^2 + \beta^2} > R \end{cases} \qquad H_{\alpha\beta}^{sqr} = \begin{cases} 1 & for \quad |\alpha| \le A; |\beta| \le A \\ 0 & for \quad |\alpha| > A; |\beta| > A \end{cases}$$

where *R* and *A* represent the radius of a circular window and the size of a square window of the filter function, respectively. By analogy, the corresponding high frequency filters are:

$$H_{\alpha\beta}^{cir} = \begin{cases} 0 & for \quad \sqrt{\alpha^2 + \beta^2} \le R \\ 1 & for \quad \sqrt{\alpha^2 + \beta^2} > R \end{cases} \qquad H_{\alpha\beta}^{sqr} = \begin{cases} 0 & for \quad |\alpha| \le A; |\beta| \le A \\ 1 & for \quad |\alpha| > A; |\beta| > A \end{cases}$$

Bidimensional Fourier analysis is useful also for highlighting the presence of periodic structures in a surface, i.e. crystal planes or other regular structures are well detected by such analysis.

2.5. PHASE IMAGING

Phase imaging is a powerful extension of atomic force microscopy: it is a special technique capable of revealing particular structures often not revealed by topographic images. This method of analysis can be used only in dynamic mode. By mapping the phase of the cantilever oscillation (with respect to the driving oscillation) during tapping mode scans, phase imaging permits to overcome simple morphological mapping and hence detect variations in composition, adhesion, viscoelasticity, and several other properties. Applications include identification of contaminants, mapping of different components in composite materials, and differentiating regions of high and low surface adhesion or hardness.

Phase imaging is a relatively new technique; it has the advantage of being performed at the same time of topographic imaging in tapping mode, i.e. both topographic and phase images can be obtained in a single scan. By taking into account that the interactions between the tip and the surface depend not only on the sample topography but also on other surface properties, also the response of the tip–cantilever system to the oscillating driving force depends on these properties.

In phase imaging, the phase of the sinusoidal oscillation of the cantilever is measured relative to the driving signal applied to the cantilever (Fig. 22).

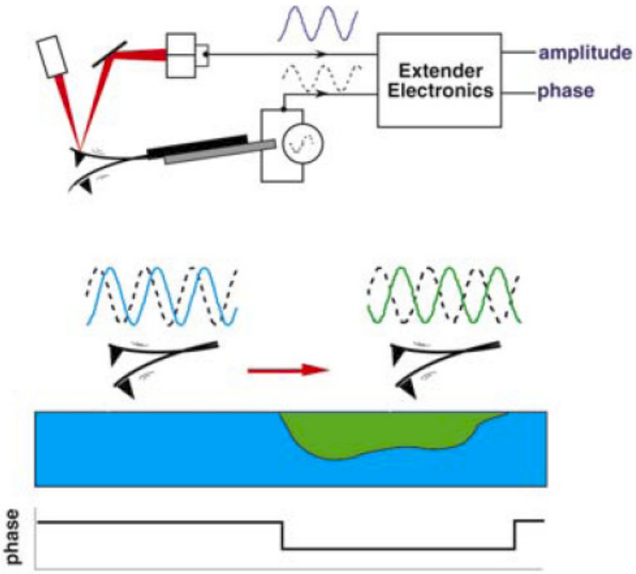

Fig. 22 – Schematic representation of phase imaging operation mode: the extender electronics measure the phase lag between the cantilever oscillation (solid line) and the driver piezo (dashed line).

Recording this phase shift during tapping mode scans produces phase images. Phase imaging can detect, for instance, different polymer components related to their stiffness or areas of different hydrophobicity/hydrophilicity in solid solutions.

Before the invention of tapping mode AFM, high resolution imaging of polymers by scanning probe microscopy was restricted to a few polymer surfaces. In fact, normal and lateral tip–surface forces often produced dramatic modifications of the polymer surfaces. Most of those modifications came to an end when the polymers were imaged by dynamic modes. Since then, the dynamic mode did not just open the potential of scanning probe methods to investigate the nanostructure morphology of polymers, it also provided the *phase imaging mode*, especially suited to study polymer surfaces.

For instance, this method of investigation can be used to collect information on the separation of the components constituting the surface of block copolymers (Fig. 23).

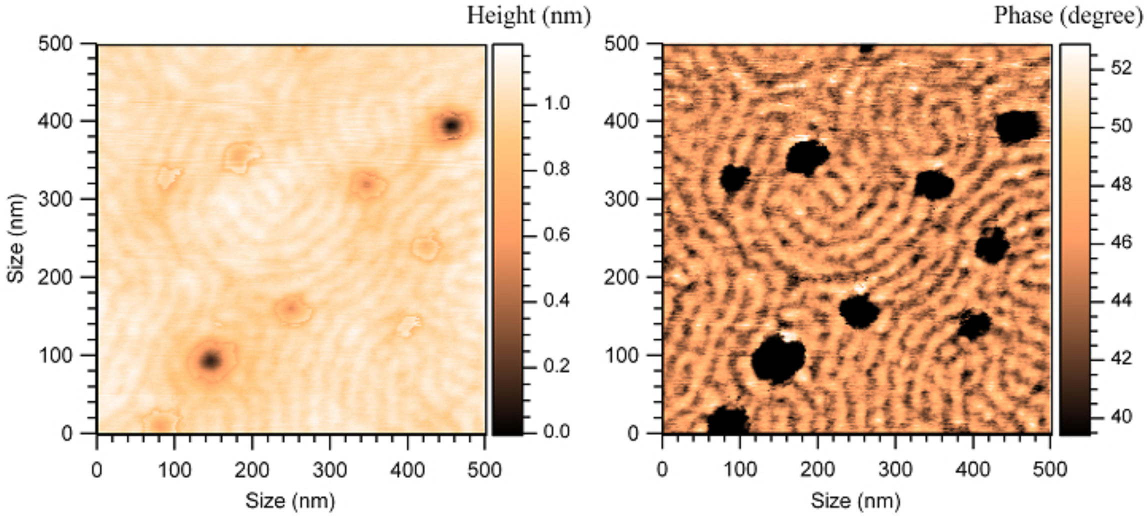

Fig. 23 – Topography (left) and phase (right) images of a block copolymer. Phase separation is especially clear in the phase map: brighter and darker areas represent stiffer and softer copolymer phases, respectively.

Indeed, the topography image in the left panel provides very little indication of the heterogeneous nature of the sample, whereas the right image clearly maps the two phases of the material (lamellae), resolving features as small as 20 nm. The polymer structure is reported in Fig. 24.

The image was obtained in the so called hard tapping mode: the amplitude of the cantilever A_0 used to "excite " viscous–elastic response of the material was very high compared to equilibrium distance R_0 in the Lennard–Jones potential (Fig. 12). On the other hand, analysis of other kinds of materials, such as fragile oligopeptides required only small amplitude in order to avoid damaging the sample and to get enough resolution to image small features.

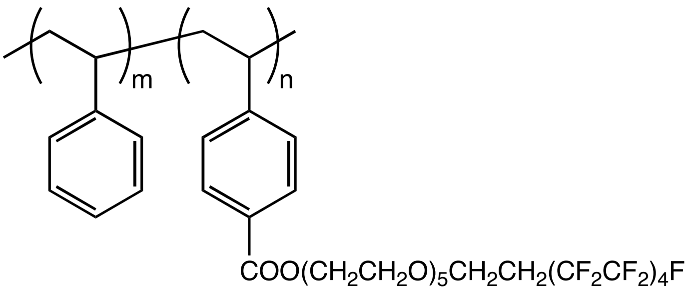

Fig. 24 – Schematic structure of the two block copolymer analysed by phase imaging. The fluorurated block is the soft fraction whereas the styrene block represents the stiff part.

In biology, the distinct advantage of this scanning probe microscope over the scanning electron microscope (SEM) is its ability to directly monitor changes in the conformation or aggregation state of macromolecules, and to study dynamic aspects of molecular interactions in their physiological environment.[55] For example, AFM has been used to image and study protein conformational changes, the unfolding of individual protein molecules, the interaction between single proteins, and the activity of individual enzymes. AFM has further been used to watch changes in the surface morphology of individual protein crystals as they were growing, and to determine their growth kinetics. Analogously, the formation of salt crystals can be monitored during PBS buffer evaporation. Changes in the morphology of the samples can be seen in Fig. 25, which shows the growth of the buffer salt crystals from "holes" in the surface that behaves as a nucleation centre.

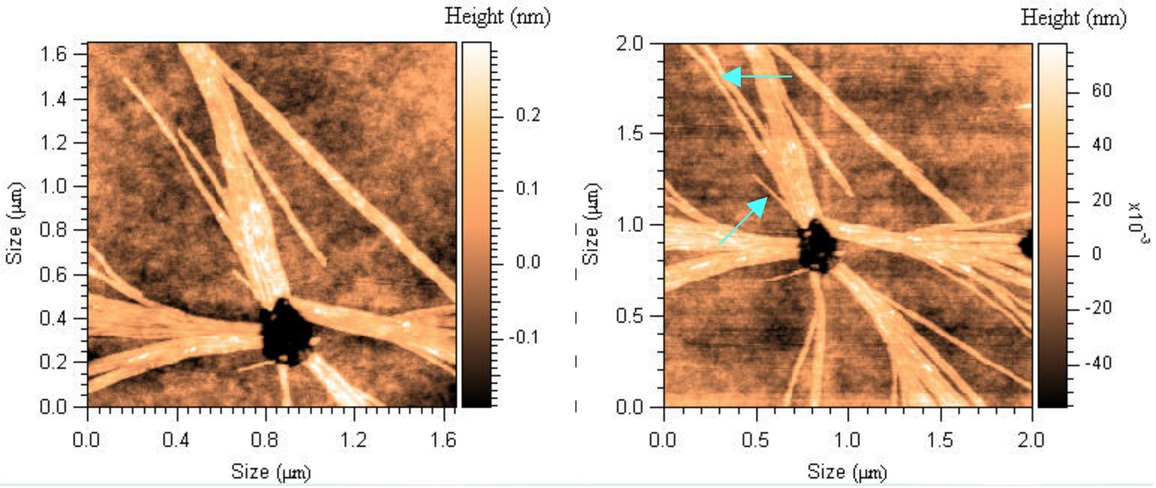

Fig. 25 – Crystal growth during the evaporation of a buffer solution. The two images were taken at 5 minutes interval. Arrows highlight the presence of newer crystals.

It is clear that a wealth of information can be gathered from such a kind of experiments: dynamics and molecular diffusion or rearrangements of samples can be studied with unprecedented details also in "living" environments. Moreover, temperature studies can also be performed by simply implementing a temperature controlled sample stage to investigate how dynamics is affected.

2.6. FORCE–DISTANCE CURVES

Force–distance curves have become a new fundamental tool in several research fields, such as surface science, materials engineering, biochemistry, and biology. Furthermore, they have a great importance for the study of surface interactions from a theoretical point of view. Force–distance curves have been employed for the study of many material properties and for the characterization of almost all known kinds of surface forces. Since 1989, several techniques of acquisition and data analysis have been developed and an increasing number of systems, presenting distinctive features have been analyzed. A great deal of work has been performed on both the theoretical and experimental aspects. Indeed, AFM is able to acquire force–distance curves on every kind of surface and in every kind of environment, with high lateral (25 nm), vertical (0.1 Å), and force (1 pN) resolution. The entire force–distance curve can be collected.

When acquiring force–distance curves, the piezo must be ramped along the z axis, i.e., the axis perpendicular to the surface. There are two principal modes of acquisition of force–distance curves. In the first mode, called static mode, the sample is displaced along the z axis in discrete steps and the variations in cantilever deflection are collected (§ 2.3.2). In the second mode, called non–contact mode, the cantilever is vibrated by an extra piezoelectric transducer while the sample is approached and withdrawn. The amplitude or the resonance frequency of the cantilever oscillations is collected as a function of tip–sample distance (§ 2.3.3).

The first study on force–distance curves acquired with an AFM, concerning the characterization of surface forces on LiF and graphite, dates back to 1988.[56] The first works trying to interpret force–distance curves and related information appeared in 1989–1990.[57] Since the first experiments, it has become clear that, when force–distance curves are acquired in air, meniscus forces exerted by thin layers of water vapour dominate any other interactions. Working in a controlled atmosphere or in a liquid environment can eliminate such forces.

In 1991 several studies of force–distance curves in liquids were performed, both theoretically and experimentally. Moreover, Mizes *et al.*[58] performed the first direct measurement of the spatial variation of adhesion. Since then, two different research lines have characterized the research on force–distance curves: on one hand, the study of different interactions in several environments, on the other hand, the "mapping" of such interactions, drawn from force–distance curves, in order to distinguish materials with different physical–chemical properties (a kind of "surface spectroscopy"). In 1994, a further technique was introduced.[59] This technique employs functionalized tips, i.e., tips covered with particular molecules that selectively adhere to other, in order to study specific forces by means of force–distance curves.

2.6.1. Relationship between AFM force–distance curves and tip–sample interaction forces

Force–distance curves are plots of cantilever deflection versus piezoelectric displacement. In order to obtain such a plot, the sample (or the tip) is ramped along the vertical axis (z axis) and the cantilever deflection δ_C is acquired. The tip–sample force is given by Hooke's law:

$$F = -k_C \delta_C$$

The distance controlled during the measurement is not the actual tip–sample distance D but the distance z between sample surface and the rest position of the cantilever. These two distances differ because of cantilever deflection δ_C and because of the sample deformation δ_S. These four quantities are related as follows:

$$D = z - (\delta_C + \delta_S)$$

Since one does not know in advance the cantilever deflection and the sample deformations, the only distance that one can control is the z distance, i.e. the displacement of the piezo. Therefore, the raw curve obtained by AFM should be called "force–displacement curve" rather than "force–distance curve". The latter term should be employed only for curves in which the force is plotted versus the true tip–sample distance that has been previously calculated from raw data. An AFM force–displacement curve does not reproduce tip–sample interactions, but is the result of two contributions: the tip–sample interaction *F(D)* and the elastic force of the cantilever. Such result can be intuitively understood by means of the graphical construction shown in Fig. 26.

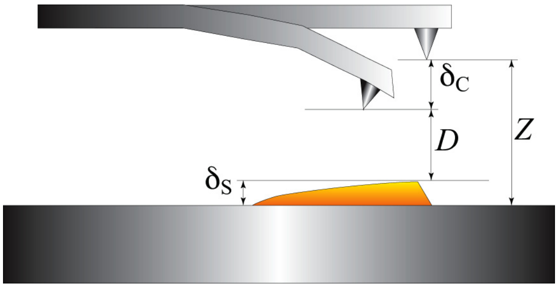

Fig. 26 – Representation of the tip–sample system: D is the actual tip–sample distance, whereas z is the distance between the sample and the rest position of the cantilever. These values differ because of the cantilever deflection δ_C and the sample deformation δ_S.

The total contributions of the force–distance curves are due essentially to the Lennard–Jones potential and the elastic potential of the cantilever.

The black curve in Fig. 27 represents the tip–sample interaction force. Since no surface force has been introduced yet, for the sake of simplicity the black plot was chosen to be the interatomic Lennard–Jones force. By expressing tip–sample forces through a potential of this type, only a simple qualitative description of the mechanisms involved in force–displacement curves can be provided. In particular, the attractive force between surfaces actually follows a force law D^{-6} and the repulsive part of the force is much more complex than the one modelled by the Lennard–Jones potential. The red line represents the elastic force of the cantilever and the resulting deflection (represented by some crosses) versus distance curve is shown in the second panel on the right. At each distance the cantilever deflects until the elastic force of the cantilever equals the tip–sample interaction force, so that the entire system is in equilibrium. Going from right to left, for instance approaching the sample, the deflection curve of loading is obtained. As soon as the tip is getting close to the surface, instability occurs and the tip suddenly jumps into contact. A similar phenomenon is also observed in tip withdrawal.

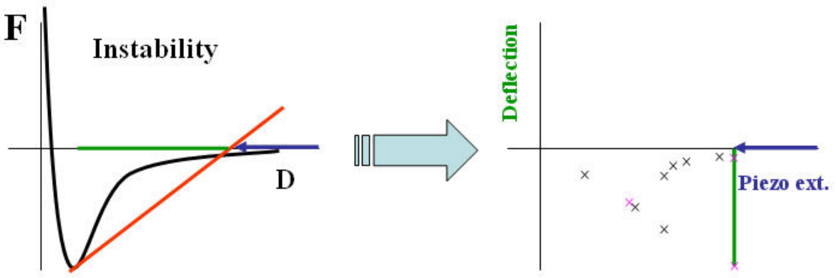

Fig. 27 – Derivation of force–distance curves.

An analytical expression for the force–displacement curves can be given following the derivation of Hao.[60] The cantilever–sample system can be described by means of a potential U_{tot} that is the sum of three potentials: $U_{CS}(D)$, $U_C(\delta_C)$, and $U_S(\delta_S)$. $U_{CS}(D)$ is the interaction potential between the tip and the sample and in our description we used the Lennard–Jones potential. $U_C(\delta_C)$ is Hooke's elastic potential of the cantilever and $U_{CS}(D)$ is the potential that describes the sample deformation. Sample deformations will be treated in detail in the section regarding the mechanical properties of the materials. For the present derivation, the Hooke's law describes the sample deformation:

$$U_C(\delta_C)=\frac{1}{2}k_C(\delta_C)^2 \quad U_S(\delta_S)=\frac{1}{2}k_S(\delta_S)^2$$

in which k_C and k_S are the cantilever and sample elastic constants.

Usually the interaction force can be written as:

$$F = -\frac{\partial U_{CS}}{\partial D} = -\frac{C}{D^n}$$

in which C and n depend on the type of forces acting between the tip and sample. The force expressed in the previous equation takes into account only the attractive part of the interaction, i.e. only the interaction prior to contact. The relation between z and δ_C can be obtained by forcing the system to be stationary:

$$\frac{\partial U_{tot}}{\partial(\delta_S)} = \frac{\partial U_{tot}}{\partial(\delta_C)} = 0$$

Since $\partial U_{CS} / \partial(\delta_S) = -\partial U_{CS} / \partial(D)$, we obtain

$$\delta_S = \frac{k_C}{k_S}\delta_C ,$$

$$k_C\delta_C = \frac{C}{(z - \delta_C - \delta_S)^n}$$

Hence:

$$k_C\delta_C = \frac{C}{(z - \beta\delta_C)^n}$$

in which $\beta = (1 + k_C / k_S)$.

In Fig. 28 the feature of the force–distance curve can be noted: the discontinuity pointed out by the green line. This feature is present also in the withdrawal curve and is called the “jump off contact”. Nevertheless, the two jumps are not equals: the difference in the path between approaching and retracting is usually called “force displacement curve hysteresis”.

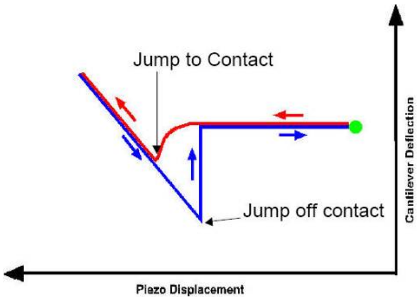

Fig. 28 – Typical shape of force–distance curves.

If we return to the previous equation that represent the condition for $U_{tot} = 0$, we can assess that the system must satisfy $\partial U_{tot} / \partial(\delta_C)^2 > 0$ to be in stable equilibrium, for instance:

$$\frac{k_C}{\beta} > nC\frac{1}{(z-\beta\delta_C)^{n-1}}$$

in which k_C/β is referred to as the effective elastic constant. If the force gradient is larger than the effective elastic constant, the cantilever becomes unstable and "jumps" onto the surface. This is the jump to contact discontinuity.

From the equations presented so far, the cantilever deflection $(\delta_C)_{ITC}$ and the tip–sample distance D_{ITC} at which the jump to contact occurs can be determined as:

$$(\delta_C)_{JTC} = \sqrt[n+1]{\frac{C}{(n\beta)^n k_C}}$$

$$D_{JTC} = \beta n(\delta_C)_{JTC}$$

These equations are valid for any kind of attractive force and are adapted to the main attractive forces, i.e. the Van der Waals and hydrophobic. No similar expression can be found for the jump–off contact, since, in this case, sample deformations and contact elastic theories actually determine both the distance and the force.

2.7. POTENTIAL SOURCES OF DATA DISTORTION

In the previous section, idealized elastic and plastic behaviour and the used analysis methods to calculate material properties from the displacement that occurs as a load is applied were discussed. A description of the tools necessary to make these measurements was also given. There are some aspects associated with these tools such as load frame compliance and tip shape anomalies that must be accounted for. There are other sources of error for depth sensing indentation measurements that are caused by the material and by the testing parameters. Unlike those associated with the apparatus, these distortions are material specific and therefore much harder to identify and correct. Accurate knowledge of the contact area is crucial in determining a truly representative hardness.

Some materials exhibit deformation behaviour that can lead to significant miscalculations of the contact area. Under certain loading conditions, some materials pile–up around the indenter increasing the contact area. Other materials experience sink–in, seeming to collapse from the area surrounding the indenter. There are other contact area problems that are introduced due to the scale of testing. Surface anomalies and roughness are not significant issues at the macro–scale but can influence nanoindentation considerably. Depending upon the scale of the roughness it is possible that only a fraction of the indenter tip is really in contact with the sample surface.

Certain materials exhibit time dependent deformation. Creep is defined as continued plasticity at a constant load. The continued deformation is often apparent in the hold at maximum load. The rate at which the probe comes in contact with a material can also have a significant influence on the indentation behaviour.

2.7.1. Contact area changes

Hardness measurements rely heavily on accurate determination of residual area at both micro and nanoscale. Even traditional hardness tests have to account for materials characteristics that might adversely affect the measured data. Anything that distorts the contact area makes the property values inaccurate. In this section, some of the potential sources of inaccurate estimation of contact area will be considered.

2.7.1.1. Pile–up and sink –in

At a particular depth penetration, the contact area depends not only upon the tip shape, but also on the elastic properties of the material. Materials with limited elasticity accommodate the volume of the indenter by plastic flow of the material, eventually piling–up around the tip (Fig. 29). This often happens in materials that are work hardened prior to testing. Elastic materials accommodate the indenter by longer–range elastic deformation. In such cases, the material appears to sink–in around the tip.

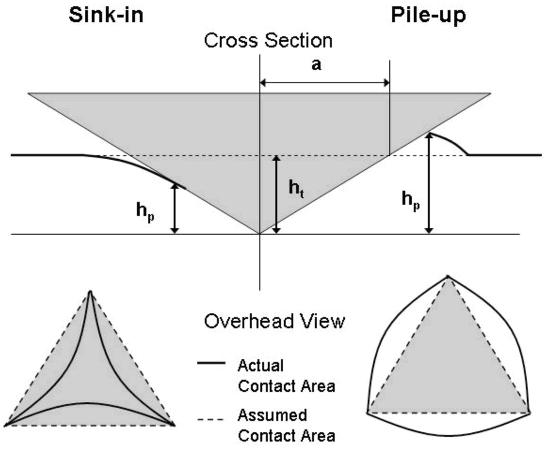

Fig. 29 – Schematic representation of pile–up and sink–in.The cross section of the indenter at the maximum load is reported in the top picture. The radius of the projected contact area based upon displacement is overestimated in sink–in and underestimated in pile–up.. This is more evident in the top view where dotted and solid lines indicate the assumed contact area and the real contact area, respectively.

The deformation zone is dependent upon the ratio of the elastic modulus to the yield stress (E/σ_Y).[61] When this ratio is large, the plastic zone often extends beyond the area in direct contact of the tip. When additional plasticity occurs near the indenter, the pile–up phenomenon appears. On the other hand, the deformation to accommodate the tip is more localized when the E/σ_Y ratio is small.

2.7.1.2. Roughness

Real surfaces are never ideally flat. Often there are even a variety of scales to the surface modulations. On a macroscopic scale, roughness has little effect on indentation testing, provided the indenter is large compared to the asperity size. In the nanometre regime, care must be taken to identify the influence of roughness of different spatial frequencies. Many of the surface modulations are significantly larger than the area of interest; hence locally it can be approximated as flat. But there are often surface features of the same order of magnitude and even smaller than the area of interest that influence the images or experiments being performed. The contact between two bodies is controlled not only by the material properties (elastic modulus and hardness) but also by topographical properties.

One of the most common methods for quantification of surface topography is the root mean square (RMS) roughness (R_q). This term is defined as:

$$R_q = \left[\frac{1}{n}\sum_{i=1}^{n}\left(z_i - \bar{z}\right)^2\right]^{\frac{1}{2}}$$

where n is the number of data points, z_i are the relative vertical heights, and $\bar{z}$ is the mean surface height. R_q describes the height distribution about the mean value. The mean surface height is defined by:

$$\bar{z} = \frac{1}{n}\sum_{i=1}^{n} z_i$$

The lack of information about the width and spacing of the asperities is the most obvious limitation of this roughness definition. There is no knowledge of the different roughness frequencies that often coexist. The only way to get these data is to scan the surface and display the image histogram to collect the whole information of the roughness. Roughness characterization needs a description of the length scale, the size of the image in relation to the largest feature size, and the processing performed on the image, in order to have a complete picture of what the value means.

2.7.1.3. Adhesion

All of the proposed model and the analysis technique at this scale assume that there is not significant adhesion between the probe and the sample. Some tip/sample pairs experience considerable adhesion. In these cases, the probe and sample remain in contact after the load goes to zero, and even require a significant negative force to return the tip to the original displacement (this phenomenon is present besides the jump off contact). Johnson, Kendal and Roberts[35] expressed the adhesive force as the energy balance between the loss of surface energy (U_s) and the increase in stored elastic energy (U_e). The lost surface energy can be expressed as:

$$U_s = -2\pi a^2 \gamma$$

where a is the radius of the projected area of contact and γ is the energy per unit contact area for both surfaces. The total energy balance can be written as:

$$\frac{eU_e}{da} = \frac{eU_s}{da} = -4\gamma\pi a$$

Adhesive forces increase the contact area over that predicted by the Hertz equation. The apparent load (P_1) is the combination of the applied load and the adhesive force ($P_1 = P + P_A$)

In the Hertz theory, the load is defined as:

$$P = \frac{4}{3}\frac{E^{*}a^{3}}{R}$$

where a is the contact radius, R is the radius of the object and E^{*} is the reduced Young modulus. Accordingly, the real applied load can be rewritten as:

$$P = \frac{4}{3}\frac{E^{*}a^{3}}{R} - \sqrt{8\pi a^{3}\gamma E^{*}}$$

This equation indicates that the actual radius is larger than that predicted by the Hertz equation. Hence also the residual contact area will be greater than the predicted one with the consequence of an underestimate of the hardness.

Johnson, Kendal, and Roberts[35] derived an important equation that enables to determine the effect of adhesive forces upon the contact size and the reduced modulus.

$$\frac{P}{P_A} = \frac{1}{3}\frac{a}{R}\sqrt{\frac{E^{*}a}{\pi\gamma}} - 1$$

A material that has a relatively small reduced modulus would increase the role of the adhesive force.

2.7.2. Time dependent properties

2.7.2.1. Creep

Nanoindentation assumes elastic–plastic behaviour and does not take into account any time dependence of mechanical properties. However, most materials have viscoelastic properties that can influence the load–displacement data. Creep, or time dependent plasticity is often observed in indentation testing as continuous deformation during the hold at maximum load. Dislocation glides, dislocation creep, diffusion creeps, and grain boundary sliding are responsible for this behaviour.[62] Usually more than one mechanism is active at the same time. Dislocation glide usually occurs at very high stress levels. The rate of creep is correlated to the ease of dislocation motion.

During indentation testing, some materials exhibit instantaneous jumps in displacement, or "pop–ins". Such displacements were recorded in the loading curves of semiconductors, ceramics, and metals.[63,64] This phenomenon has been shown to exist in both single crystals and polycrystalline material.[65] Different materials experience similar phenomenon for very different reasons. For example, in silicon the displacement excursion indicates a pressure–induced phase transformation while in aluminium the "pop–in" is due to surface oxide (Fig. 30). In some cases, there is more than one excursion in a single loading curve, often referred to as a staircase loading.

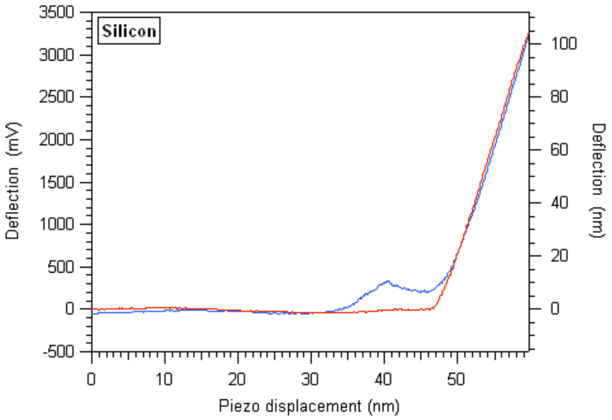

Fig. 30 – Observation of a step–in during indentation of silicon surface.

2.7.2.2. Impact velocity

The ability of materials to absorb load by elastic strain is not only correlated to the surface properties such as presence of oxides, grains, and boundaries dislocations, but it may also result from the testing parameters. Mann and Pethica[66] suggested that the impact velocity could influence the load at which the material yields. They performed indentation experiments on GaAs varying the rate at which the tip came into contact with the sample. They found that the impact velocity had a dramatic influence on the remainder of the deformation behaviour. When a low impact rate was used, there was considerable elastic loading in the sample.

3. MATERIALS AND METHODS

3.1.1. Materials

Human serum albumin (HSA) was purchased from Sigma.

Aminopropyltriethoxysilane (APTES) was purchased from Aldrich.

Phosphate Buffer Saline (PBS) was prepared by dissolving 2 g KCl, 2 g $KH_2PO_4 \cdot H_2O$, 80 g NaCl, and 15.6 g $Na_2HPO_4 \cdot 12H_2O$ in 1000 ml distilled water. The pH was adjusted at 7.4 with 10 N NaOH. The solution was heat–sterilized in autoclave at 121 °C for 20 min and stocked at 4 °C. The buffer was used after 1/10 dilution with distilled water.

Polystyrene and poly(methyl methacrylate) samples were kindly provided by Dr. A. Battisti of the University of Pisa.

Balinit C® coated steel samples were provided by Prof. R. Bassani of the Department of mechanical, Nuclear, and Production Engineering of the University of Pisa.

Silicon samples were purchased from Silchem in the form of wafers cut in the (100) crystallographic plane.

A standard gold sample was purchased from Veeco Instruments, Santa Barbara, Ca – USA.

The investigated oligopeptides were kindly supplied by Novetide Ltd., Israel and stocked at –18 °C. The oligopeptide sequences are H–KEK–NH_2 and Ac–RDKDR–NH_2, where K represents the lysine; E is glutamic acid; R is arginine; D is aspartic acid; H– ad –OH refer to the free N– and C–termini of the peptides; Ac– (CH_3CO–) and –NH_2 refer to the blocked N– and C–termini of the peptides.

Mica disks with a diameter of 9 mm (A1 quality) were purchased from Società Italiana Chimici, Roma, Italy.

Glass was purchased in form of microscope slides manufactured by Marienfeld GmbH (Germany).

3.1.2. Silicon surface activation with aminopropyltriethoxysilane

Silicon samples were treated sequentially with piranha solution (3:1 v/v sulphuric acid/ hydrogen peroxide), boiling dichloromethane, boiling methanol, and boiling acetone. Samples were then kept in boiling water for two hours, dried, and then heated at 200 °C. Finally, the samples were kept for 12 hours in 1.2 mM aminopropyltriethoxysilane

(APTES) solution in anhydrous toluene. Anhydrous toluene was prepared by distillation over a Na/K alloy under nitrogen atmosphere. Immediately before use, some ATPES was added to the distilled toluene and the flocculent precipitate was removed by filtration.

3.1.3. Sample preparation for AFM analysis

3.1.3.1. Surface cleaning

Surfaces were cleaned prior to the AFM measurements, using a large variety of methods. Every sample was polished with a nitrogen flux in order to remove contaminants such as dust or other impurities; chemical washings of the specimens were then performed to avoid organic contamination or in order to prepare the surface for functionalization. Common solvents used in during the experiments were methyl and ethyl alcohols, acetone, dichloromethane, ethyl ether.

3.1.3.2. Oligopeptide aggregates

Aggregation experiments were performed on ~9, 40, and 120 mM oligopeptide solutions in water and in PBS solution.

About 10 μl of solution were placed on the surface of a freshly cleaved mica sheet that was glued to a steel AFM sample plate. The solution was put over the mica by a syringe provided with a 0.2 μm nylon filter (Supelco) in order to remove solid contaminants and aggregates. The sample was incubated for 1 h under ambient condition to let it adhere to the surface; then the surface was washed with bidistilled water to remove unattached peptides and other impurities. Finally the sample was put under a Petri dish to avoid contamination by dust and left dry for about 2 h. All samples were analyzed in tapping mode using a RTESP (Veeco) cantilever with ~350 kHz resonant frequency, 125 μm length, and ~30 N/m elastic constant.

3.1.3.3. Synthetic polymer films

Polystyrene and poly(methyl methacrylate) were dissolved in toluene and dichloromethane, respectively, then a few drops were placed over a freshly cleaved mica sheet and spin coated at 3000 rpm for 1 minute. The expected thickness of films is about 2 μm.

3.1.3.4. Silicon functionalization

Silicon wafers were cut into small pieces in order to fit the microscope head. They were degreased by sequential immersion in boiling dichloromethane, boiling methanol, and boiling acetone prior to the functionalization procedure.

3.1.3.5. Protein binding

The protein binding over the silicon tip functionalized with APTES molecules was achieved putting the tips into a water solution of HSA for about 24h at room temperature.

3.1.4. AFM microscope

The microscope used in this thesis is a Multimode AFM microscope (Veeco Instruments, Santa Barbara, Ca – USA) equipped with Nanoscope IV controller, Picoforce controller and closed loop z piezoelectric translator for revealing small forces, and a thermal controller enabling to perform measurements at controlled temperatures ranging between –20 and +200 °C. Images consist of raster–scanned, electronic renderings of sample surfaces. There are three default image sizes: 128 x 128, 256 x 256, and 512 x 512 pixels. In addition, nine width–to–height aspect ratios may be specified by the user: 1:1, 2:1, 4:1, 8:1, 16:1, 32:1, 64:1, 128:1 and 256:1. The controller provides 16–bit resolution on all three axes, with three independent 16–bit digital–to–analog converters (DACs) in x and y for control of the scan pattern, scaling, and offset. Depending on the scanner in use, the Multimode can scan up to 200 μm laterally (in x and y) and 10 μm vertically (z axis).

3.1.5. AFM measurements

3.1.5.1. Morphological measurements

AFM morphological measurements were performed in tapping mode by using RTESP (Veeco) silicon tips with about 30 N/m elastic constant and 350 kHz free resonance frequency. Generally, topography and phase images were acquired. In some cases, friction and deflection maps were recorded.

3.1.5.2. Force–distance measurements

A special stiff probe with diamond–coated silicon tip with pyramidal shape ($\alpha = 15°$, $\beta = 25°$, $\gamma = 17.5°$) and rhomboidal base (DDESP, Veeco) was used in nanoindentation measurements. In particular, probes having k = 40.29 N/m and sensitivity = 42.46 nm/V, k = 40.75 N/m, sensitivity = 36.93 nm/V, and k = 50.1 N/m and sensitivity 34.88 nm/V were used for polystyrene, silicon, and Balinit C® samples, respectively. The total ramp size used in indentation experiments was 1 μm. A rate of 200 nm/s was chosen. The final indentation depth was measured from force–distance curves.

3.1.5.3. Protein swelling measurements

Triangular NP tips (Veeco) with low elastic constant (0.06 N/m) were used in order to achieve the sensitivity needed for measuring the small forces (hundreds of pico Newtons) involved in the protein swelling.

3.1.6. Contact angle measurements

Contact angle measurements were performed with a home–made microscope equipped with a digital camera. This system is composed by a Zoom 6000 (Navitar, USA) with magnification ranging from 0.7x to 4.5x, mounted on Powershot S70 (Canon, Japan) digital photo camera. The digital camera is attached to the system via an adaptor that fits both the 30 mm microscope eyepiece port and the C mount of the digital camera. This adapter presents a magnification factor of 0.75x. A greater resolution is obtained combining the Navitar zoom with a 2x tube and a 12x final objective. The system reaches a total magnification of 243x. The whole assembly is mounted over a stand provided with a solid heavy base; this stand allows for coarse and fine translations in the *x* and *y* directions and also to tilt the camera from 0 to 90° (Fig. 31). The droplet digital images were acquired with the camera and processed with ImageJ, a public domain, Java image–processing program developed at the National Institutes of Health (USA).

Fig. 31 – Photo of the home–made system used for acquiring digital optical images.

4. RESULTS AND DISCUSSION

4.1. SUBSTRATES USED IN AFM EXPERIMENTS

Since AFM does not require the substrate to be conductive, the choice of substrates is almost unlimited. Both glass cover slips and cleaved mica sheets have been used to adsorb various macromolecules and organelles with varying degrees of success. The biopolymers to be imaged in the AFM are normally dissolved in aqueous solution and then deposited onto the substrate. Compared with the size of the molecules to be analysed, the substrate has to be flat. Furthermore, ease of preparation is required in order to reliably achieve flat surfaces. However, in some of the experiments, in particular in those involving functionalization and growth of self–assembled layers, the choice of the substrate has been mostly driven by the need to attain an efficient and correctly ordered coverage of the substrate. The most useful surfaces adopted for the investigation of samples are glass, gold, mica, and silicon.

Glass

Glass is flat enough for imaging cells or other large and relatively thick samples. Apart from cells, also large molecules like tubulin molecules, chromosomes or cell organelles can be analysed over this surface. On the other hand, glass is generally too rough for reliable visualization of DNA or small proteins such as fibrinogen and so on, especially under fluids. They are best suited for all experiments in which visible light is transmitted across the sample, as in scanning near field optical microscopy (SNOM) or in the combined optical microscopy and SPM. For such a reason, we have restricted ourselves to use glass only in some experiments. Before use, organic contaminants, dust, and other particles are removed by washing with concentrated HCl/HNO_3 (3:1 v/v) and 5 times for 1 min with Millipore water in an ultrasonic bath (50 kHz). This process makes the cover slips clean and relatively smooth (RMS–roughness ~ 0.5 nm).

Silicon

Silicon wafers with orientation 111 or 100 present flat surfaces over large areas. Those specimens are used in a great variety of experiments. Silicon is a very hard material and present a typical RMS roughness of only ~ 0.1–0.2 nm, which makes it suitable to be used in surface functionalisation experiments, especially using siloxane molecules as

APTES. As a matter of fact, silicon wafers are the substrates of choice when syloxane layers are to be grown trough self–assembly on a surface.

Gold

Gold surfaces can be easily prepared by vapour deposition onto glass and mica (previously prepared with a layer of chromium in order to get better adhesion). Typically, flatness of the so–deposited gold layers is not excellent, being heavily affected by the structural and morphological nature of the underlying layers, but still acceptable for most of the experiments of interest in this work. Gold is chemically inert against oxygen and stable against radicals. It binds functional organic thiols and disulfides with high affinity; the functionality can be used to covalently attach biological macromolecules.

Mica

Also known as Muscovite mica, Isenglass, or Potash mica is a phyllosilicate mineral of aluminium and potassium with formula: $KAl_2(AlSi_3O_{10})(F,OH)_2$. Mica undergoes perfect basal cleavage yielding remarkably thin laminas (sheets), which are often highly elastic. Muscovite melts at approximately 1320°C, has a Mohs hardness of 2 – 2.25. It can be colourless or tinted through greys, browns, greens, yellows, or (rarely) violet or red, and can be transparent or translucent. The minimum step size which can be observed on the surface is the thickness of an individual layer (1 nm) and the hexagonal lattice constant within the layers, which can be used for AFM calibration, is 0.52 nm. The RMS roughness is 0.06 ± 0.01 nm. making such a substrate an excellent choice for high resolution AFM imaging. Fig. 32 shows a step between two planes on a mica sheet, as observed in a topography AFM scan acquired in the contact mode. This image clearly demonstrates the capability of our instrument to capture details on the nm scale.

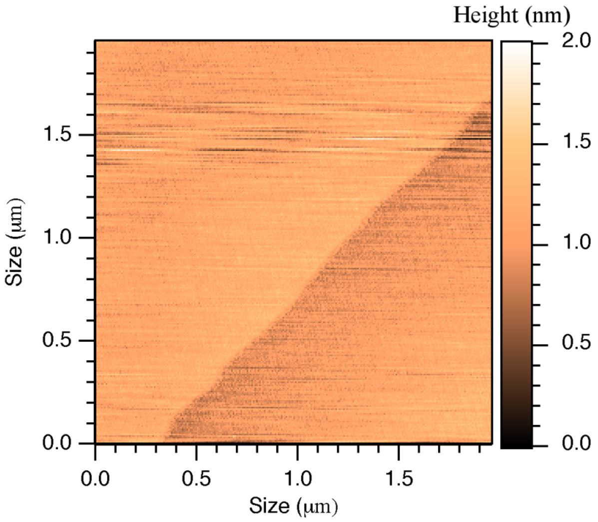

Fig. 32 – Mica surface scanned in contact mode presenting a 15 Å tall diagonal step.

Mica has been successfully used in many studies, especially for AFM imaging of double stranded DNA and DNA–protein complexes, protein arrays, and densely packed proteins. Although the mechanism by which macromolecules absorb to this substrate still remains poorly understood, a large number of protein samples adhere tightly to this surface.

4.2. AFM OF OLIGOPEPTIDES

Self–assembling oligopeptides are a new class of biomaterials, which have many potential applications in the field of biomedicine and pharmaceutical areas due to their biocompatibility and biodegradability. Those peptides are able to form three–dimensional matrices so they represent an ideal constituent for tissue engineering and carriers in drug delivery systems. Accordingly, an investigation was started on the self–assembling characteristics of selected oligopeptides. The sequences of the investigated oligopeptides are H–KEK–NH_2 and Ac–RDKDR–NH_2 (Fig. 33), where K represents the lysine; E is glutamic acid; R is arginine; D is aspartic acid; H– refers to the free N–terminus of the peptides; Ac– (CH_3CO–) and –NH_2 refer to the blocked N– and C–termini of the peptides. These oligopeptides pertain to a particular class first studied by Zhang *et al.*[67.] They consist of alternating hydrophilic and hydrophobic amino acids; the hydrophilic surface of the molecule has alternating + and – charged amino acid residues. This charge conformation permits to the peptide to self organize in particular shapes and morphologies.

Concentration is a key parameter in controlling the aggregation of self–assembling oligopeptides and our study was addressed to find a relation between the aggregate size, as evaluated by AFM and the concentration of the starting solution.

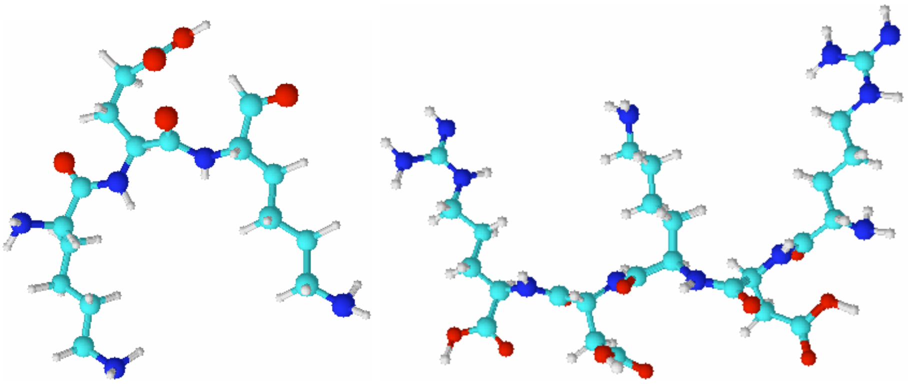

Fig. 33 – 3D schematic representation of the tripeptide H–KEK–NH_2 (left) and the pentapeptide Ac–RDKDR–NH_2 (right).

Hence our study was focused on the analysis of the presence of aggregates and of their average size with the aid of the atomic force microscope. Samples were prepared by casting of oligopeptide aqueous solutions on mica plates. Oligopeptide concentrations ranging between ~10 and ~120 mM, either in water or in pH 7.4 PBS buffer were used. AFM measurements were performed in tapping mode by using silicon tips (RTESP) with about 30 N/m elastic constant and 350 kHz free resonance frequency. Measurements in tapping mode allow for acquiring both topographical and phase images. Phase images give information on the mechanical properties of peptide aggregates: in fact they are related to the surface viscoelastic response to tip oscillations. Soft materials like peptide aggregates, respond in a different way with respect to mica and buffer salt residues. Distribution of the phase shift during scanning over the sample surface, reflects the distribution of the sample material characteristics, outlining local variations of the surface viscoelastic properties.

4.2.1. H–KEK–NH_2 tripeptide

At the lowest concentration (9.7 mM in water), the tripeptide formed small globular aggregates (clear regions) with diameters ranging from 5–10 nm of the smallest ones to ~30 nm of the biggest aggregates. These aggregates are resolved with difficulty even by the AFM (Fig. 34). Indeed, the collected images are not clear enough: especially the topography seems to be a little "dirt". This result was attributed to the residual presence of water. A better contrast was obtained in the phase image. Moreover, this map highlight some clear spots (shown by cyan arrows) that cannot be attributed to oligopeptide aggregates (dark spots) because they are harder compared to organic aggregates. In any case, AFM phase imaging demonstrates itself a viable technique to detect the presence of aggregates as small as 5 nm.

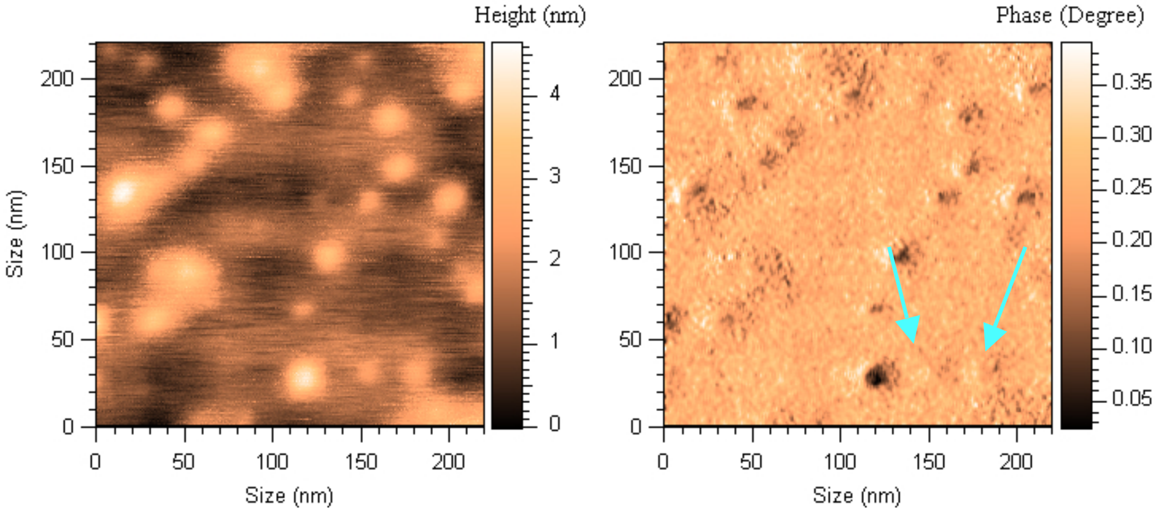

Fig. 34 – AFM topography (left) and phase (right) maps (220x220 nm) of 9.7 mM tripeptide solution evaporated on mica.

The AFM maps of the aggregates obtained by evaporation of 37 mM tripeptide solution in pH 7.4 PBS buffer are presented in Fig. 35. In this case, the same features can be distinguished in both topography and phase images. It is worth noting that the topography map reveals a lot of structures over the mica surface, although it is not possible to separate clearly oligopeptide aggregates from the rest of the background buffer salts. On the other hand, the phase image clearly shows the domains in which tripeptide aggregates are present. In fact, the aggregates are softer structures than PBS salts and the mica surface; they appear as darker spots because of their different viscoelastic properties. The phase image shows that the tripeptide molecules self assemble forming globular or slightly elongated shapes, with comparable dimensions ranging around a mean value of ~40 nm. Apparently, the presence of the salts affects the size and the size distribution of tripeptide aggregates. Very likely, the salt microgranules act as nucleation centres. In accordance, oligopeptides tend to aggregate near these saline nuclei when the salt is present in the starting solution.

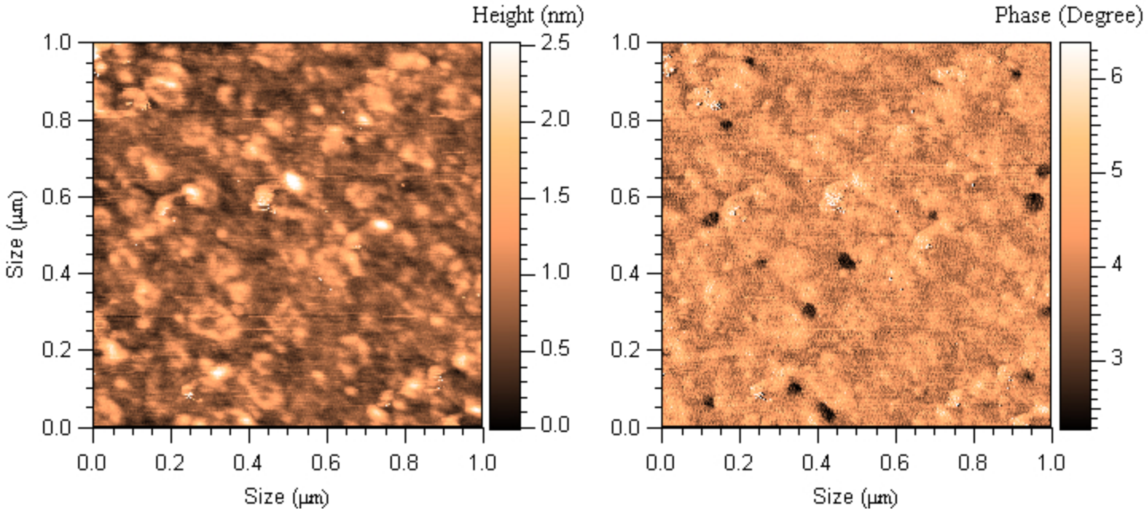

Fig. 35 – AFM topography (left) and phase (right) maps (1.0x1.0 μm) of 37 mM tripeptide PBS solution evaporated on mica.

The bottom left area of Fig. 35 is zoomed in Fig. 36. Here, all small features and details can be appreciated also in the topography map. In particular, cyan arrows highlight the presence of KEK aggregates. In fact, the tripeptide aggregates have a rather different structure as compared to the rest of the image, where buffer salts, possibly some impurities, and surface irregularities are present. Anyway, the maximum contrast is obtained again in the phase image.

A further zoom (Fig. 37) emphasizes the difference of peptide morphology in comparison with the background. In the topography map, arrows highlight the presence of two tripeptide aggregates. The organic structures reveal small features and a more complex organization, compared to relatively flat salt surfaces. Their shape is not really globular, but rather irregular and elongated.

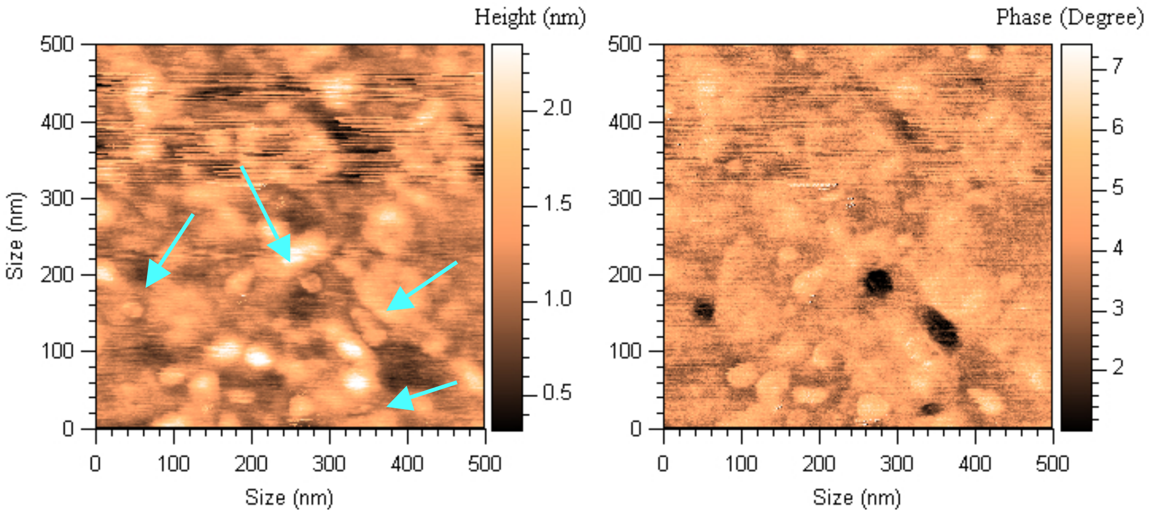

Fig. 36 – AFM topography (left) and phase (right) maps (500x500 nm) of 37 mM tripeptide PBS solution evaporated on mica.

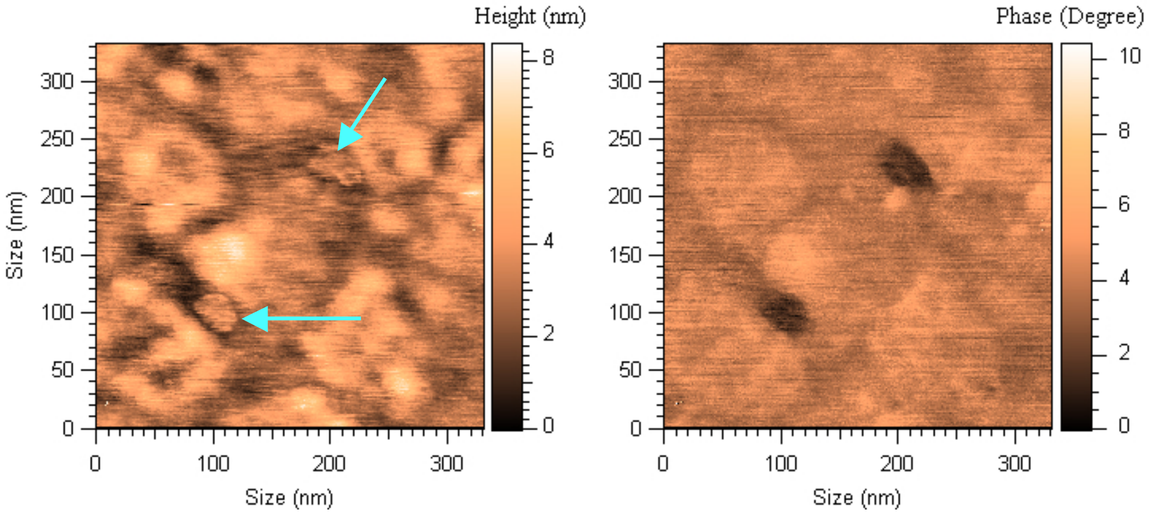

Fig. 37 – AFM topography (left) and phase (right) maps (330x330 nm) of 37 mM tripeptide PBS solution evaporated on mica.

Indeed, the oligopeptide aggregates are always surrounded by salt structures as demonstrated by the 3D representation of the same topography of Fig. 37 (Fig. 38). The cyan circles highlight two KEK aggregates that are surrounded by salt structures that stick out of the aggregates. A completely different situation was found when aggregates were formed by evaporation of a tripeptide solution in bidistilled water (i.e., without salt). In this case, the background surface was almost flat (except for the black lines that represent some artefacts after filtering the images). Tripeptide aggregates are the only visible structures over the mica surface (Fig. 39). The aggregate size is essentially distributed around two values: The biggest globular structures have a diameter of about 180 nm whereas the smallest aggregates have an approximate size of 20 nm. This observation is roughly confirmed for all similar samples.

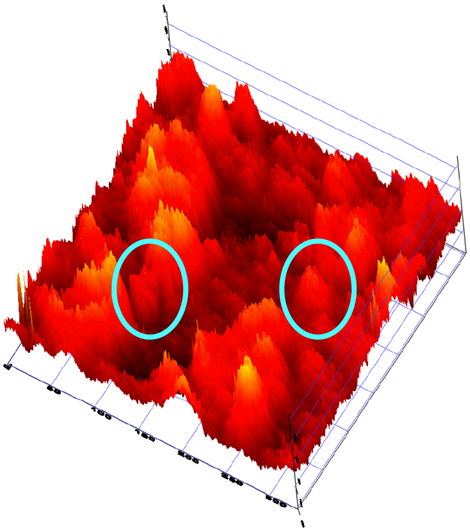

Fig. 38 – 3D topography of 37 mM tripeptide PBS solution evaporated on mica.

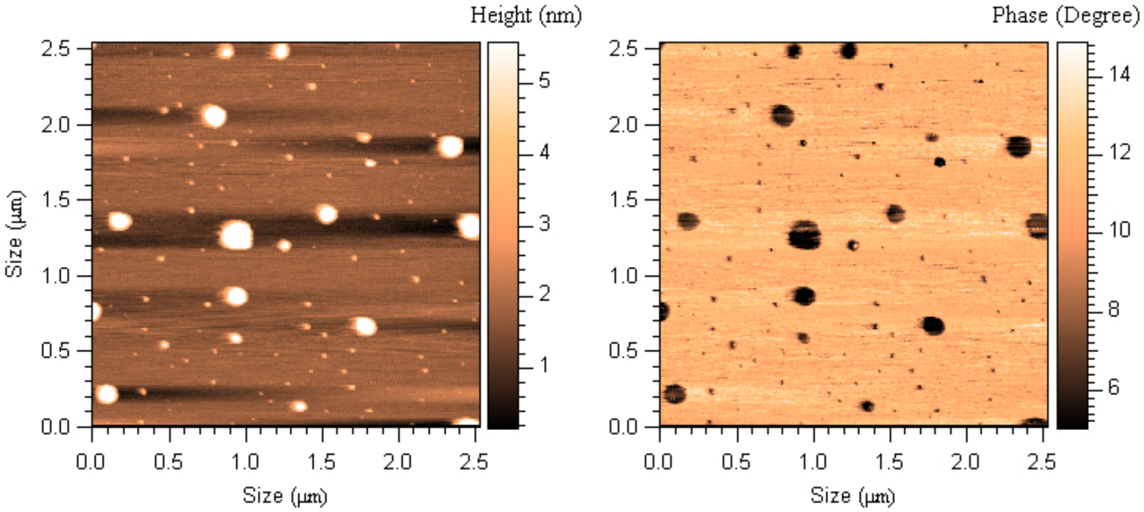

Fig. 39 – AFM topography (left) and phase (right) maps (2.5 x 2.5 µm) of 118 mM tripeptide water solution evaporated on mica.

Apparently, bigger aggregates and larger size distribution are formed in water than in PBS solution. This effect was attributed to the absence of the nucleating effect caused by inorganic salt crystals. It is worth analyzing the maps recorded on mica surface after evaporation of 37 mM tripeptide solution (Fig. 40). There is a homogeneous distribution of globular oligopeptide aggregates having a broad size distribution peaking at about 10 and 60 nm. In this case, only a small amount of inorganic salts is present on the scanned surface. The shape of the aggregate at the top of the topography, highlighted by the cyan arrow is rather unusual: it is elongated and to some extent it looks like a pear. However, a closer look at the phase image clarify that this shape is composed by the peptide aggregate itself (twin bobbles aligned vertically on the left of the structure) and the salt that appears brighter in the phase image because it is harder than organic materials.

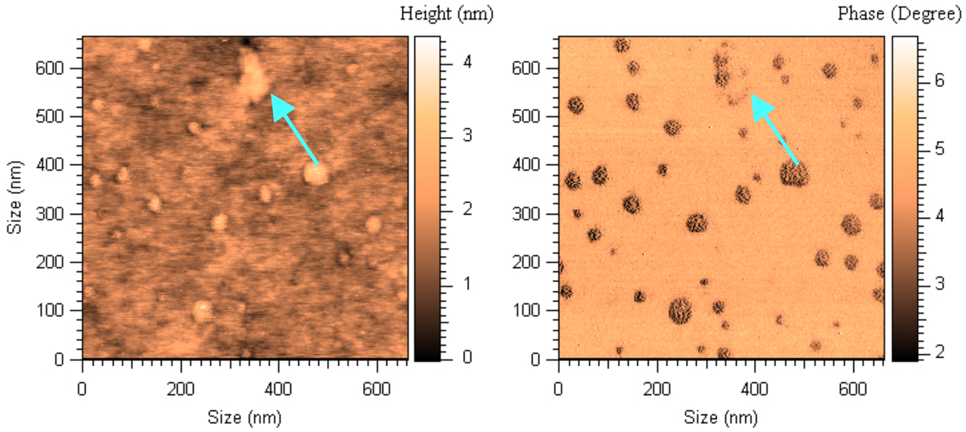

Fig. 40 – AFM topography (left) and phase (right) maps (660 x 660 nm) of 37 mM tripeptide PBS solution evaporated on mica.

A completely different situation is detected in the phase image of aggregates formed by evaporation of concentrated (118 mM) tripeptide PBS solution (Fig. 41). The buffer salt, present in the top right corner as a long linear bright construction is the upper limit for peptide structure. At this concentration and in the presence of inorganic salts, KEK aggregates (dark regions in the phase map) form elongated irregular shapes (30x300 nm) almost perpendicular to the salt structure that can be seen at the left top corner of Fig. 42.

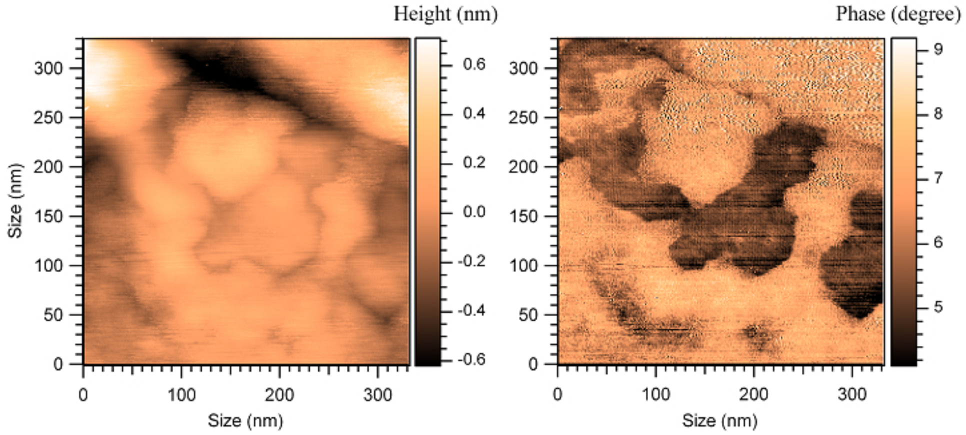

Fig. 41 – AFM topography (left) and phase (right) maps (330 x 330 nm) of 118 mM tripeptide PBS solution evaporated on mica.

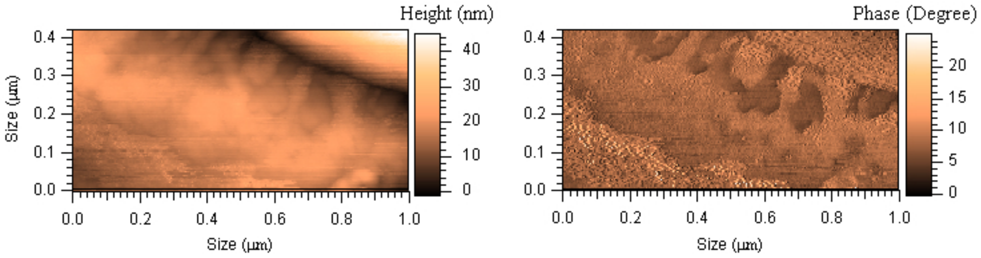

Fig. 42 – AFM topography (left) and phase (right) maps (1.0 x 0.42 µm) of 118 mM tripeptide PBS solution evaporated on mica.

Almost all dark structures (tripeptide) in the phase map are oriented towards the big salt formation in the top right corner of the image. The peptide aggregates are about 30 nm wide and 280–300 nm long. Again, all tripeptide aggregates are formed next to inorganic salt formations.

4.2.2. Ac–RDKDR–NH$_2$ pentapeptide

Evaporation of the pentapeptide PBS solution gives rise to the development of fibril–like elongated patterns. Initially, proto–structures constituted by aligned small (~12 nm) aggregates are formed (Fig. 43). The indicated structure is more easily identified as a row of orange–yellow peaks in the 3D topographic image (Fig. 44).

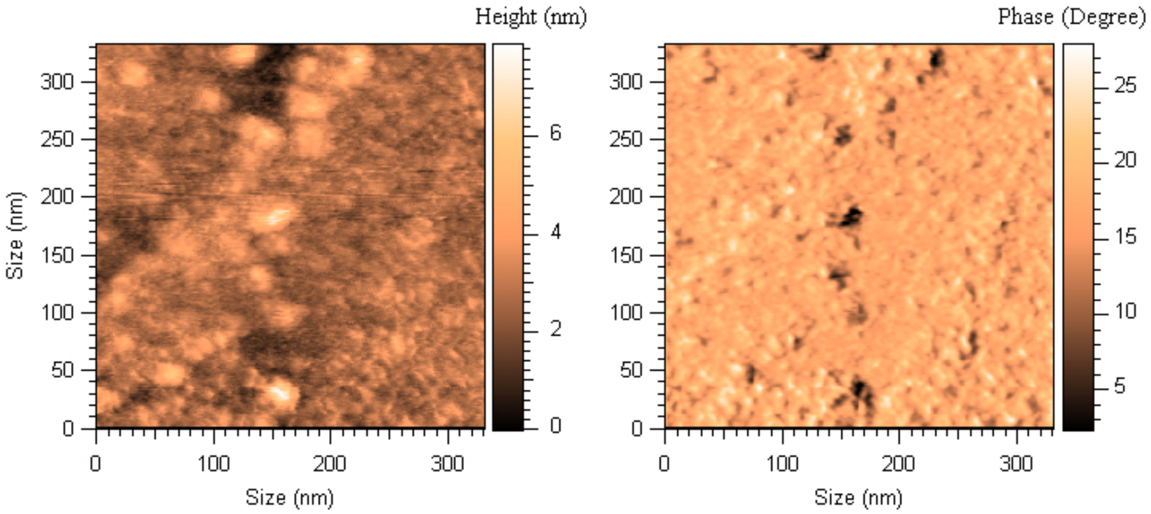

Fig. 43 – AFM topography (left) and phase (right) maps (330x330 nm) of proto–aggregates formed by evaporation of 4.3 mM pentapeptide PBS solution on mica.

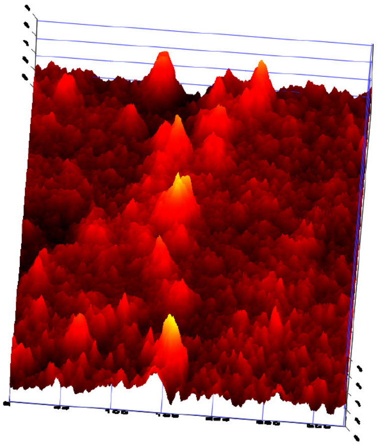

Fig. 44 – 3D AFM topography of the proto–aggregates formed by evaporation of 4.3 mM pentapeptide PBS solution on mica.

After a while, the proto fibrils join together to form filaments (Fig. 45). Once more, the pentapeptide linear structure is better resolved in the phase image because of the higher contrast. The dimension of this fibril is quite large in topography (about 80 nm), but this is partially affected by the relatively low resolution achievable in topography, where convolution with the tip size affects the results. In the phase image, where contrast mechanisms may act to enhance the effective space resolution, the dimension measured is more reasonably ~30 nm.

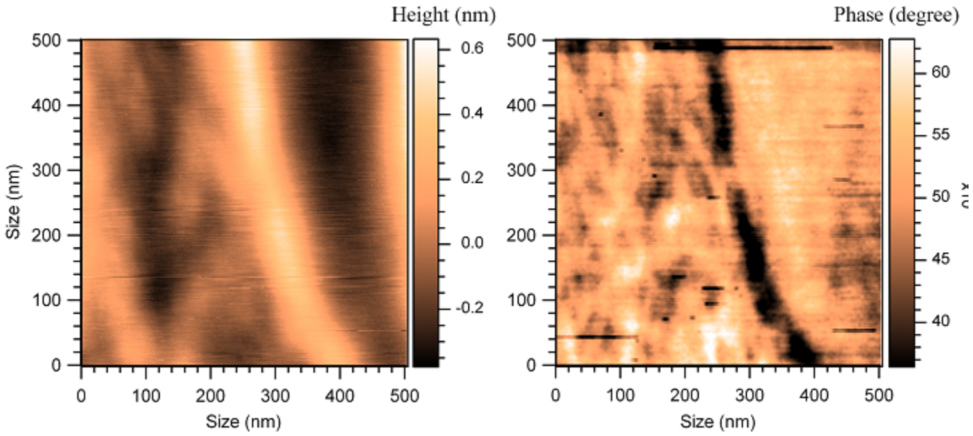

Fig. 45 – AFM topography (left) and phase (right) maps (330x330 nm) of a fibril formed by evaporation of 4.3 mM pentapeptide PBS solution on mica.

Also in the case of the pentapeptide, the presence of inorganic salts in the starting solution greatly influences the self–aggregation process. Indeed, Fig. 46 shows a pentapeptide filament embedded with salt structures in the right top corner, in the middle, and in the left of the image. The presence of the salt in the starting solution is expected to greatly affect also the behaviour of the pentapeptide. Indeed, measurements on peptide aggregates grown in the presence of salt confirmed such hypothesis.

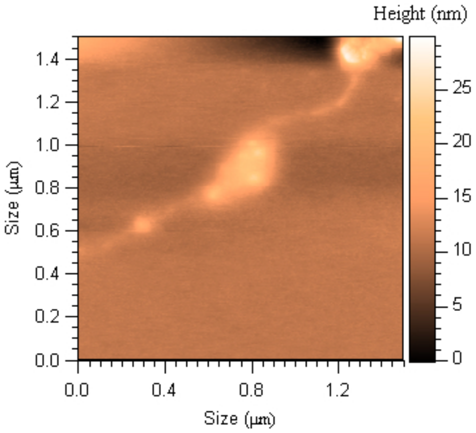

Fig. 46 – AFM topography of a fibril formed by evaporation of 4.3 mM pentapeptide PBS solution on mica.

These results confirm that there is a very intimate relationship between salt formations and aggregate development.

In the absence of PBS salts, evaporation of the pentapeptide solution provided the following topographic images:

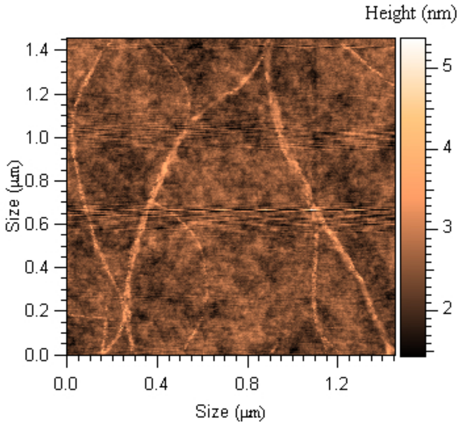

Fig. 47 - AFM topography (left) and phase (right) maps (1.4x1.4 µm) of fibrils formed by evaporation of 5.1 mM pentapeptide water solution on mica.

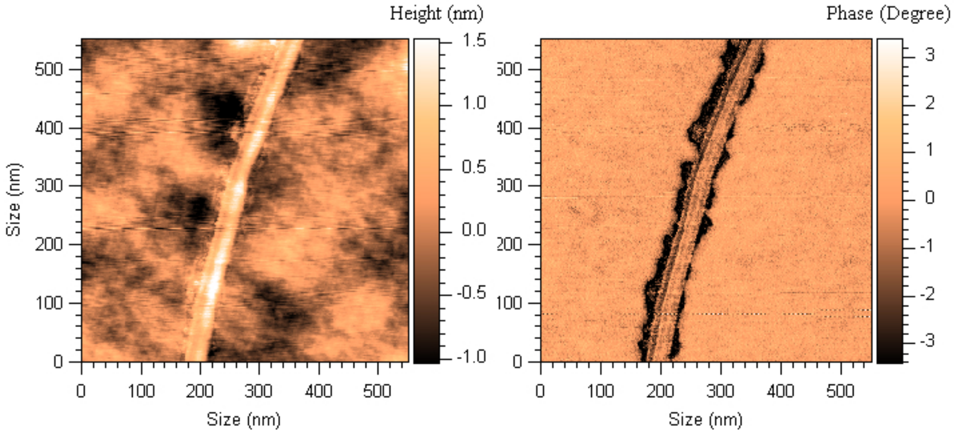

Fig. 48 - AFM topography of a fibril formed by evaporation of 5.1 mM pentapeptide water solution on mica.

4.3. NANOINDENTATION AND MECHANICAL PROPERTIES

Tissues are an important class of materials that are composed in a hierarchical structure at both macroscopic and microscopic scales. It is well known that the specific biological and chemical composition of tissues is critical for tissue function. However, the structural organization is just as important, if not more so, as this unique framework defines the three–dimensional shape of the tissue at multiple length scales. Typically, this framework consists of a complex network of structural and bioactive macromolecules such as proteins, proteoglycans, and glycosaminoglycans known in general as the extracellular matrix (ECM). The ECM has multiple functions but, in general, provides adhesion sites for the tissue–specific cells, largely controls the mechanical properties of the tissue, and serves as an organizational template that guides and maintains crucial spatial relationships between various cell types to achieve appropriate tissue function. Fig. 49 illustrates how hierarchical organization in tissues gives rise to a wide variety of biological functions.[68]

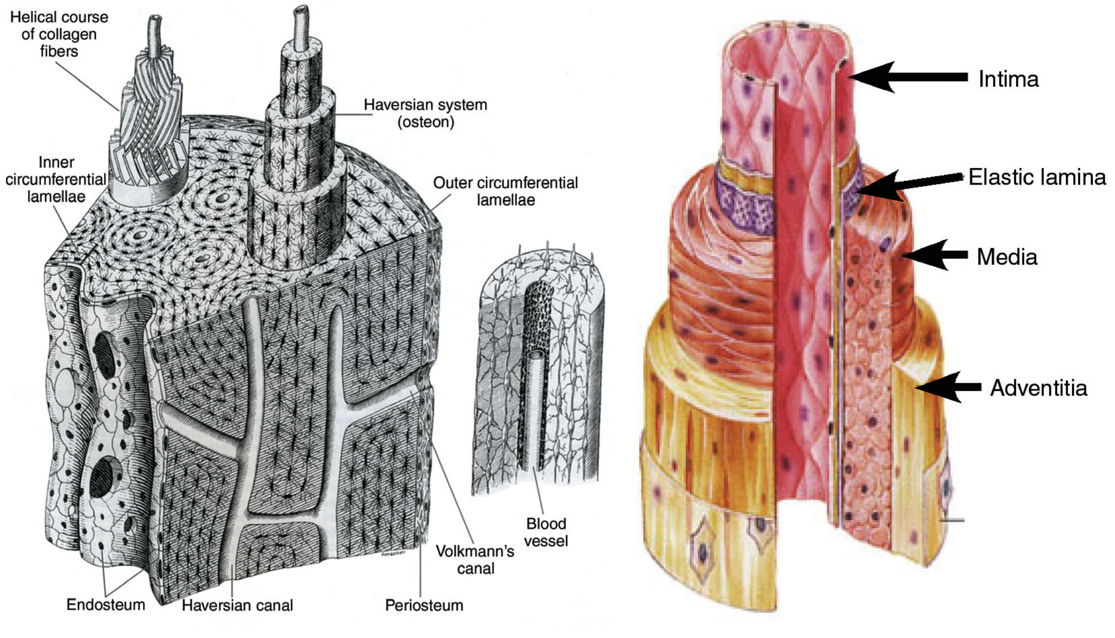

Fig. 49 – Schematic representation of the hierarchical organization of bone tissue (left) and artery wall (right).

Understanding of new materials at the molecular level has become increasingly critical for a new generation of nanomaterials for nanotechnology, namely, the design, synthesis and fabrication of nanodevices at the molecular scale. In particular, the mechanical characterization of tissues and other biological material is of outmost importance in the field of biomaterials and regenerative medicine.

Nanotribology is a new promising technique in which wear, adhesion, friction, hardness, *etc*. are studied at a nanoscopic level. In this wide research field, nanoindentation, also know as depth–sensing indentation (DSI), was addressed for a better comprehension of surface properties of machined surfaces, particularly in the case of intrinsically heterogeneous blends and alloys. DSI is a method that records the displacement of the indenter probe when a known load is first applied and then removed. The probe tip has a very well defined area function based on penetration depth, enabling calculation of the area of contact based on piezo displacement that can be readily acquired by AFM. By this new technique, loads as small as tenths of micro Newtons and depths as small as fractions of nanometre can be measured. In nanoindentation experiments, the tip is forced to the surface in order to leave a mark and both cantilever deflection and piezo movement are recorded. The collected information can be used for determining important material properties such as, hardness H and Young modulus E.

Continuing development in indentation models and analysis will increase the usefulness of this technique for the characterisation of biomaterials, particularly for tissue engineering applications. There are many advantages in using AFM for nanoindentation experiments such as:

- Possibility to check mechanical properties at very small scales
- Rapid measurements over different points of the sample surface
- Determination of Hardness and Young modulus without imaging
- All data can be collected by a single force distance curve

Furthermore, the high space resolution allowed by AFM and the aforementioned ability to apply and detect extremely small loads on areas as large as the tip cross section enable mechanical measurements to be carried out in a regime where most of the well established theories developed and tested for macroscopic indentation loose their validity, giving rise to a variety of “size effects” not yet completely understood. As a consequence, data interpretation can be rather complicated, while ensuring the ability to better understand the material features at the nanometre level.

Nevertheless using AFM for indentation experiments, presents also limitations such as:

- Long calibration times are required
- Data extraction is not straightforward
- Only small loads can be achieved

In the present thesis we report the results obtained in preliminary DSI experiments performed on soft polymeric materials such as, polystyrene, PMMA and silicon, and on Balinit C®, a very hard coating of tungsten carbide applied to the surface of specialty steel to prevent wear.

4.3.1. Theory of Hardness

Hardness measurements are one of the most common methods to test the mechanical properties of materials. These tests are quick and easy, repeatable and inexpensive. Since the early 1800's, when Friedrich Mohs[69] first introduced scratch testing, relative hardness has been used to characterize mechanical properties. Almost a century later Johan Brinell introduced a test in which a hard sphere was pressed into a specimen. The ratio of the applied force and the contact surface area was defined as the hardness, a definition still used today. Many researchers such as Knoop, Vickers, and Rockwell modified this test, but the basic principle is the same.

Indentation is the most commonly used technique to measure the mechanical properties of materials because of the ease and speed with which it can be carried out. At the beginning of the 20th century, indentation tests were first performed by Brinell, using spherical and smooth balls from ball bearings indenters to measure the plastic properties of materials.[70] The Brinell test was quickly adopted as an industrial test method soon after its introduction and prompted the development of various micro and macro indentation tests. Traditional indentation tests involve optical imaging of the indentation mark (Fig. 50).

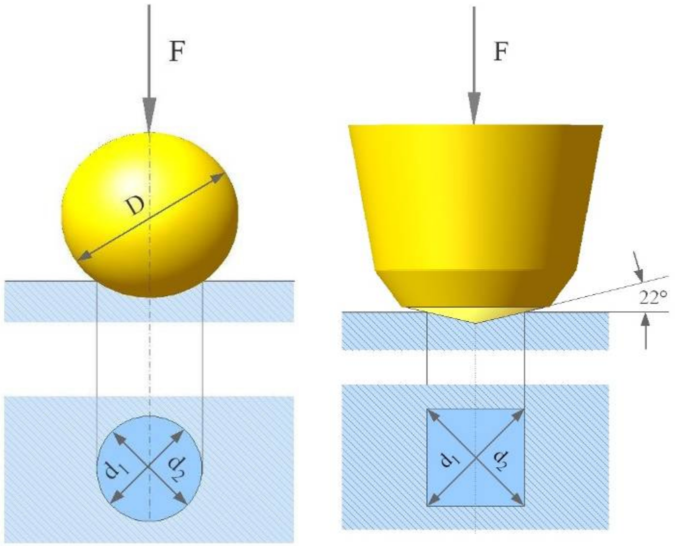

Fig. 50 – Schematic representation of Brinell (left) and Vickers (right) hardness test. A sphere with a diameter D or a pyramidal tip with definite geometry is pressed by force F on the sample surface.

In the conventional analysis of Vickers, Knoop, and Brinell tests, the hardness H is calculated as described in Eq. 6:

$$HV = \frac{1.854P}{d_1 \cdot d_2} \quad HK = \frac{3.557 \cdot 10^{-2} P}{l^2} \quad HB = \frac{2P}{\pi D \left(D - \sqrt{\left(D^2 - d^2 \right)} \right)} \qquad \text{Eq. 6}$$

Factors highlighted in red are determined directly by measuring the mark left on the surface by the indenter. This clearly poses a lower limit to the indentation scale, since space resolution in optical microscopes is ruled by diffraction, and cannot exceed about half the wavelength of the illuminating radiation. During the last two decades, the scope of indentation testing has been extended down to the nanometre range. This was achieved mainly through the development of instruments able to continuously measuring load and displacement during an indentation.[71] In recently developed systems, loads as small as one nano Newton and displacement of about 0.1 nm can be accurately measured. On the other hand, the recognition in the early 1970s that elastic modulus could potentially be measured from an indentation load–displacement curve greatly promoted the development of instrumented indentation testing methodologies. In recent years, the study of mechanical properties of materials on the nanoscale received much attention, as these properties are size–dependent. These studies were motivated partly by development of nanocomposites and application of nanometre thick films for electronics or special metal coatings, and partly by newly available methods of probing the mechanical properties of small volumes of material. From the load–displacement data, a wealth of information regarding mechanical properties can be determined without imaging the indentations.
The theoretical response of different materials to a load–unload cycle is shown in Fig. 51.

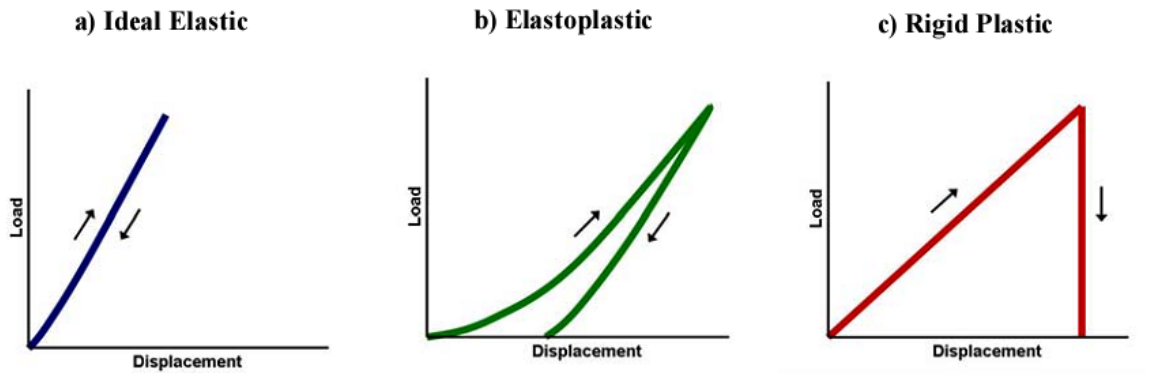

Fig. 51 – Representative load–displacement curves of completely elastic (a), elastoplastic (b), and ideally plastic (c) materials.

In the nanometre regime, atomic scale heterogeneities can have a dramatic effect on hardness tests. Factors such as location of the indent, surface preparation, surface orientation, the radius of the indenter, and even the tip material play important role in the information gathered. The mechanical response of small volumes of material is more sensitive to often–overlooked characteristics such as the surface energy and dislocation density. Also oxides, absorbed species, compositional changes, and even exposure to the environment can have significant local influence on mechanical properties.

Very low loads yield very small indents that are beyond the resolution of optical techniques, whereas other imaging apparatuses such as SEM make the tests not really convenient. Another hundred years after Brinell, the way in which we evaluate the hardness of a material is again redefined.

The mechanical properties measured most frequently using indentation techniques are the hardness, H, and the elastic modulus, E. As the indenter is pressed into the sample, both elastic and plastic deformations occur, which results in the formation of a hardness impression conforming to the shape of the indenter. During indenter withdrawal, only the elastic portion of the displacement is recovered, which facilitates the use of an elastic solution in modelling the contact process.

Fig. 52 shows a typical load–displacement curve and the deformation pattern of an elastic–plastic sample during and after indentation: h_{max} represents the max displacement at the peak load (P_{max}); h_c is the contact depth and it is defined as the depth of the indenter in contact with the sample under load; h_f is the final displacement after complete unloading; S is the initial unloading contact stiffness.

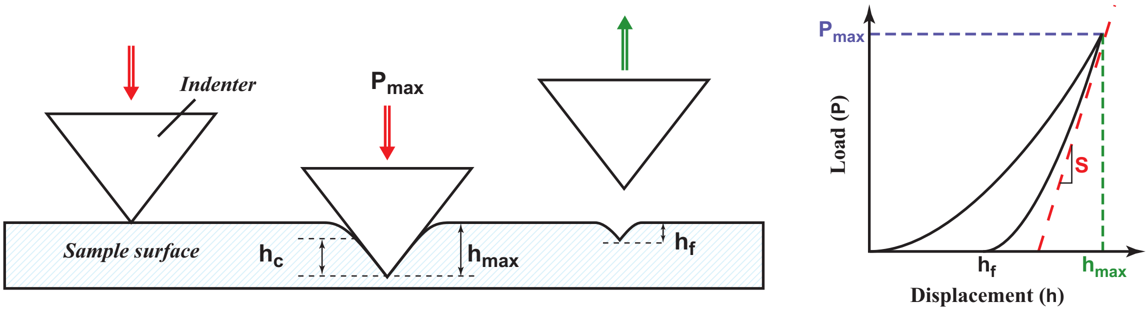

Fig. 52 – Schematic representation of the loading–unloading cycle over the sample surface and relevant material response (left); Contact zone of the force–distance curve obtained in an indentation experiment (right).

In the literature, the hardness of a material is defined as the resistance of the material to a plastic deformation. On the other hand, from a theoretical point of view, nanoindentation hardness is defined as the indentation load divided by the projected contact area of the indentation. It represents the average pressure that a material can withstand under load. Hardness can be obtained from load–displacement curve, at the peak load, as $H = P_{max}/A_C$ where A_C is the residual contact area. P_{max} is obtained by the Hooke's law ($P = kx$), where k is the elastic constant of the cantilever calculated as $k = M_e\rho_c bhL\omega_{vac}^2$; ω_{vac} is defined as $\omega_{vac}=\omega_f(1+\pi\rho_f b\Gamma(\omega_f)/4\rho_c h)$; h is the thickness, b and L are cantilever width and length, respectively (Fig. 8); ρ_c is the cantilever density; $M_e=M\cdot 0.2427$ is the effective mass; ρ_f is the fluid density (air 1.18 kg/m^3); $\Gamma(\omega) = \rho_f\omega b^2/4\eta$ is the hydrodynamic function; η is the fluid viscosity (air $1.86\cdot10^{-5}$ kg m^{-1}s^{-1}).

By substituting a few constants, one gets:

$$k = 0.19\rho_f b^2 LQ\Gamma\omega_f^2$$

A special stiff probe with diamond–coated tip and high elastic constant (DDESP, Veeco) was used in nanoindentation measurements. The tip shape is a pyramid (α = 15°, β = 25°, γ = 17.5°) with a rhomboidal base.

The maximum force was calculated from the maximum deflection of the cantilever recorded by the detector. The system sensitivity was found by performing a test measure over a hard material (in the present case an alumina single crystal substrate) in order to get the numerical factor of the instrument in nm/V; this factor represents the voltage change of the system reading the photodiode (the bending motion of the cantilever) for a tip deflection of 1 nm.

The contact area can be determined from the knowledge of the penetration depth gathered from loading–unloading curves. In fact, the shape of the indenter determines the relationship between penetration depth h_f and contact area A_c. Before starting nanoindentation experiments, a new expression was derived ($A_C = h_f^2 C_{tip}/2$) in order to take into account the morphology of the diamond–coated tip.

4.3.2. Experimental procedures

Essentially, AFM indentation tests were performed using the force–distance technique. The experiments were carried out by setting the approach speed and the ramp size. A cantilever calibration test was made preliminarily to determine accurately its elastic constant.

Calibration of the cantilever is a key point in quantitative force analysis such as in molecular recognition and chemical force microscopy. It is also very important for mechanical studies in which it is necessary for the calculation of the load. In fact, in a first approximation the load applied to the samples is obtained considering the cantilever as a perfect spring with k elastic constant. When in contact with the sample, the cantilever is deflected by Δz. Hence, following the Hooke’s law, the force applied to the sample can be calculated as:

$$F = k \cdot \Delta z$$

The elastic constant of the cantilever can be evaluated in a large variety of modes ranging from pure theoretical indirect methods to experimental techniques that can, however damage the tip or the cantilever if not properly executed. Accordingly, it is better to use methods that do not compromise tip and cantilever integrity.

The techniques described in literature include:

- Theoretical calculations based on cantilever size and material properties.
- Measurements of the gravitational deflection due to added masses.
- Measurements of the deflection due to cantilevers of known spring constant.
- Measurements of the deflection caused by the viscosity of the medium surrounding the cantilever.

The calculation of the k constant is necessary for each cantilever used in AFM experiments because the spring values indicated by manufacturer are often incorrect. Producers use large tolerances in the specified values of the cantilever force constant due to the difficulty in controlling the cantilever thickness at a particular stage of the manufacturing process and the structural defects and geometry deviations from cantilevers to cantilever. Because of this, several approaches have been developed to measure or calculate the cantilever spring constant. Perhaps the most accessible techniques are calibration against known references, the Sader method, and the thermal noise method. The first technique is really invasive, whereas the second and the third ones should be preferred, as they do not damage either the probe or the lever.

The most simple and elegant method reported in the literature involves a study of the cantilever fluctuation of thermal nature. Many authors modelled the cantilever as a simple harmonic oscillator with one degree of freedom (neglecting higher modes of oscillation). The thermal noise method appeals to the equipartition theorem, which states that the thermal energy present in all terms in the Hamiltonian of a system that are quadratically dependent on a generalized coordinate is equal to $k_bT/2$, where k_b is the Boltzmann's constant and T is the absolute temperature. If one can treat the cantilever as an ideal spring of constant k, a measurement of the thermal noise i.e., of the fluctuations $\left\langle x^2 \right\rangle$ around the equilibrium position allows the spring constant to be determined as

$$k = \frac{k_b T}{\left\langle x^2 \right\rangle}$$

Unfortunately, the cantilever cannot be treated as an ideal spring. A series of improvements, not discussed here,[72] leads to the correct calibration formula:

$$k = 0.8174 \frac{k_b T}{s^2 P} \left[\frac{1 - \left(\frac{3w}{2L} \right) \tan\phi}{1 - \left(\frac{2w}{L} \right) \tan\phi} \cos\phi \right]^2$$

where the numerical factor results from the geometry of the cantilever; s is the sensitivity calibration factor (in units of m/V); P is the noise power (in units of V^2) isolated in the fundamental resonant mode only; w is the width of the tip, and L is the cantilever length. Finally, the term in square brackets accounts for the cantilever tilt angle (ϕ) relative to the substrate and the geometry of the optical lever detection scheme commonly used in commercial AFM.

The most widely used method in our experiments belongs to the category of the geometric calculation of the elastic constant, improved by taking into account also the resonant frequency. This method, compared to the pure geometrical calculation, avoid to consider the thickness of the cantilever a factor that could induce relatively large deviations in the calculated value of the elastic constant. The mass of the cantilever is also required and this can be easily determined from the knowledge of the density and the dimensions of the cantilever. In particular for rectangular cantilevers:

$$k = m_e \rho_c whL\omega_{vac}^2 \qquad \text{Eq. 7}$$

that is the same as $\omega = \sqrt{\frac{k}{m}}$

where w, h, and L are the width, the thickness, and the length of the cantilever, respectively and ω_{vac} is the natural oscillating frequency in vacuum, ρ_c is the density of the cantilever, and m_e is the normalized effective mass, which takes the value of 0.2427. Although simple in appearance, application of the previous equation has been limited for several practical reasons that will be discussed in the following. In contrast to the plan view cantilever dimensions (the view from the top of the cantilever in which the length and the width of the cantilever are visible and hence are easily measured by optical techniques), thickness measurement typically requires the use of electron microscopy, which can be time consuming, can damage the sample, and cannot be carried out routinely on every cantilever. Furthermore, determination of the density or mass of the cantilever can pose an even greater difficulty. Typically, the reflectivity of AFM cantilevers is increased by the deposition of thin gold films on Si or Si_3N_4 substrate. This also necessitates the previous deposition of a thin sputter–coated chromium layer to improve adhesion of the gold layer. For most commercial cantilevers, the thickness of these individual layers is unknown, so that the average density of the cantilevers, and hence their mass, remain completely undetermined. Additionally, measurements of the frequency response of AFM cantilevers are commonly performed in air or in liquid medium. It is well known that the surrounding medium can markedly reduce the resonant frequency from its value in vacuum. It was found that the shift of cantilever resonant frequency from vacuum to fluids (gas or liquid) is strongly dependent on both the density and viscosity of the fluid and it can be accurately modelled. It will be now shown that these same results can be used to formulate a simple, practical, and accurate method for the determination of the spring constants of rectangular AFM cantilevers.

To begin with, it is worth noting that the shift in the resonant frequency from vacuum to fluid is primarily due to inertial effects in the fluid. The vacuum resonant frequency ω_{vac} is related to the resonant frequency in fluid ω_f by:

$$\omega_{vac} = \omega_f \sqrt{\left(1 + \frac{\pi \rho_f w}{4 \rho_c h} \Gamma_r \left(\omega_f\right)\right)} \qquad \text{Eq. 8}$$

On the other hand, the areal mass density over the surface of the cantilever ρ_c is given by:

$$\rho_c = \frac{\pi \rho_f w}{4h} \left[Q_f \Gamma_i(\omega_f) - \Gamma_r(\omega_f) \right] \qquad \text{Eq. 9}$$

where ρ_f is the density of the fluid, and Γ_r and Γ_I are the real and imaginary components of the hydrodynamic function $\mathbf{\Gamma}$, respectively. The function $\mathbf{\Gamma(\omega)}$ depends on the Reynolds number $Re=\rho_f \omega w^2/(4\eta)$ where η is the viscosity of the surrounding fluid, and is independent of the cantilever thickness (the most difficult parameter to measure) and density. Substituting Eq. 8 and Eq. 9 in Eq. 7 we obtain the required result:

$$k = 0.1906 \rho_f w^2 L Q_f \Gamma_i(\omega_f) \omega_f^2 \qquad \text{Eq. 10}$$

Eq. 10 relates the elastic constant k directly to the plan view dimensions of the cantilever, the fundamental frequency ω_f, and the quality factor Q_f in fluid. This expression is valid only if $Q_f >> 1$.

4.3.3. Calculation of the hardness

As previously stated, material hardness can be found by the following equation:

$$H = \frac{P_{\max}}{A_c}$$

Hence, in order to obtain a quantitative value of the hardness of the material under examination, we have to find the maximum load applied to the sample surface and the residual contact area left by the indenter over the surface once the load is removed.

If we consider the cantilever as an ideal spring with elastic constant k, according to Hooke's law, the load is defined as spring constant multiplied by the deflection of the end of the cantilever. Unfortunately, the instrument does not give a direct value of the displacement in length units. The signal recorded at the photodiode that monitors the cantilever deflection is a voltage, due to the photogenerated current. Indeed, we need a conversion factor that permits to calculate the bending movement of the cantilever in the real space and in length units. This factor can be easily found and, as already mentioned it is called sensitivity factor: basically it is defined as the cantilever deflection signal (voltage at the photodiode) versus the voltage applied to the z piezo determined from the slope of the force plot during indentation. The cantilever sensitivity can be calculated from a measure of loading over a very hard material such as alumina (Al_2O_3). This is possible because when the tip is in the contact zone and touching a stiff material, the piezo displacement equals the deflection of the cantilever because the tip cannot deform the sample (Fig. 53).

Accordingly, the cantilever displacement Δz can be evaluated as:

$$\Delta z = sensitivity[nm/V] \cdot displacement[V]$$

Once the elastic constant and the sensitivity factor are known, it is possible to determine the maximum force used in indentation and other mechanical experiments for the characterization of the examined specimens.

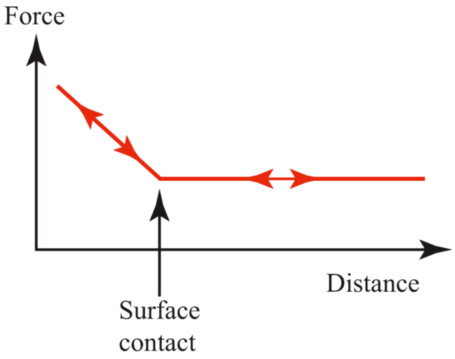

Fig. 53 – Typical force–distance curve recorded on a very stiff material: trace and retrace curves overlap in the contact region; the cantilever deflection equals the piezo displacement along the z *axis, thus enabling the calculation of the sensitivity constant.*

The investigated materials in the present PhD thesis are of different nature and rather heterogeneous. Hence, it was necessary to develop a reliable and repeatable method in order to compare their mechanical properties.

The triggered force method was first evaluated: the same maximum load was applied to different materials in order to compare their responses. Ignoring the ramp size, the AFM instrument should apply only the maximum set load. However, this method afforded strange results: sometimes, organic polymers resulted harder than silicon or steel. In order to check whether the system was working properly, a signal access module (SBOB, Fig. 54) was used to collect the data directly from the microscope, getting rid of signal conditioning and representation processing accomplished by the control software.

With this extension, it is possible to collect all electrical signals coming from the AFM head plus the high voltage used to actuate the piezoelectric scanner.

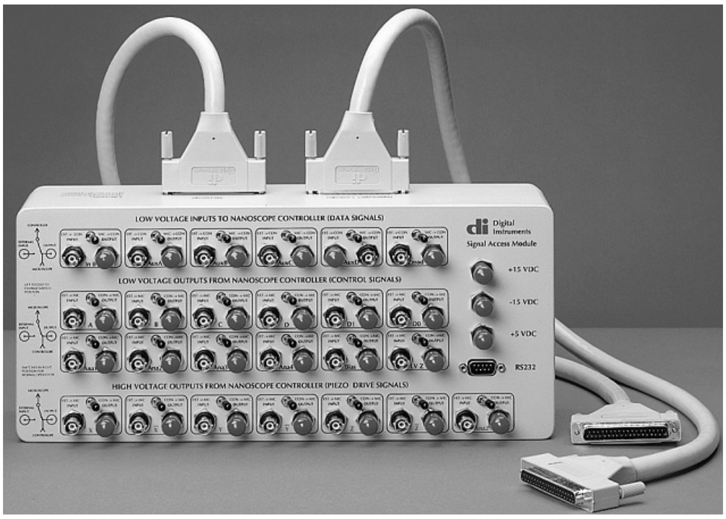

Fig. 54 SBOB signal access module

A digital oscilloscope (LeCroy 9384) was used to record the signals corresponding to piezo movement (high voltage in the z direction), deflection signal (in the z direction) as viewed at the photodiode, and the piezo correction in the x direction (Fig. 55).

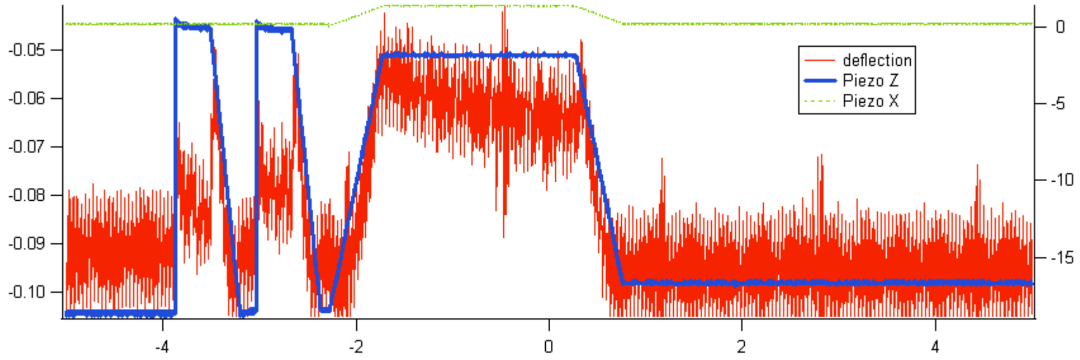

Fig. 55 – Signals recorded by the oscilloscope through the SBOB module: voltage applied to move the piezo in the z axis (blue), z deflection of the cantilever (red), and correction in the x direction while indenting (green).

The correction in the x direction is used because there is an angle between the cantilever and the surface. When the tip is kept into contact with the sample surface, this exerts a force in the x direction (Fig. 56).

This correction depends on the tilt angle and it has to be set properly because indentation experiments can give really different results (Fig. 57).

There is material deposition (pile–up) on the left, outboard side of each indentation depending upon the amount of correction. The pitching forward of the cantilever during nanoindentation tends to move the laser spot (reflected by the cantilever onto the position–sensitive detector) in a direction opposite to normal deflection. This produces a counter–effect that may lead to less deflection at the photodetector but higher forces. The end result is deeper, larger dents for lower *x rotate* values.

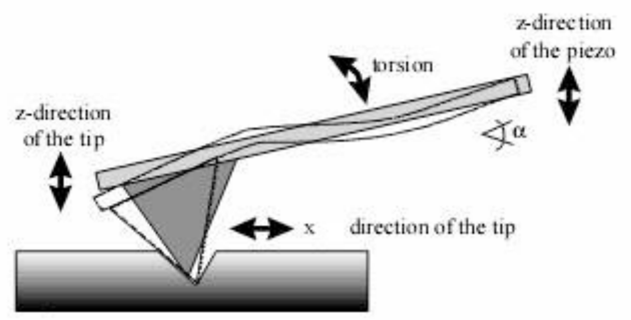

Fig. 56 – While approaching, the tip is tilted of an angle α. Once the probe starts to indent the surface it tends to pitch forward in the x direction. The system automatically rotates the sample with respect to the tip, by applying a small x translation, in order to avoid lateral forces (shear stress) over the surface.

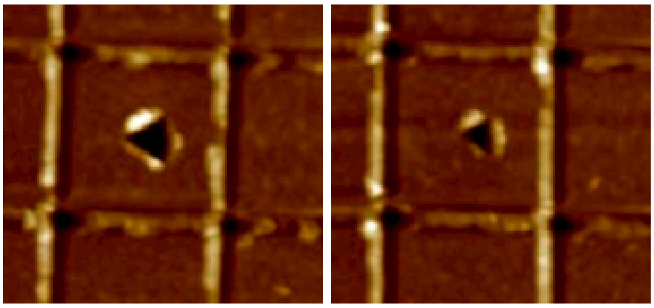

Fig. 57 – Influence of the tilt angle (left: 12.0 degrees; right: 20.0 degrees) on indentation experiments performed at the same maximum load. Note the pile–up effect on the left.

Coming back to the problem involved in triggered indentation, it is clear that two big spikes occur (Fig. 58) in the z displacement of the piezo at the beginning of the experiment. Very likely, the system requires those unwanted hits to calibrate itself and to find the value of the force needed for a triggered measure.

As expected, the system performs an indentation with the set maximum load, but it makes also two strong hits that alter the results and damage the sample before the programmed load–unload process. Therefore, nanoindentation experiments were performed using only a ramp size large enough to leave a mark in the sample surface and to compute hardness and other mechanical properties of the specimens, without using the triggered force method. By this approach, information must be derived directly from each force–distance curve recorded in nanohardness testing in order to get quantitative comparable data.

Different analysis techniques were developed for each segment of both elasticity and loading profiles. The loading portion requires models that include plasticity. The hold part is commonly used to investigate creep behaviour. The unloading section can be treated as the elastic recovery of the material. In practice, analysis of the loading and holding portions of the curve requires many assumptions about the relationship between plasticity and contact area. The most common analysis techniques make use of the unloading portion of the indentation data, primarily because they depend least from the model.

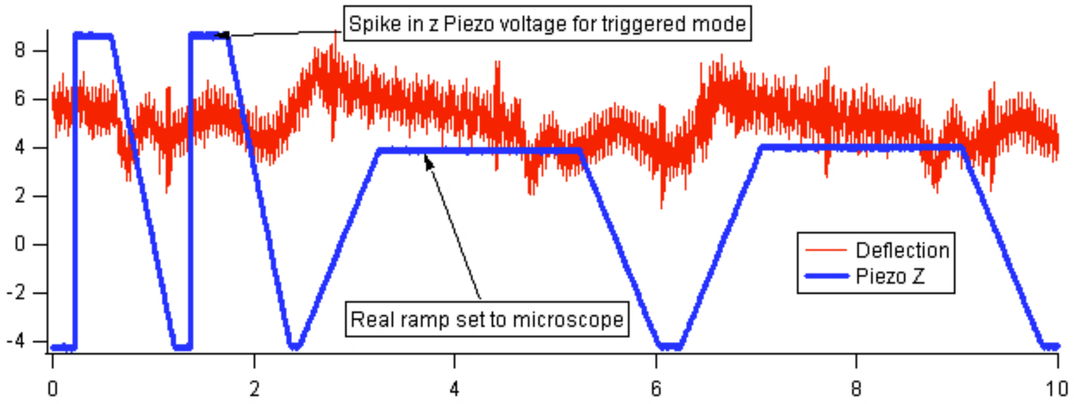

Fig. 58 –Signals recorded by the oscilloscope through the SBOB module: voltage applied to move the piezo in the z axis (blue), and z deflection of the cantilever (red). The two first spikes are needed by the software to calibrate the microscope and make the real indentation ramps at the desired P_{max} value.

Nanoindentation analysis is based upon the assumptions that the radius of curvature of the indenter is small compared to that of the specimen surface and that the dimensions of these objects are large compared to the contact area. By establishing that the size of the indent is small compared to the whole system, the stress and strain caused by indentation can be isolated from those of the specimen, such as attachment of the sample, surface constraints (boundaries), and geometry. It is also assumed that the contacting bodies are frictionless, that only the normal force is transmitted to the sample.

Over the years, several research groups investigated how best to interpret the load–displacement data that are collected during indentation testing. The investigation of the role of elasticity in material deformation began well before the reduction in component scale demanded a new testing method. In 1961, Stillwell and Tabor looked at elastic recovery of conical indentations and how they related to mechanical properties.[73] Armstrong and Robinson measured materials' combined elastic and plastic deformation during indentation testing in 1974.[74] But were Doerner and Nix[75] that first studied materials in the range of millinewton force where the indents become too small to be viewed by optical means. Later in early 90's, Oliver and Pharr slightly modified this technique.[76]

All these techniques start by examining the idealized elastic contact of a rigid sphere and a flat surface. In 1965, Sneddon[77] published the derivation of an expression for the contact between a rigid indenter of various geometries and an isotropic elastic half space. He defined the contact stiffness S as the increment of load P, divided by the incremental of displacement δh:

$$S = \left.\frac{\delta P}{\delta h}\right|_{elastic}$$

The stiffness hence could be calculated assuming that the first part of the unloading region is entirely elastic. Although most materials deform in both an elastic and plastic manner, most recovery upon unloading is thought to be elastic in nature. The residual deformation is the plastic response, related to the final depth h_f. The indenter is assumed to be completely rigid and crushproof so any elastic response is accounted in the reduced modulus E^*. The contact stiffness can be written as a function of the reduced modulus and the projected contact area A_c:

$$S = \frac{2}{\sqrt{\pi}} E^* \sqrt{A_c} \qquad \text{Eq. 11}$$

where E^* is the reduces modulus defined as:

$$\frac{1}{E^*} = \frac{\left(1 - \nu_s^2\right)}{E_s} + \frac{\left(1 - \nu_i^2\right)}{E_i}$$

E_s and E_i are respectively the Young modulus of the sample and the indenter. The relationship expressed in Eq. 11 is called the conical Sneddon stiffness equation. The area of contact is based upon the tip shape. Every tip has a well–defined area function dependent upon the depth of penetration. By this equation, the unloading slope is directly related to the modulus of the material and the square root of the area of contact.

Doerner and Nix were the first ones to establish a commonly used method for determining hardness and modulus from force displacement curves at the nanometre scale based on these principles. They assumed that the initial unloading was linear, and the intercept depth h_i was found by extrapolating the tangent from P_{max} to zero load (Fig. 59). Oliver and Pharr found that the initial unloading more closely resembled the behaviour of the power law, and not necessarily linear unloading.[76] They fitted the initial portion of the unloading curve with the relation:

$$P = \alpha h^m$$

where α and m are geometrical constants of indenters that can be found easily with a model of the tip and fitting the parameters with the curve. In order to make these calculations, a very accurate description of the tip's projected area of contact, as a function of depth, is necessary.

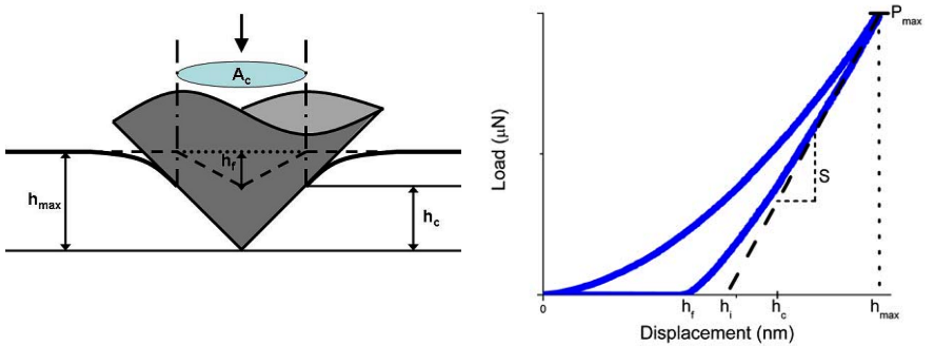

Fig. 59 – Representation of an indenter at maximum load (P_{max}) with h_{max} associated total depth. The indenter–surface contact at maximum load is defined by depth h_c with projected contact area A_c. The dashed line, with a final depth of h_f, indicates the sample profile after the load has been removed. The right plot represents the load–displacement curve, indicating the final (h_f), intercept (h_i), contact (h_c), and maximum depth. The stiffness (S) is the slope of the tangent (dashed line) at maximum load.

The experimental determination of the tip area function was determined first. The particulars of these measurements will be discussed later in this section. The projected contact area for each indent is the solution of the area function at $h = h_c$. By using the power law relationship for unloading and a well–defined function for the tip area, the hardness of the material can be defined as:

$$H = \frac{P_{\max}}{A_c}$$

where H is the hardness, P_{max} is the maximum indentation load, and A_c is the projected area of contact at depth h_c.

Among the material properties often sought in indentation testing, there is the modulus of the material. There is an accepted assumption in the calculation of the indentation modulus: that it remains constant over depth. The modulus can be calculated using the contact area and the stiffness:

$$E^* = \frac{\sqrt{\pi}}{2\sqrt{A_c}} S$$

With the knowledge of the tip reduced modulus, the Young's modulus (E^*) of the material under investigation can be derived. Table 1 reports the most common mechanical properties of the materials used for the fabrication of the tips.

To find the contact area, a function relating the contact area, A_c, to the contact depth, h_f, is needed. One method to find this relation is to reconstruct the entire shape of the tip using a particular calibration pattern. In general, topographical artefacts are a common problem while imaging with scanning probe microscopes. Anyway, in some cases this phenomenon that is present while scanning surfaces with features or irregularities comparable in size to the dimension of the working part of the tip can be helpful. If we consider a two dimensional model as represented in Fig. 60, the tip can be described by a $P(x)$ function, while the form of the true topography of the surface by a function $R(x)$. Then the AFM image of the surface $I(x)$ turns out as follow:

$$I(a) = R(x_k) - P(x_{k-a})$$

with the condition that $dR/dx = dP/dx$ in x_k points of contact.

Table 1: Mechanical properties of hard materials used for tip fabrication.

Material	Young's Modulus E (Kg/m^3)	Microhardness (GPa)	Poisson ratio ν	Density (GPa)
Diamond	900–1050	78–102	0.07	3.515
Si_3N_4	310	19	0.3	3.180
Si	130–188	9–10	0.3	2.330

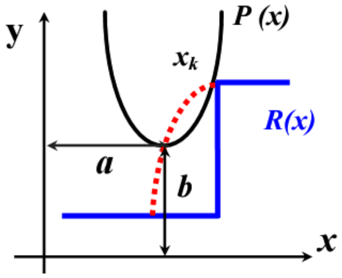

Fig. 60 – Schematic drawing of AFM acquisition process. The function that describes the tip, the function that describes the surface morphology, and the derived topography are represented in black, blue, and red, respectively.

Hence, if the surface consists of relatively high spikes with dimensions smaller that the tip, it is possible to reconstruct the tip shape. This method can be applied also in the three dimensional space (Fig. 61).

We can use a special calibration grating to obtain an AFM image of the tip used. Since the contribution of the real topography $R(x, y)$ is small compared to the dimensions of the probe $P(x, y)$, the image obtained contains information about shape, dimension, and defects (Fig. 62). This methodology requires a lot of time for acquiring the images, but it allows for a specific characterization of every tip used in nanoindentation experiments.

Another way adopted to find a relation between the indentation depth h_f and the contact area A_c is the so–called geometrical model.

Following the works done for commercial types of indenters such as Vickers, Berkovich, and so on, we have developed a model to get a relationship between the depth of indentation and the contact area. This model takes into account the dimensions and the shape of the tips microfabricated at the end of the commercial cantilevers used in our experiments.

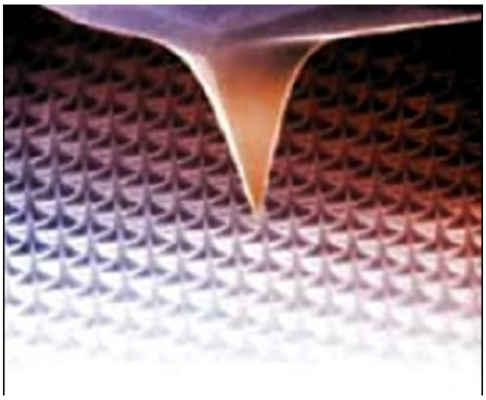

Fig. 61 – SEM image of the cantilever scanning over the pins test structure.

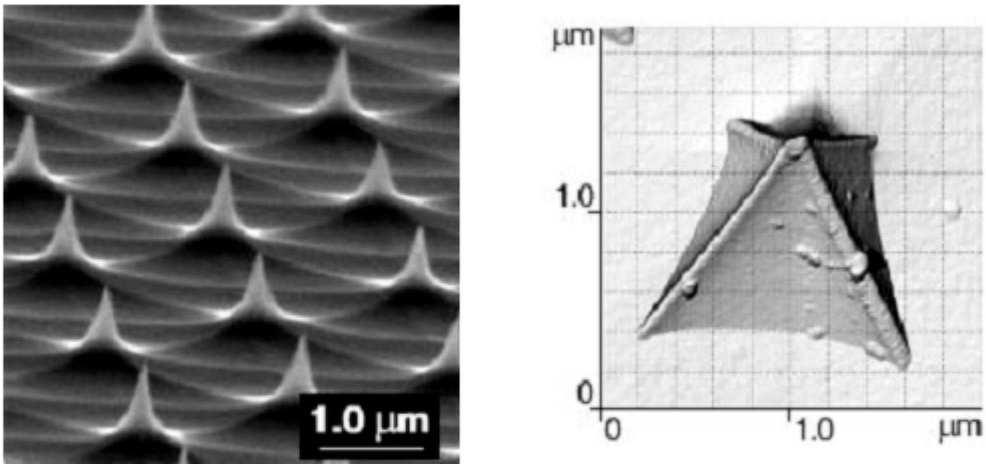

Fig. 62 – SEM image of the special pattern (left) used for the reconstruction of the tip shape (right).

Using simple geometrical relations and before starting nanoindentation experiments, a new expression was derived ($A_C = h_f^2 C_{tip}/2$) in order to take into account the morphology of the diamond–coated tip shown in Fig. 63.

By considering the geometrical characteristics of the tip, the C_{tip} coefficient can be easily calculated by equation:

$$C_{tip} = 2(\sqrt{A-2B} + \sqrt{C-2D})$$

where:

$$A = (1/\cos^2\alpha + 1/\cos^2\beta + 1/\mathrm{ctg}^2\alpha + 1/\mathrm{ctg}^2\beta),\ B = (1/\cos^4\alpha + 1/\cos^4\beta + 1/\mathrm{ctg}^2\alpha + 1/\mathrm{ctg}^2\beta),$$

$$C = (1/\cos^2\gamma + 1/\cos^2\beta + 1/\mathrm{ctg}^2\gamma + 1/\mathrm{ctg}^2\beta),\ D = (1/\cos^4\gamma + 1/\cos^4\beta + 1/\mathrm{ctg}^2\gamma + 1/\mathrm{ctg}^2\beta.$$

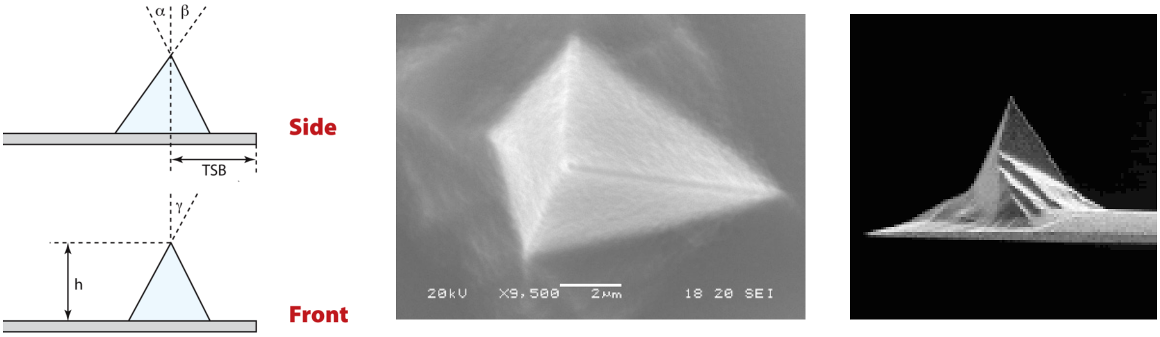

Fig. 63 – Geometrical characteristics and SEM images of the DDESP tip used in indentation tests.

The plot of the contact area versus the penetration depth is shown in Fig. 64.

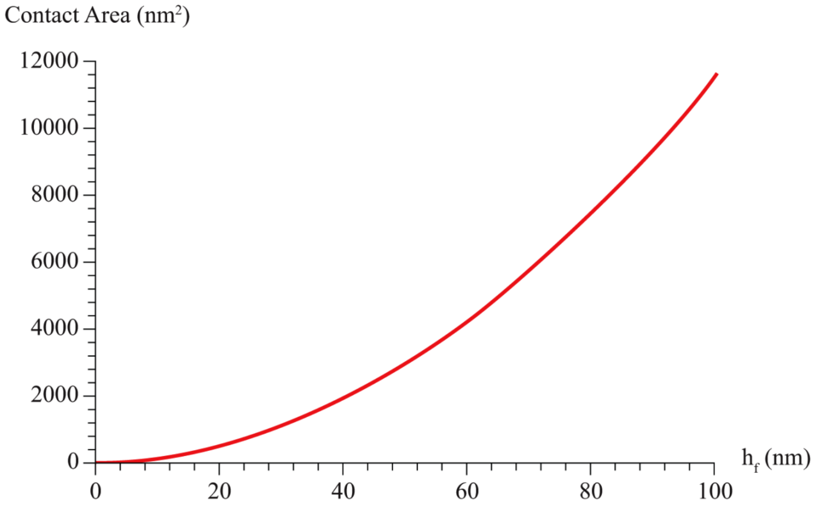

Fig. 64 – Plot of the dependence of contact area A_c on the penetration depth h_f for the DDESP diamond–coated tip.

Another theoretical model was used with success in order to calculate the hardness. In fact, it was shown that the conventional representation of hardness, in terms of maximum applied load divided by projected area is equivalent to the plastic work divided by the plastically deformed volume:[78]

$$\frac{load\ \ P(N)}{Plastic\ \ area\ \ A_p(m^2)} = \frac{Plastic\ \ work\ \ W_p(J)}{Plastic\ \ volume\ \ V_p(m^3)}$$

The work–of–indentation approach is developed and applied for hardness calculations in soft and hard materials, and also for a range of coated systems. The method appears to be less sensitive than other definitions to the effects of pile–up observed in soft materials. Work–of–indentation hardness is calculated directly from the energy of indentation without the need for estimating penetration depths, areas, or volumes, which can be time consuming and inaccurate. In particular, the plastic component of the work–of–indentation yields consistent results across the range of materials studied. The method breaks down, however, at very low loads and small penetration depths, which is likely to be due to deviations from the ideal tip geometry.

In nanoindentation experiments, the work of indentation can be calculated conveniently from loading–unloading curves (Fig. 65).

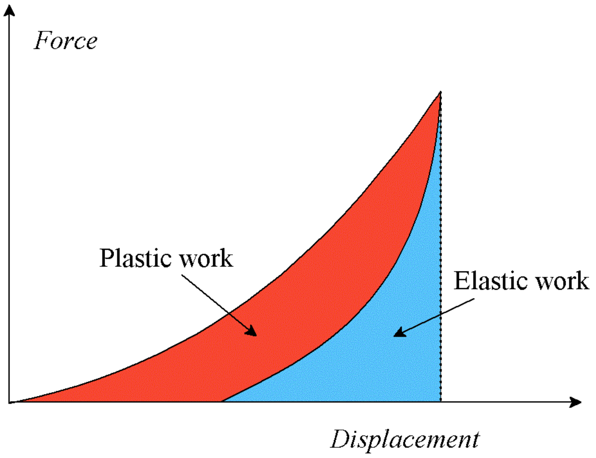

Fig. 65 – Typical plot obtained from nanoindentation experiments. The areas corresponding to elastic recovery and to plastic work are highlighted in blue and in red, respectively.

By using the work–of–indentation approach to hardness calculation, the errors due to pile–up are reduced, and a more accurate and consistent hardness variation with the applied load can be obtained. Moreover this method presents some advantages in the hardness calculation of composite or coated materials. In fact if creep or fracture occur, with this methodology is possible to remove the contribution of the fracture from the whole calculation of the plastic work (Fig. 66).

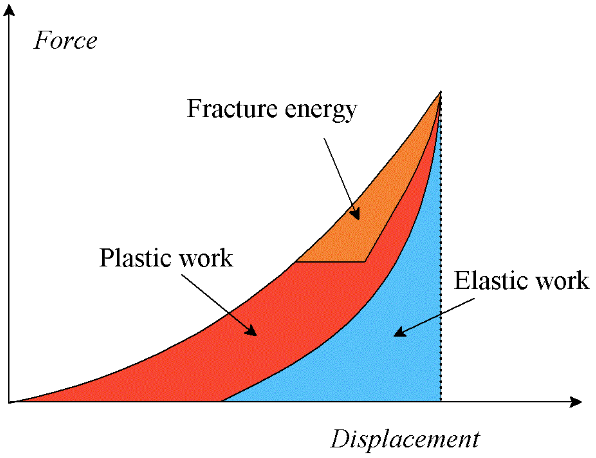

Fig. 66 – Typical plot obtained in an indentation experiment in which occurs the fracture of the material under investigation.

If the load is integrated with respect to the penetration depth, one finds:

$$W = \int P dh \qquad \text{Eq. 12}$$

where $W = W_e + W_p$. The conventional hardness is defined as:

$$H_p = \frac{C_{tip} P}{h_f^{\,2}} \qquad \text{Eq. 13}$$

where P is the load, h_f is the indentation depth, and C_{tip} is the geometrical constant calculated with our model. Eq. 13 can be rearranged to give the load in terms of hardness and displacement, and integrated to the maximum indentation depth. As a result, an approximate equation for work W is obtained in terms of hardness and maximum indentation depth h_f as follows:

$$W_p = \frac{H h_f^3}{3 C_{tip}} \qquad \text{Eq. 14}$$

If Eq. 13 and Eq. 14 are combined, and the indentation depth is eliminated, the hardness can be found to be proportional to the cube of the maximum applied load P_{max}, divided by the work squared:

$$H = \frac{C_{tip} P_{\max}^3}{9 W^2}$$

Hardness can now be calculated by using only the maximum load $P_{\max}$ and work W, whereas the maximum total indentation depth can be determined from the nanoindentation load–displacement traces. The knowledge of this parameter is particularly important when correlating micro– and nano–hardness data.

4.3.4. Nanoscratching tests

Before starting indentation experiments, the AFM system was preliminarily tested in nanoscratching mode. Both biological specimens and hard materials were investigated by this technique. In nanoscratching tests, the AFM tip is used as a plow to carve a pattern on the specimen surface. It would be really interesting to measure the resistance opposed by the material during the scratching in order to compare the resistance of their surface to wear and friction. However, nanoscratching tests can afford only qualitative data because the system does not allow for recording both the vertical and the lateral torsion of the cantilever while the tip is used as a plow. Nevertheless, other important information such as the dissipated power can be collected. Moreover, the tip can be used as single molecule nano manipulator and to check the adhesion of samples of interest to a surface.

Preliminary nanoscratching tests were carried out on Balinit C®, a very hard material used as steel protective film. Indeed, by taking into account this application field, nanoscratching experiments could be used to evaluate the force and/or the energy needed to pull the film off the steel surface. Since the morphology of Balinit C® rather coarse (RMS = 23.7), the indentation mark left over the surface is not easily detected (Fig. 67) in spite of the large applied force (2.3 μN). This seems to be due to morphological irregularities and to local defects. Moreover, the removed material during the scratch has to be accommodated somewhere on the surface.

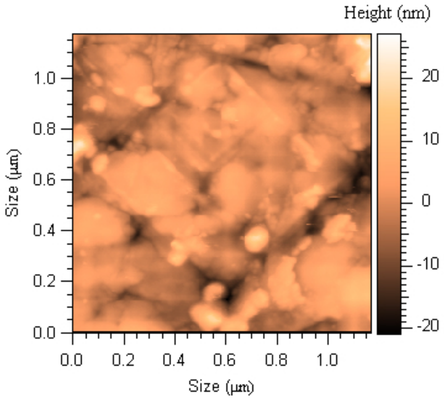

Fig. 67 – Rhomboidal scratching over Balinit C® surface.

Nanoscratching tests can be used also to check if biological molecules are covalently bound to reactive surfaces. This information can be really valuable, particularly in the fabrication of biosensors and to investigate the strength of protein–substrate and ligand–receptor interactions. To explore this AFM application, a scratch test was carried out on a fibrin fibril placed on top of functionalised silicon surface. Fig. 68 shows the horizontal scratch carved by the AFM tip on the silicon surface. It is clear that the scratch stopped at the filament, indicating that the tip could not detach and bend the protein strand. This behaviour demonstrates that the protein was strongly bound to the surface.

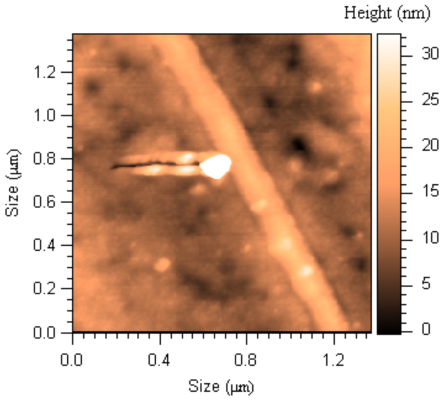

Fig. 68 – Topography after a nanoscratching test was performed over a fibrin filament.

4.3.5. Samples

Nanoindentation experiments were carried out on two commercially available organic polymers [polystyrene (PS) and poly(methyl methacrylate) (PMMA)], and on two hard materials [silicon and Balinit C®]. The organic polymers were studied in the form of thin films, obtained by spin coating of polymer solution on glass discs; the hard material samples were in the form of wafer and sheets (Fig. 69).

Balinit C® Silicon PS PMMA

Fig. 69 – Pictures of the samples used in mechanical nanoindentation analysis.

Balinit C® is an amorphous metal carbon coating (WC/C) that was developed at Balzers Gmbh as a special coating with high hardness and low friction coefficient. The multilamellar structure of the coating, in which tungsten carbide rich and carbon rich phases alternate in layers a few atoms thick, results in good running–in and burnishing with reduced sliding load. Balinit C® has good wear resistance, high load–bearing capacity even in dry or lubricant–starved contact, and low friction coefficient. In the specifications given by manufacturer, the hardness is reported equal to 7.7 GPa.[79]

Silicon is a tetravalent metalloid used in countless applications varying from electronic devices to the production of steels, cements, glasses, *etc*. In its elemental crystalline form, silicon has a grey colour and a metallic lustre, which increases with the size of the crystal. It is similar to glass in that it is rather strong, very brittle, and prone to chipping. It has 13 GPa hardness, 150 GPa Young's modulus, and 100 GPa bulk modulus.[80]

Poly(methyl methacrylate) (PMMA) is a thermoplastic polymeric material with 0.3–0.4 GPa hardness, 0.33 Poisson ratio, and 2.5–3.5 GPa Young's modulus,[80,81] sold under the trade name of Plexiglas, Perspex, or Lucite. It is used in a large variety of dental implants and in bone replacement. Polystyrene is a colourless, hard plastic with limited flexibility but it can be cast into moulds with fine detail.

4.3.6. Nanohardness measurements

Preliminary tests were carried out on silicon, polystyrene, poly(methyl methacrylate), and Balinit C®, in order to acquire some familiarity with the instrument. A series of loading–

unloading experiments were performed and both the force–distance curve and the topography after indentation were recorded to measure directly the residual contact area. Comparisons were made to analyse the differences between the direct method and the geometrical model of AFM tips developed for hardness calculation.

As already mentioned, traditional methods use the optical imaging technique; indeed, hardness evaluation requires the computation of the residual area of contact. Therefore, this method really provides only the plastic response of the material and is not very suitable for obtaining elastic and viscoelastic plastic properties of the materials. Also, for micro– and nano–hardness measurements, the errors involved in the contact area measurements may be quite large.

In our experiments, the ramps made with a diamond coated tip were used to calculate the force applied to the sample and hence the hardness and the Young's modulus.

The first experiments were carried out on polystyrene films by using a DDESP tip having k = 40.29 N/m and sensitivity 42.46 nm/V. The total ramp size used in indentation experiments was 1 micron; rate of approach was 200 nm/s. A $8.2 \cdot 10^{-6}$ N maximum force was achieved and a final indentation depth h_p = 75 nm was measured from force–distance curve (Fig. 70).

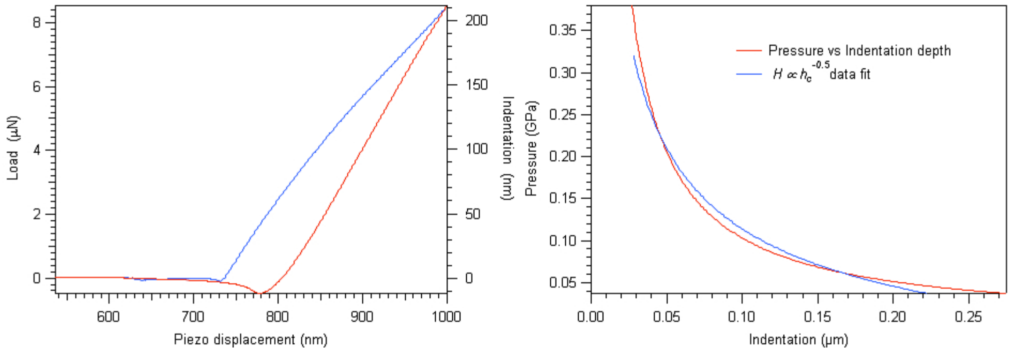

Fig. 70 – Force–distance curve acquired in polystyrene nanoindentation experiments (left) and indenter pressure vs. penetration depth.

The pressure–indentation depth function starts at about 0.5 GPa (not shown in Fig. 70) and tends to the asymptotic value of 0.04 GPa. The trace part of the indentation curve presents a hump, which is an indication of the pile–up process, as confirmed by the topography recorded after the indentation experiment (Fig. 71). Indeed, the AFM image captured after the indentation test, reveals a large expulsion of materials and only a small part of the mark left by the tip is still visible.

Balinit C® was the second specimen investigated in nanoindentation tests. Parameters used in indentation of Balinit C® are k = 50.1 N/m, sensitivity 34.88 nm/V, h_p = 8.3 nm as measured from the force–distance curve.

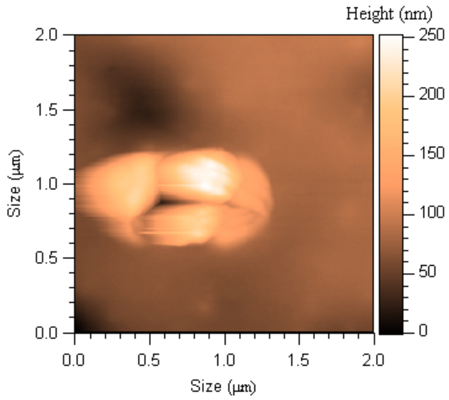

Fig. 71 – Indentation mark detected on polystyrene surface after the loading–unloading process.

The indentation curves of Balinit C® show a rather deep indentation and a little step appears during the retrace cycle, very likely due to tip adhesion on the surface. Moreover, the right plot of Fig. 72 show that the average pressure quickly decreases as the probe travels inside the surface. This could be attributed to a dislocation occurring at the beginning of indentation that requires a large load, followed by tip penetration with relatively low material resistance. The topography acquired after the experiment over the surface of Balinit C® shows an irregular shape of the indentation mark (Fig. 73).

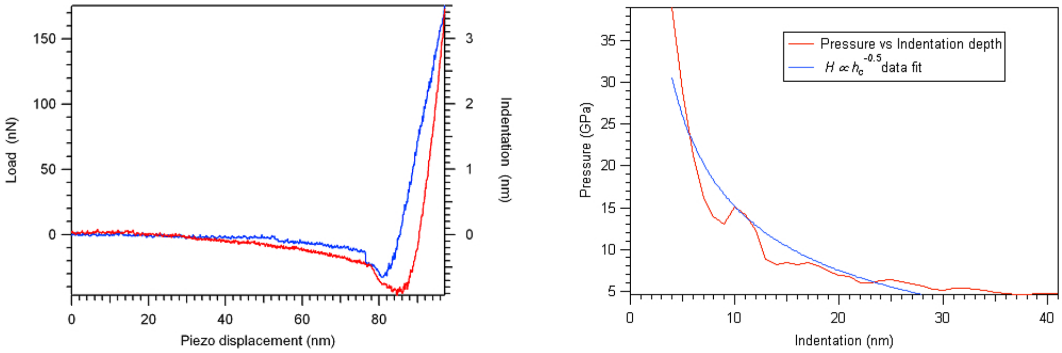

Fig. 72 – Force–distance curve (left) and indenter pressure vs. penetration depth (right) relevant to the nanoindentation of Balinit C®.

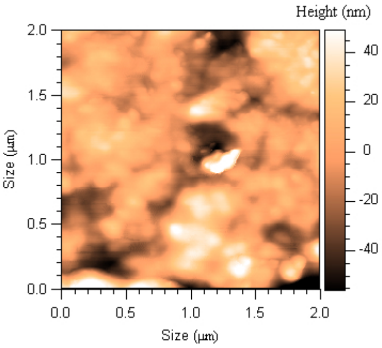

Fig. 73 – Topography of the indentation mark on Balinit C® showing debris at the border of the triangular pattern left the tip on the sample surface.

The hole left by the tip is not well defined, the edges are cloudy, and there is some debris especially on the bottom of the imprint.

Silicon was the last sample investigated in nanoindentation tests. Parameters used in the indentation of silicon are k = 40.75 N/m, sensitivity 36.93 nm/V. In this case, a double indentation test was performed. The results obtained in the first indentation experiment (Fig. 74) are similar to those of the second test (Fig. 75).

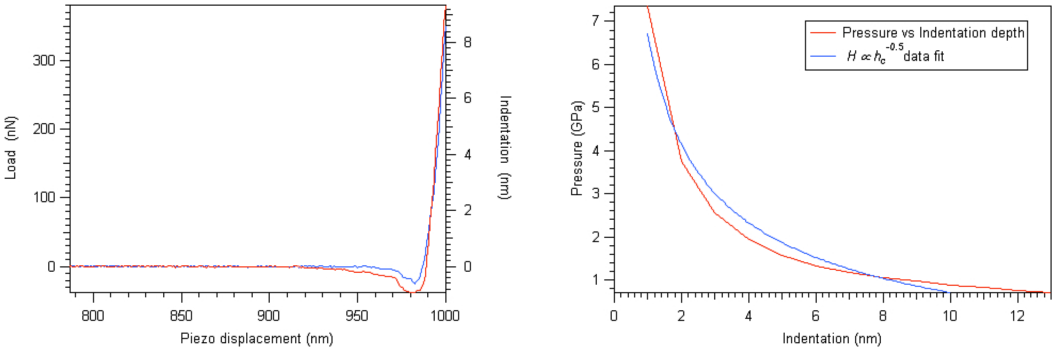

Fig. 74 – Force–distance curve (left) and indenter pressure vs. penetration depth (right) relevant to the first nanoindentation test on silicon.

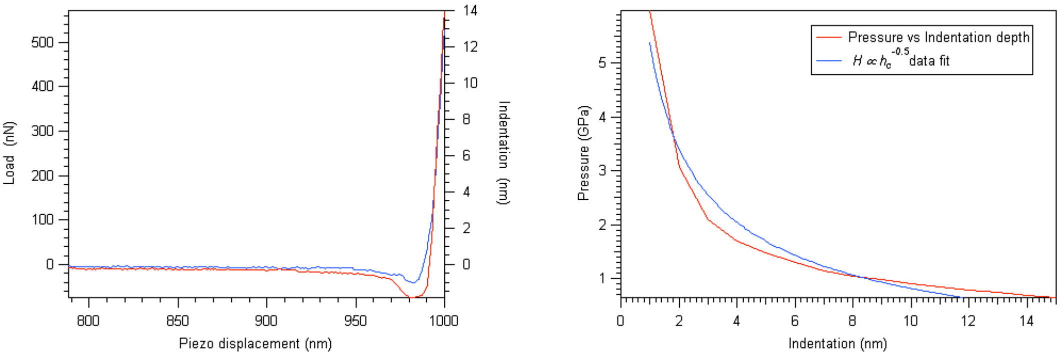

Fig. 75 – Force–distance curve (left) and indenter pressure vs. penetration depth (right) relevant to the first nanoindentation test on silicon.

The force and the ramps used in both experiments are the same and the images found after indentation present the same morphology. However, the plot of the pressure *vs.* the penetration depth highlights that the pressure calculated in the second test is definitely larger that that of the first experiment. This result indicates the occurrence of specific features related to the sample local microstructure that are accessible only by nanoindentation analyses. Fig. 76 presents the AFM topography of the silicon surface after the double indentation test. Two marks are clearly visible: on the left is present the imprint left by the first depth sensing indentation test, while the second mark is on the right. At a closer look, the latter imprint (at the image right side) appears to have more pronounced borders than the first one.

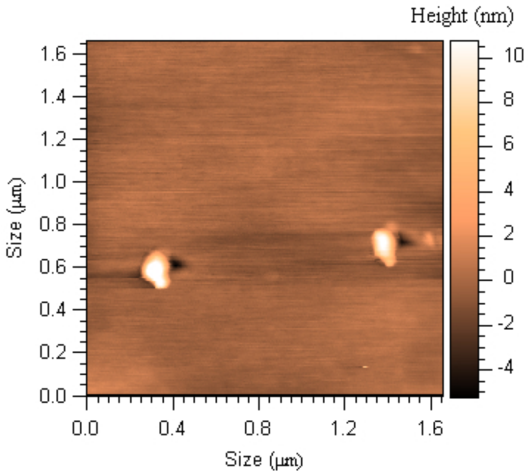

Fig. 76 – Indentation marks left on silicon by the double indentation test.

The results collected in preliminary tests are summarized in Table 2. In order to compare the results obtained by our geometrical method with a more traditional optical technique, we developed a procedure able to obtain the residual contact area after indentation. This method consists in fitting a plane to the AFM topography (§ 2.4.1.1) and then measuring the whole area below the fitted plane.

Table 2. Experimental and literature data relevant to the hardness of the investigated materials.

Material	Hardness (GPa)	
	Experimental	Literature
Polystyrene	1.6	~ 0.3
Silicon	10.6	~ 13
Balinit C®	6.7	7.7
PMMA	0.1	~ 0.3

As an example, Fig. 77 reports the topography collected in a preliminary test carried out on poly(methyl methacrylate), a polymer with well–known mechanical characteristics.

The area of indentation was zoomed in, a plane was fitted to the resulting image, and residual indentation area was detected and measured (Fig. 78).

To apply the model of direct area measurement instead of the DSI model, the topographic image must be processed in order to calculate the residual contact area A_c from the AFM map. This is obtained by fitting the original image with a plane and then by searching all points that have coordinates below the fitted plane. In such a way we can easily calculate the contact area and hence the hardness for each specimen. The images obtained by this procedure from the topographic maps in Figs. 71, 73, and 76 are shown in Fig. 79.

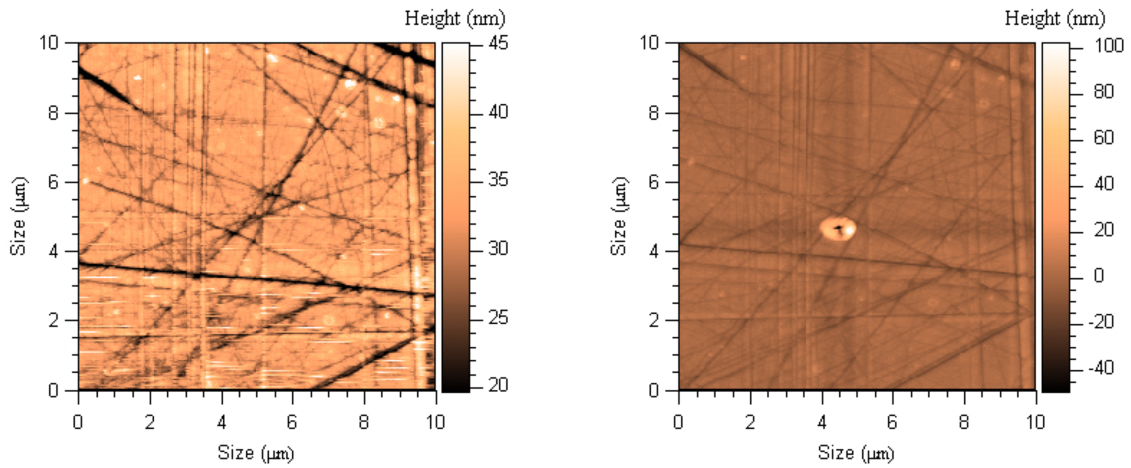

Fig. 77 – Topography of PMMA before (left) ad after (right) the indentation experiment.

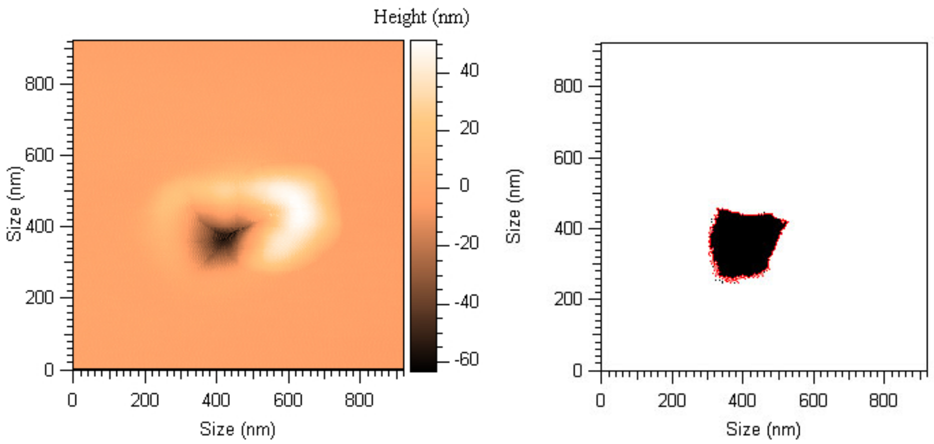

Fig. 78 –AFM topography of the imprint left by nanoindentation on PMMA surface (left) and residual contact area (right).

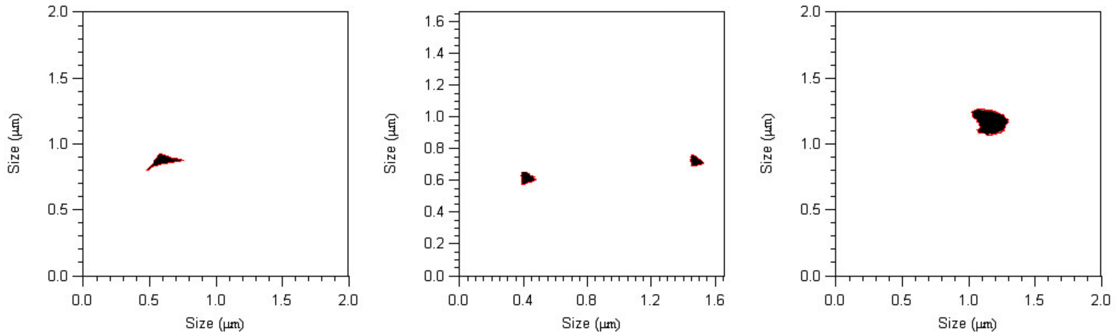

Fig. 79 – AFM maps highlighting the residual contact areas present on polystyrene (left), silicon (centre), and Balinit C® (right) after nanoindentation at different loads.

The residual contact area of softer materials such as polystyrene and poly(methyl methacrylate had a more defined shape. Nevertheless, the shape has very clear hedges also in the case of silicon. Indeed, the silicon flat surface allows for an easy identification of both marks that resemble the tip shape.

The most difficult identification process was found in the case of Balinit C® topography. In fact, the indent mark did not present the expected rhomboidal tip shape: the original contour is jagged due to dislocation and material expulsion during indentation, probably enhanced by the relatively large load used in the measurement. Those defects increase the already intrinsic difficulty in the measurements of the residual contact area that permits the hardness calculation as demonstrated by the reported results in the Table 3.

Table 3 – Hardness of different materials evaluated by direct A_C measurements.

Material	Hardness (GPa)	
	Experimental	Literature
Polystyrene	0.6	~ 0.3
Balinit C®	0.6	7.7
Silicon	1.6	~ 13

The reported values are far from the corresponding literature data and this result can be attributed to surface modifications that occur during the tip movement within the sample. Indeed, these effects have been detected for both polystyrene (adhesion and relatively large pile–up affect) and Balinit C® (dislocations and debris formation).

Nevertheless, better results can be obtained by a more accurate calibration procedure, by the use of relatively small loads, and for the most part, by exploitation of the close loop in the z–direction piezo scanner (Fig. 80 and Fig. 81). Accordingly, the hardness determination by the direct area method was carried out on PMMA and gold with a dedicated system (Picoforce, Veeco). However, this technique afforded nano–hardness values about one third of the macro hardness data reported in literature (Table 4).

Table 4. Direct A_C measurement of material hardness by a dedicated system.

Material	Hardness (GPa)	
	Experimental	Literature
PMMA	0.12	~ 0.3
Gold	0.4	~ 1.4

4.3.7. Dependence of hardness on the penetration depth

Once set–up the methods for determining material nanohardness, we performed an extensive investigation to assess the dependence of hardness and Young's modulus on the indentation depth. When the tip is pushed inside the sample, a whole range of complex phenomena occurs including adhesion and material displacement; hence, the results are of difficult interpretation. Nevertheless, it would be of great interest to assess the mechanical characteristics not only of the surface but also of inner structures present within the investigated specimens. For instance, protective coatings and surface structures present on tissue engineering scaffolds and other biomedical devices can be studied in details.

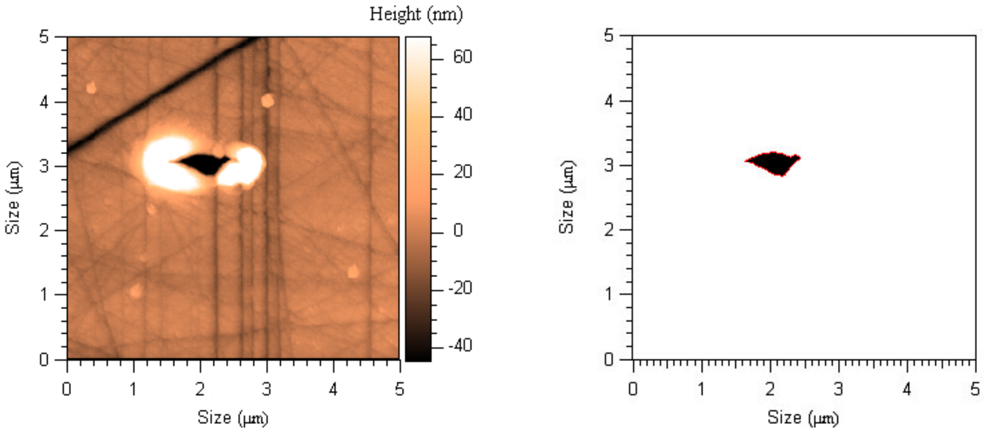

Fig. 80 – AFM topography (left) of the imprint produced on PMMA surface by nanoindentation and residual contact area (right) using the system provided with z closed–loop piezo scanner.

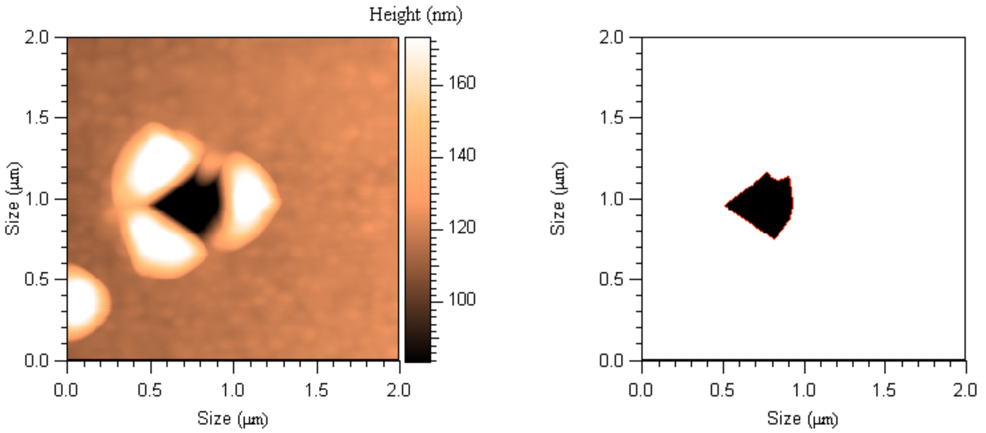

Fig. 81 – AFM topography (left) of the imprint produced on gold surface by nanoindentation and residual contact area (right) using the system provided with z closed–loop piezo scanner.

Hardness data evaluated for polystyrene and poly(methyl methacrylate) at various indentation depths are presented in Fig. 82 and Fig. 83, respectively. The corresponding Young's modulus curves are reported in Figs. 84 and 85. About 50–100 indentation tests were performed on each material at different indentation depths in order to collect enough data to perform statistically significant analysis of the influence of the penetration of the tip inside the sample on mechanical properties. It is clear that both hardness and modulus decrease by a power law ($H \propto h_c^{-0.5}$) on increasing the indentation depth (h_c). This behaviour is in agreement with what is reported in the literature,[82] although no sound explanation has been provided yet. Apparently, polystyrene and poly(methyl methacrylate) have close hardness and Young's modulus. However, this resemblance is only indicative of a comparable order of magnitude because of the different penetration depths. These data are in good agreement with what reported in the literature.

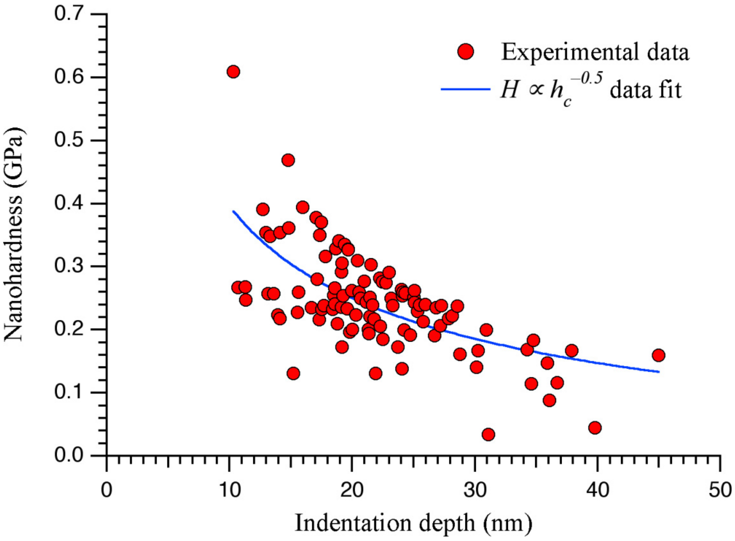

Fig. 82 – Polystyrene nanohardness data obtained in a series of experiments carried out by varying the indentation depth.

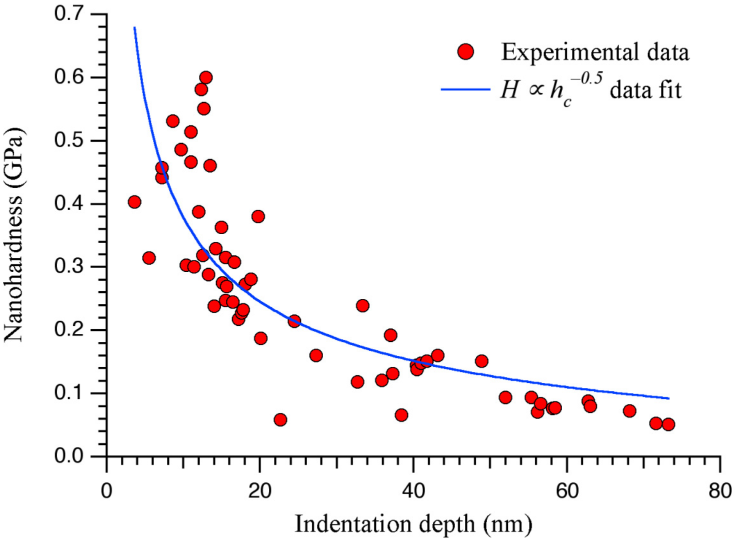

Fig. 83 – Poly(methyl methacrylate) nanohardness data obtained in a series of experiments carried out by varying the indentation depth.

The observed data scattering is typical of the performed mechanical analysis. The main factor that affects these measurements is the plasticity of the examined material. The plasticity is the property of a material to undergo non–reversible shape changes in response to the applied force. Plastic deformation occurs under shear stress while fractures occur under normal stress. Each measure was performed at different depth and in different points of the specimen surface with the consequence that each value is affected by a different local gradient of the plasticity.

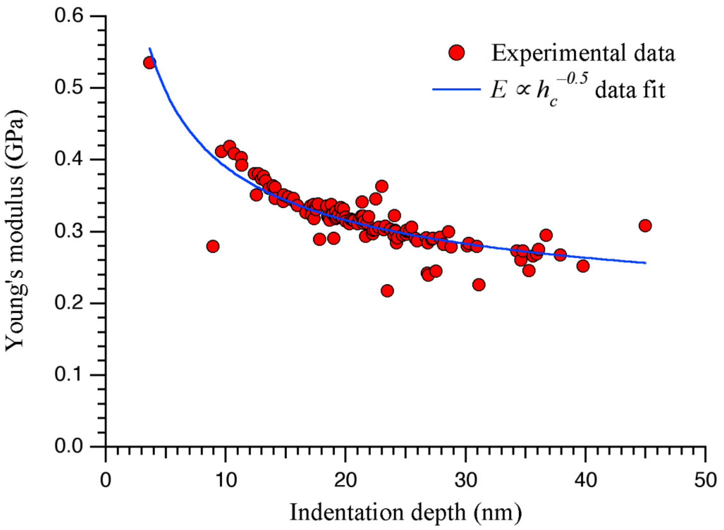

Fig. 84 – Polystyrene Young's modulus data obtained in a series of experiments carried out by varying the indentation depth.

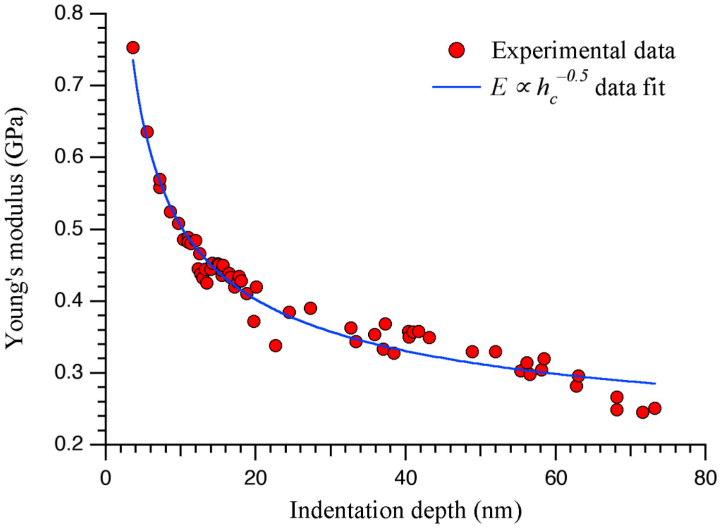

Fig. 85 – Poly(methyl methacrylate) Young's modulus data obtained in a series of experiments carried out by varying the indentation depth.

We believe that the theory of plasticity should be based not only on the stress–strain behaviour obtained from macroscopic mechanical tests, but should also draw information from nanomechanical gradient–dominant experiments, such as nanoindentation tests. In those experiments when a tip is moved inside the sample, the removed material has to be accommodated. The material displacement during indentation takes advantage of defects, as dislocations in ductile crystals, micro–and nano cracks in very brittle matter (quasi crystals, for instance grain boundaries), or free volumes (e.g. holes and pores in glasses or polymers).

4.4. PROTEIN SWELLING

The design of biocompatible synthetic surfaces is an important issue in the field of material medical applications. The discovery of chemical force microscopy (CFM) and its modification for the optical detection of exceedingly small forces has opened the exciting perspective of imaging the surface of living biological specimens. The additional potential of CFM for the study of molecular recognition, by using a measuring tip with bound ligands, has recently gained much attention. The idea is to detect and study the binding of ligands on tips to surface–bound receptors by applying an increasing force to the complex that reduces its lifetime until it dissociates at a measurable unbinding force.

Molecular interactions are of key importance for the function of the immune system. Suitably functionalized tips can be used for investigating the strength of protein–substrate and ligand–receptor interactions. These measurements can also give an insight on the activity of antibodies bound to different surfaces. Single–molecule force spectroscopy and binding force measurements by AFM show a growing potential for functional investigations of biomolecules and for the mechanical manipulation of single molecules. The technique has revealed unique details of the molecular basis of the mechanical properties of biological molecules and polymers that could not be obtained otherwise and we expect more to come. The investigation of intermolecular forces can improve also our understanding of microscopic phenomena, such as adhesion, friction, lubrication, and so on. Several detective techniques such as surface force apparatus, optical tweezers, and interfacial force microscope were used to measure intermolecular forces. While these techniques can be applied to investigate intermolecular interactions, many of them lack either the spatial or the force resolution necessary to measure discrete molecule–molecule interactions. Compared to the above instruments, the chemical force microscopy, which exploits chemically functionalized tips to study intermolecular or chemical groups interactions at nanometre scale, is a promising and efficient tool for detecting forces between molecule pairs or single chemical bonds.

4.4.1. Self–assembly monolayers

Surface modification techniques provide good approaches to control the interactions between living systems and implanted materials by modifying the surface characteristics. Self–assembly monolayers (SAM) are surfaces consisting of a single layer of molecules, typically ordered at the molecular level, on a substrate. Rather than having to use a technique such as chemical vapour deposition or molecular beam epitaxy to add molecules to a surface (often with poor control over the thickness of the molecular layer), self–assembled monolayers can be prepared simply by adding a solution of the desired molecule onto the substrate surface and washing off the excess. Alkylthiols on gold are a typical example. Sulphur has particular affinity for gold, with binding energy in the range of 20–35 kcal/mol (85–145 kJ/mol). Alkanes with a thiol head groups will stick to the gold surface and form an ordered assembly with the alkyl chains packing together due to van der Waals forces. For alkylthiols on gold, the extended alkyl chains typically orient with an angle of about 30 degrees from the perpendicular to the substrate, and are assumed to be in a fully extended linear arrangement (Fig. 86).

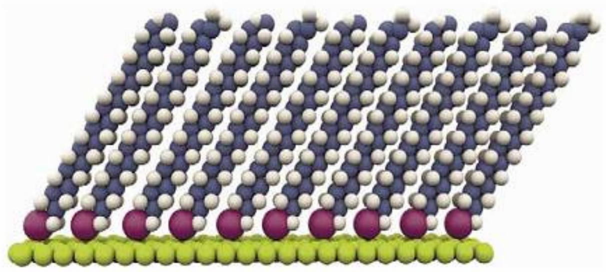

Fig. 86 – Schematic representation of alkylthiol SAM on a gold surface.

The initial stage of SAM formation usually takes minutes or less under the normal conditions of 0.1–10 mM thiol concentration in a solvent. A more complete ordering of the assembly can take place over days or months, depending on the molecules involved. Alkylthiols are known to assemble on many metals, including silver, copper, palladium, and platinum

A variety of other self–assembled monolayers can be formed, although there is always debate about the degree to which systems self–assemble. Alkoxysilanes are another well–known example of self–assembly on silicon oxide surfaces and potentially are of greater technical relevance than alkylthiol assembly on metals. A trialkoxyalkylsilane was used in our experiments even if the layer growth requires a careful preparation in order to avoid the reaction of siloxane bonds with water or humidity to form dimers and other aggregates and hence giving rise to the formation of irregular multilayers.

4.4.2. Investigation of protein unfolding

The aim of the present research was to study the unfolding of proteins. Investigation of the interactions of human serum albumin (HSA) linked to a silicon tip with a silicon surface functionalized with a reactive self–assembly monolayer represented a good starting point for biocompatibility experiments. Indeed, HSA is a very important protein. It is the most abundant protein in human blood plasma and it is involved in the regulation of osmotic pressure of the blood flow. It is produced in the liver and it is necessary for the correct distribution of body liquids into intervascular compartments and in tissues. The reference range for albumin concentration in blood is 30 to 50 g/l. The albumin molecule is negatively charged and for this reason its adhesion over the flat surface of mica, which is also negatively charged, is unfavourable. Accordingly, HSA attachment was performed using a SAM substrate as linker between the protein and the surface.

4.4.2.1. Surface functionalisation

The surfaces of AFM tips and of silicon wafers were functionalized with aminopropyl-triethoxysilane (APTES) in order to form a reactive self–assembly monolayer that could covalently bind proteins through the free amino groups.

The preparation and functionalisation of long–term stable protein–coated AFM tips is an important issue in force spectroscopy. In particular, in the context of conformation change experiments it is a desirable goal to reach long–term stability because it provides the opportunity to measure a long series of force curves with the same set of molecules under diverse experimental conditions. But ageing and wearing of the silane layer were frequently found to limit the use of such tips in long term measurements. For this reason, tips were used immediately after the functionalization.

Functionalization was performed in five steps: degreasing, surface hydrolysis, drying, APTES treatment, and HSA binding. The silicon specimens were first treated with piranha solution (3/1 v/v sulphuric acid and hydrogen peroxide) in order to remove organic contaminants and start activating the surface. They were further degreased by successive washings with boiling dichloromethane, boiling methanol, and boiling acetone. The samples were then extensively rinsed into pure water. Since the presence of hydroxyl groups onto the silicon surface is crucial for the reaction with APTES on silicon, the samples were treated with bidistilled boiling water for at least 2 hours and then heated in a furnace at 200 °C in order to remove the residual moisture. Surface activation was performed by maintaining the silicon wafer and tips into 1.2 mM APTES solution in anhydrous toluene. Anhydrous toluene was prepared by distillation over a Na/K alloy under nitrogen atmosphere. Immediately before use, a small amount of APTES was added to the distilled toluene in order to react with residual water that could be still present, and precipitate as a flocculent suspension that can be easily removed. The last step involved the reaction of APTES–modified surfaces with the protein. This was achieved by maintaining the silicon surface into $2.3 \cdot 10^{-5}$ M HSA aqueous solution. The same functionalization procedure was applied also to silicon nitride tips.

4.4.2.2. Characterization of silicon surface by contact angle measurements

The formation of a stable and ordered organic layer is crucial for the attainment of well–defined nanostructures. The quality of stable monolayers can be estimated from wetting measurements. Indeed, the shape of a liquid droplet on a plane homogeneous surface depends on the free energy of both the droplet and the surface (Fig. 87).

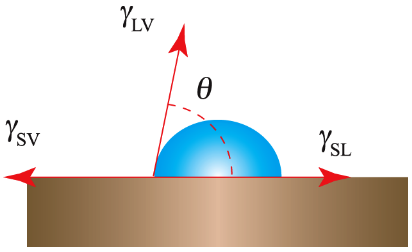

Fig. 87 – Schematic representation of the forces acting on a water droplet placed on top of a plane surface.

The contact angle is related to the surface free energy by the Young's equation:

$$\gamma_{LV} \cos\theta = \gamma_{SV} - \gamma_{SL}$$

where γ_{LV}, γ_{SV} and γ_{SL} are the interfacial tensions at the liquid–vapour, solid–vapour and solid–liquid interface respectively. The angle of a droplet on a solid surface is the result of the balance between the cohesive forces in the liquid and the adhesive forces between the solid and the liquid. If there is no interaction between the solid and the liquid, the contact angle will be 180°. As the interaction between the solid and the liquid increases, the liquid spreads until $\theta = 0°$.

Contact angle measurements were performed with a home–made microscope equipped with a digital camera. The system, able to reach a maximum magnification of 243x was used to acquire images of water droplets on the investigated surface. The digital images were then processed with ImageJ, a public domain, Java image–processing program developed at the National Institutes of Health (USA).

The activation of the silicon surface was first checked by comparing the wettability of the degreased silicon wafer and that of the corresponding hydroxylated wafers (Fig. 88).

The picture quality is not good enough for quantitative measurements. However, image processing by ImageJ to find the droplet contour (Fig. 89) made evaluation of the contact angles much easier.

The contact angles of water droplets on degreased silicon and silicon treated with piranha solution and boiling water were 52 and 22°, respectively. These data indicated that the activated silicon was much more hydrophilic than the starting sample because of the presence of hydroxyl groups on its surface. On the other hand, hydroxylated silicon ($\theta = 22°$) and APTES–functionalized silicon ($\theta = 16°$) showed similar water wettability (Fig. 89), very likely due to the presence of free hydroxyl and amino groups, respectively.


Pure Silicon Hydroxylated silicon

Fig. 88 – Optical microscope images of distilled water droplets on pure silicon (left) and on hydroxylated silicon (right).

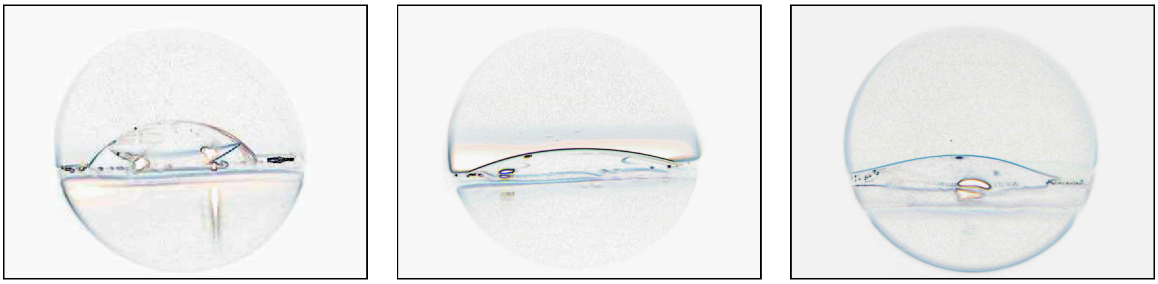
Pure Silicon Hydroxylated silicon APTES functionalized silicon

Fig. 89 – Images of distilled water droplets on degreased silicon (left), on hydroxylated silicon (centre), and on APTES–treated silicon (right) processed with ImageJ software.

4.4.2.3. Characterization of silicon surface by force–distance AFM measurements

In order to highlight the differences between hydroxylated and APTES–treated silicon surface, the samples were analyzed by AFM in the force–distance mode.

As already mentioned, a force–distance curve is a plot of tip–sample interaction forces *vs.* tip–sample distance. In general, this kind of curve results from two contributions: the elastically potential of the cantilever and the interaction potential between the tip and the surface of sample. The latter contribution is crucial for the understanding of SAM–functionalized surface properties. In fact, the tip feels a particular interaction when it is in contact with SAM molecules. The force–distance curve presents two regions after the jump to contact (Fig. 90). The first one, characterized by low stiffness, is due to the presence of the SAM over the surface (~8.15 N/m). Then the stiffness quickly rises to ~17.2 N/m when the tip is brought in contact with the surface as the load is increased. This behaviour differs from the loading curve obtained on the starting silicon wafer (Fig. 91). Moreover, the depth of the zone of low stiffness (1.8 nm) is in good agreement to the length of the APTES molecule. These results confirmed the efficacy of the silanisation process.

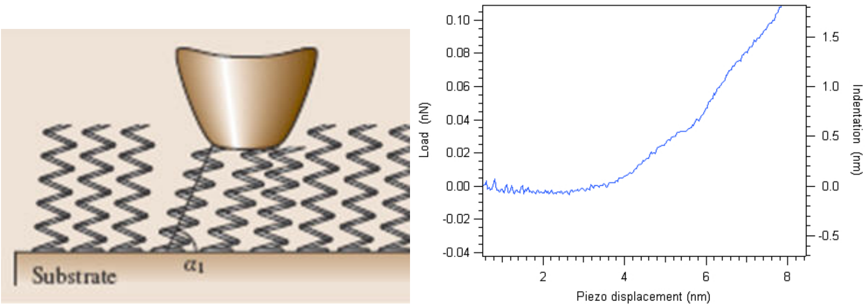

Fig. 90 – Schematic representation of tip–SAM interactions (left) and force–distance curve (right) recorded during tip approach to APTES–modified silicon surface.

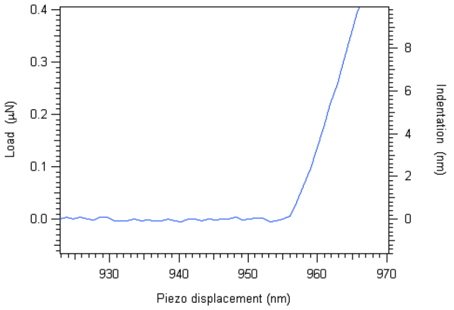

Fig. 91 – Force–distance curve recorded during tip approach to silicon surface.

4.4.2.4. Characterization of silicon surface by high–resolution AFM images

The formation of the APTES surface layer was better investigated by acquiring AFM high–resolution images recorded with the deflection channel. These images are quite different from the more usual height images. For instance, topography is recorded as the difference between the set up value and the piezo correction during the scan. On the contrary, deflection is the original signal that is gathered from the photodiode. In other words, instead of using the constant gap mode of operation, maps were acquired at constant height, that is possible due to flatness of the specimens in the small investigated region. In such conditions, resolution may be improved due to the absence of the feedback loop. High–resolution analysis of silicon surface was performed by acquiring lines at a rate of 30 Hz. Image size was only 10x10 nm.

High–resolution surface images of pure silicon (Fig. 92) and of APTES–activated silicon (Fig. 93) presented two different patterns. This difference is better evidenced by the corresponding bidimensional Fourier transforms (2D FFT), a technique usually adopted to point out the regular features in microscope images. In fact, the presence of a molecular layer on top the surface modifies the regularity of the crystallographic pattern, thus giving rise to other structured shapes.

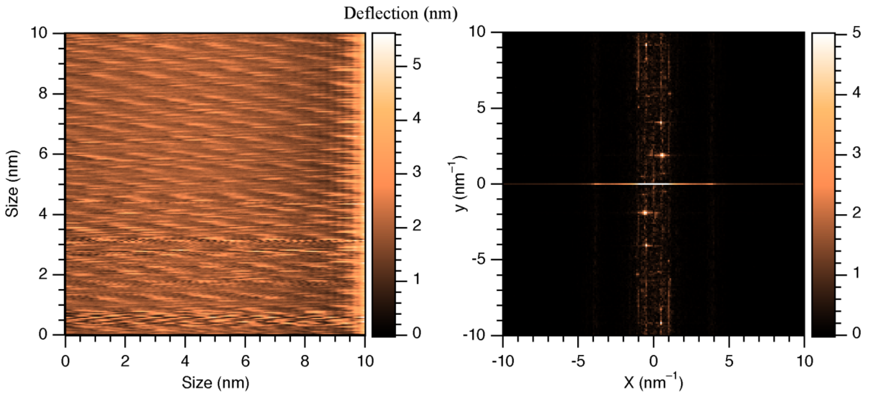

Fig. 92 – Deflection map of silicon 100 surface (left) and the corresponding 2D FFT (right).

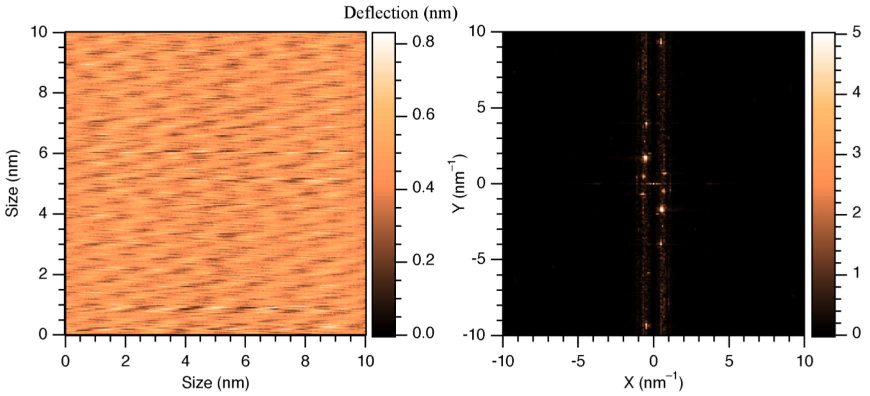

Fig. 93 – Deflection map of APTES–functionalised silicon 100 surface (left) and the corresponding 2D FFT (right).

This analysis assured that the desired functionalization was achieved. Moreover, high–resolution images demonstrated that the molecular layer formed on the silicon surface is not regularly assembled as sketched to the right of Fig. 94, but it is more alike the irregular structures on the left.

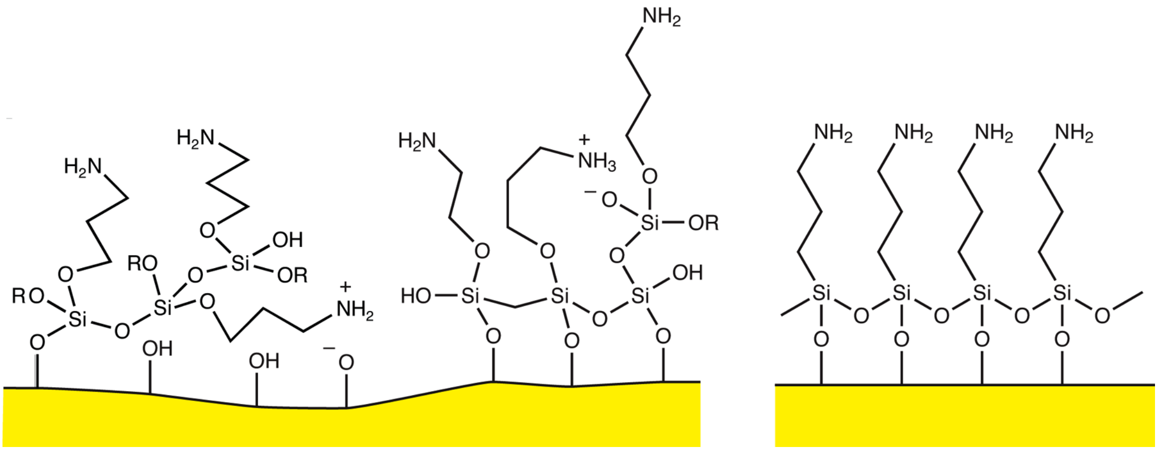

Fig. 94 – Schematic representations of SAM assembly: realistic irregular structure (left) and ideal arrangement (right).

Verification of the effective APTES functionalization of AFM tips was almost impossible. Nevertheless, after APTES treatment, the tips were kept in HSA water solution for about a 24 h. To check the presence of bound protein on the probe tip, a fluorescence test can be performed. In particular, irradiation at 320 nm can be used to excite fluorescence emission by the protein that under excitation has a yellow–green emission, as shown in Fig. 95.

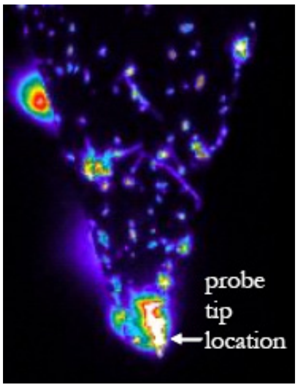

Fig. 95 – Fluorescence image of the HSA functionalized tip.

4.4.2.5. Protein unfolding measurements

In the force–measuring mode of the AFM, single molecules or pairs of interacting molecules are stretched between the tip and a flat substrate whose position is continuously monitored. The force resolution of the AFM is limited by the thermal noise of the cantilever that is determined by its spring constant. According to the equipartition theorem, the cantilever has on average a thermal energy of $0.5K_bT$ and therefore $0.5k\Delta z^2=0.5K_bT$ where K_b is the Boltzmann's constant and T the absolute temperature. Since $F= k\Delta z$, the force sensitivity is given by $\Delta F = (K_bTk)^{1/2}$ and is, therefore, better the softer the cantilever. The smallest force that can be detected with commercially available cantilevers is in the few pico Newton range. Assuming the molecule is bound at both ends, one on the surface and the other one on the tip, this system allows for stretching the suspended molecule with sub–nanometre precision. The forces acting on the molecule as it is extended are transmitted to the cantilever, causing it to bend. Generally the processes involved in such a kind of experiments are the detachment and the conformation changes of protein under investigation. Unfolding the HSA domain abruptly reduces the holding force because of an increase in the length of the extended protein, leading to the typical saw–tooth pattern in force–distance curves. This pattern represents a clear signature of the unfolding process. Besides unfolding, the mechanical forces applied to the molecule can lead also to dissociation. Dissociation on the other hand consists in the rupture of numerous bonds in series. The individual bonds dissociate and re–associate on a much faster timescale than that of the experimental pulling process and the stretching of the protein can no longer be observed. Instead of this, one observes a desorption plateau in the force–distance curve whose height reflects the equilibrium desorption force required to peel the protein off the surface.

In our measurements, after the first step jump, the cantilever remained at an almost constant deflection value. This behaviour was attributed by Friedman *et al.*[83] to the desorption of the HSA molecule from the underlying surface. At this stage, the protein molecule remains in the folded state and its conformation does not change, although some disconnection from the surface occurs. In the second step, which takes place at the same force value reported by Hinterdorfer *et al.*,[81] the force exerted by the tip suddenly swells the protein. A third step is very likely present between 30 and 40 nm but it partially overlaps the jump off contact. This step can be tentatively attributed to rupture of the covalent bond between HSA and the tip.

The swelling of the protein was performed by first approaching the HSA–functionalized tip to the surface and then by doing 25 approach–retrace cycles at 200 nm/s with 60 nm ramp size in order to acquire statistical significant data. Forces between surface and HSA–functionalized tip were monitored during force–distance cycles by moving the probe continuously up ("trace") and down ("retrace") at constant lateral positions. A typical unloading curve is presented in Fig. 96. This curve presented a first step probably because of the partial detachment of the protein from the surface, while the second saw–tooth step had the typical shape of the uncoiling process of proteins.

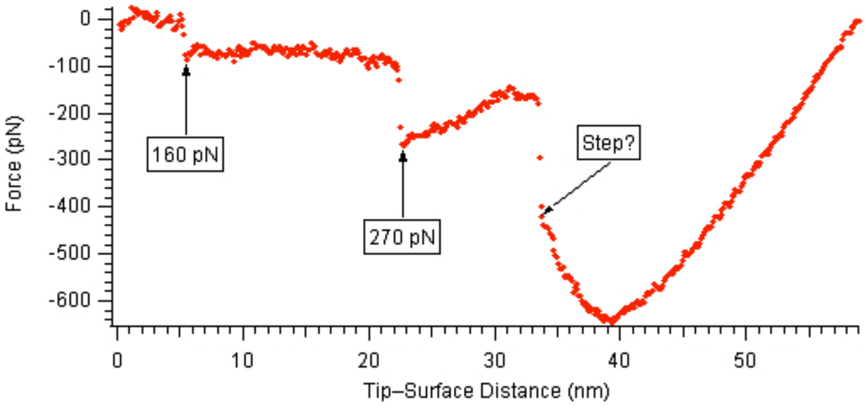

Fig. 96 – Unloading curve of the HSA protein swelling experiments. Arrows highlight the two steps at about 160 and 270 pN.

Several tests were performed in order to collect the data reported in Fig. 97. This figure shows two typical histograms of the measured forces and of the corresponding Gaussian fitting curves. The peaks are centred at 161 and 268 pN with ± 25 pN errors mainly attributable to thermal noise of the cantilever.

The force is not the only variable that can be measured from those experiments: also the energy involved into detachment and swelling of the protein can be accurately calculated. It is sufficient to integrate the force over the piezo displacement during the retracting curves. The energy dissipated in the first two steps is $4.35 \cdot 10^{-23}$ and $1.24 \cdot 10^{-22}$ kcal/molecule, that is about 26 and 75 kcal/mol. The energy implied in the second force jump corresponds to the energy needed by the protein to change from the folded to unfolded state.[81] The third step, whose presence remains to be confirmed, occurs at about 450 pN, that is at $2 \cdot 10^{-22}$ kcal/molecule or 125 kcal/mol that closely correspond to the energy of a carbon–carbon covalent bond (~ 100 kcal/mol).[84]

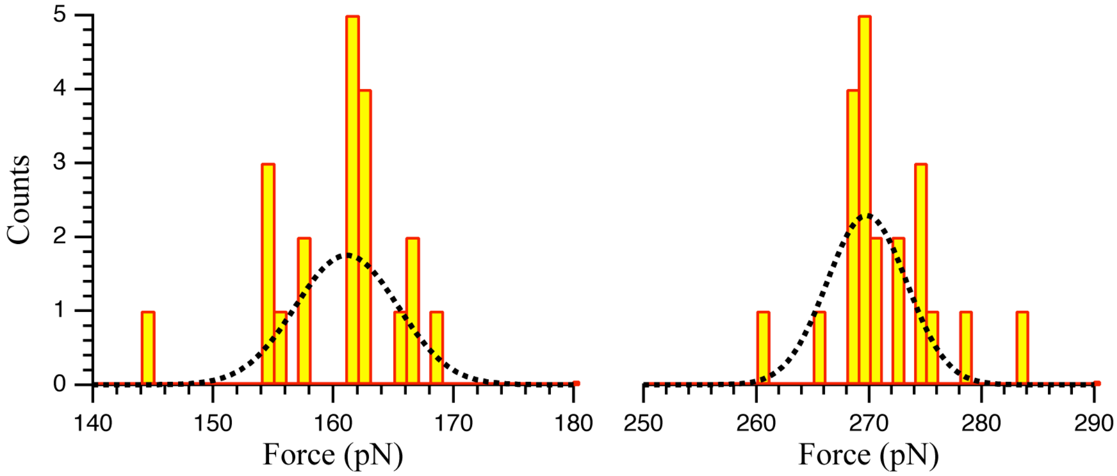

Fig. 97 – Histograms of the measured adhesion forces in albumin swelling.

5. CONCLUDING REMARKS

The exploitation of a new AFM instrument for the characterization of materials suitable for biomedical applications represented the main objective of the undertaken research project. The following points summarize the results achieved within the framework of the performed research activity.

- *AFM instrument*

  Selection, set–up, and preliminary testing of a commercial atomic force microscope represented the first task undertaken in the present thesis. It turned out that acquisition of medium quality topographic images of surfaces is an easy task that can be performed within a few days from the set–up. However, full exploitation of the instrument capabilities is an unceasing process of failures and achievements that is still ongoing. Exploration of the many theories underlying the different AFM techniques also constitutes a tough job. The lesson is that even the best commercial AFM are not yet routine instruments but still require dedication and skills for all but the most mundane tasks. On the other hand, understanding of AFM potential and limits might allow for performing tasks that were simply unbelievable before the advent of surface probe microscopy.

- *Phase imaging of oligopeptides*

  The bottom–up approach to the fabrication of supramolecular materials by self–assembly is gaining increasing interest because of its inherent simplicity and versatility. In particular, oligopeptides bearing oppositely charged side chains form three–dimensional matrices that might find application in the field of tissue engineering and in drug delivery practice. Accordingly, the self–assembling characteristics of selected oligopeptides were investigated by AFM techniques. Topography and even better phase imaging allowed for evaluating both the morphology and the distribution of oligopeptide aggregates. The collected information permitted to evaluate the dependence of the aggregation process on the oligopeptide concentration in the starting solution. Aggregate size and shape also depended on the presence of inorganic salts. Indeed, salt particles seem to act as nucleation centres promoting the onset and the growth oligopeptide aggregates. In spite of their preliminary character, the reported data clearly evidence that

AFM is a powerful method to study self–assembling materials at nanometre scale. Investigation of the conformational changes following self–assembly, and determination of the aggregation kinetics in solution represent possible future developments of this research line. Of course, investigation of a larger class of oligopeptides could help understanding the dependence of the aggregation process from structural parameters, such as the chemical constitution, charge distribution, steric hindrance, and hydrophilic–hydrophobic balance.

- *Mechanical analysis*

  Understanding of new materials at the molecular level has become increasingly critical for a new generation of nanomaterials for nanotechnology. In particular, the mechanical characterization of biomaterials is of outmost importance in the field of regenerative medicine. In order to exploit the potential of surface probe microscopy to evaluate the main mechanical characteristics of different materials at the nanoscale, the AFM was used as a nanoindentation device. Nanoindentation experiments were carried out on a selection of soft polymer samples, such as polystyrene and poly(methyl methacrylate), and hard materials like silicon and tungsten carbide. The conventional method for hardness calculation, which involves the direct observation of the residual contact area, led to relative large deviations from literature data. On the contrary, depth–sensing indentation, which utilises the depth of indentation h_c to calculate the material hardness and Young's modulus gave much better results. In all cases, more sound values were obtained on soft samples than on hard materials. Very likely, the use of diamond tips and super–stiff silicon cantilevers will afford more reasonable data also in the case of hard materials. In spite of these difficulties, the adopted technique allowed for determining not only the nanohardness and nanostiffness of the investigated materials, but also their dependence on the depth of indentation. However, application of different theoretical models and/or experimental conditions afforded dissimilar mechanical properties for the same sample. These results confirm that the use of AFM in applications other than topography still is more an art than a routine technique. Moreover, interpretation of nanoindentation data requires further theoretical foundation.

- *Protein swelling*

  Molecular interactions, such as protein–substrate and ligand–receptor interactions are of key importance for the function of living systems. Single–molecule force spectroscopy and binding force measurements show a growing potential for functional investigations of biomolecules and for the mechanical manipulation of single molecules. In this thesis, single–molecule force spectroscopy was applied successfully to study the uncoiling of human serum albumin. The functionalization of the AFM tip and of the support surface was successfully achieved by activation followed by application of a self–assembling reactive monolayer. The actual presence of the reactive surface layer was supported by different tests. Repeated chemical force microscopy experiments allowed for determining the energetic of the protein coiling–uncoiling process. The reported results are supported by the work of other authors. However, a typical plateau of polymer desorption from a surface was also observed. At present we are still working on theories to understand this occurrence. In any case, this investigation confirmed the wealth of information that can be gained by AFM chemical force spectroscopy, especially in the field of biological chemistry for the study of molecular recognition.

GLOSSARY

2D	Bi–dimensional
3D	Three–dimensional
A	Amplitude of cantilever oscillation
A_c	Residual contact area
AFM	Atomic Force Microscope
APTES	Aminopropyltriethoxysilane
b	Width of the cantilever beam
d	Minimum distance between two points resolvable by instrument
DSI	Depth Sensing Indentation
E	Young modulus
$E*$	Reduced Young modulus
$F_{\alpha\beta}$	Fourier map
F_L	Lateral / Torsional force acting on the cantilever
F_{ts}	Tip–surface forces
F_{WdV}	Wan der Vaals Force
F_Z	Transversal force acting on the cantilever
h	Thickness of the cantilever beam
H	Hardness
h_c	Depth of indentation during first part of unloading
h_f	Final indentation depth
h_{max}	Depth of indentation at maximum load P_{max}
HSA	Human Serum Albumin
I	Momentum of inertia
$\Im$	Imaginary unit $\sqrt{-1}$
I_i	Currents from various sections of the photodiode
k	Hooke's elastic constant
k_c	Cantilever elastic constant
k_s	Sample elastic constant
L	Length of the cantilever beam
$n_P(r)$	Atom density in the probe tip
$n_S(r)$	Atom density in the sample
P	Load over a surface
P_1	Apparent load
P_A	Adhesion
PBS	Phosphate Buffer Saline
PMMA	Poly(methyl methacrylate)
R	Tip radius
r_0	Equilibrium position in Lennard–Jones potential
Re	Reynolds number
RMS	Root mean square
R_q	Surface roughness
SEM	Scanning Electron Microscope
SNOM	Scanning Near field Optical Microscope
SPM	Scanning Probe Microscope

STM	Scanning Tunnelling Microscope
U_0	Energy at the minimum of Lennard–Jones potential
U_e	Elastic energy
U_{LJ}	Lennard–Jones potential
U_s	Surface energy
$w(x,t)$	Transverse displacement of the cantilever beam
α	Tip angle or damping coefficient
β	Tip angle
Γ	Hydrodynamic function
γ	Damping coefficient or tip angle
δ_c	Cantilever deflection
ΔI_L	Current proportional to the cantilever torsion under influence of lateral forces
ΔI_Z	Current proportional to the cantilever bend under influence of the force acting normally to the sample surface
δ_s	Sample deformation
Δz	Minimum detectable depression
η	Fluid viscosity
μ	Mass per unit of length
ρ_c	Cantilever density
ρ_f	Fluid density
ϕ	Phase shift
ω_0	Mechanical resonant frequency of cantilever in vacuum
ω_r	Mechanical resonant frequency of cantilever in air

REFERENCES

[1] A. S. Williams, J. P. Camilleri, R. M. Goodfellow, B. D. Williams *Br J Rheumatol* **35**, 719 (1996)

[2] D. F. Williams “Definitions in Biomaterials” *Proc Consensus Conf Eur Soc Biomat* Chester, England, March 3–5 1986, vol. 4, Elsevier, Amsterdam, NL (1987).

[3] G.M. Whitesides, J.P. Mathias, C.T. Seto *Science* **254**.1312, (1991)

[4] L. Pauling *Nature of the Chemical Bond and the Molecular Crystals: An Introduction to Model Chemistry* 3rd ed. Cornell University, Ithaca, NY (1960)

[5] S. Zhang *Biotechnol Adv* **20**, 339 (2002)

[6] I. Huc, J. M. Lehn *PNAS* **94**, 2106 (1997)

[7] J. Feltwell *The story of silk* Alan Sutton Publ., Phoenix Mill, UK (1990)

[8] S. Winkler, S. Szela, P. Avtges, R. Valluzzi, D. A. Kirschner, D. Kaplan *Int J Biol Macromol* **24** 265 (1999)

[9] P. B. Sigler, z. Xu, H. S. Rye, S. G. Burston, W. A. Fenton, A. L. Horwich *Ann Rev Biochem* **67**, 581 (1998)

[10] D. E. Morse *Trends Biotechnol* **17**, 230 (1999)

[11] S. Weiner, L. Addadi *Trends Biochem Sci* **16**, 252 (1991)

[12] S. Zhang, T. Holmes, C. Lockshin, A. Rich *PNAS* **90**, 3334 (1993)

[13] A. Aggeli, M. Bell, N. Boden, J. N. Keen, P. F. Knowles, T. C. McLeish, M. Pitkeathly, S. E. Radford *Nature* **386**, 259 (1997)

[14] A. Aggeli, I. A. Nyrkova, M. Bell, R. Harding, L. Carrick, T. C. B. McLeish, A. N. Somenov, N. Boden *PNAS* **98**, 11857 (2001)

[15] C. Bieri, O. P. Ernst, S. Heyse, K. P. Hofmann, H. Vogel *Nat. Biotechnol* **17**, 1105 (1999)

[16] S. Fernandez–Lopez, H. S. Kim, E. C. Choi, M. Delgado, J. R. Granja, A. Khasanov, K. Kraehenbuehl, G. Long, D. A. Weinberger, K. M. Wilcoxen, M. R. Ghadiri *Nature* **41**, 452 (2001)

[17] E. K. O’Shea, R. Rutkowski, P. S. Kim. *Science* **42**, 243 (1989)

[18] D. Baker, W. F. DeGrado *Curr Opin Struct Biol* **9**, 485 (1999)

[19] S. Zhang, T. Holmes, C. Lockshin, A. Rich *Proc Natl Acad Sci USA* **90**, 3334 (1993)

[20] S. Zhang, T.C. Holmes, C. M. DiPersio, R. O. Hynes, X. Su, A. Rich *Biomaterials* **16**, 1385 (1995)

[21] T. Holmes, S. Delacalle, X. Su, A. Rich, S. Zhang *PNAS* **97**, 6728 (2000)

[22] S. Zhang *Biotechnol Adv* **20**, 321 (2002)

[23] S. Zhang, A. Rich *PNAS* **94**, 23 (1997)

[24] M. Altman, P. Lee, A. Rich, S. Zhang *Protein Sci* **9**, 1095 (2000)

[25] S. Zhang, L. Yan, M. Altman, M. Lassle, H. Nugent, F. Frankel, D. A. Lauffenburger, G. M. Whitesides, A. Rich *Biomaterials* **20**, 1213 (1999)

[26] G.M. Whitesides, J.P. Mathias, C.T. Seto *Science* **254**, 1312 (1991)

[27] S. Vauthey, S. Santoso, H. Gong, N. Watson, S. Zhang *PNAS* **99**, 5355 (2002)

[28] J. Schwartz, S. Zhang *Curr Opin Mol Ther* **2**, 162 (2000)

[29] J. D. Hartgerink, E. Beniash, S. I. Stupp *Science* **294**, 1684 (2001)

[30] F. Giessibl *Rev Modern Phys* **75** (3), 949 (2003)

[31] G. Binnig, H. Rhorer *Phys Rev Lett* **50** (2), 120 (1983)

[32] G. Binnig, C. F. Quate, Ch. Gerber *Phys Rev Lett* **56**, 930 (1986)

[33] G. Meyer, N. M. Amer *Appl Phys Lett* **53**, 1045 (1988)

[34] C. Bustamante, D. Keller *Phys Today* **48** (12), 32 (1995)

[35] K. L. Johnson, K. Kendall, A. D. Roberts *Proc Royal Soc London Ser A* **324**, 301 (1971)

[36] B. V. Derjaguin, V. M. Muller. Y .P. Toporov *J Colloid Interf Sci* **53**, 314 (1975)

[37] D. Maugis *J Colloid Interf Sci* **150**, 243 (1992)

[38] V. M. Muller, V. S. Yushenko, B. V. Derjaguin *J Colloid Interf Sci* **92**, 92 (1983)

[39] G. Neubauer, S. R. Coben, G. M. McClelland, D. Horne, C. M. Mate, *Rev Sci Instrum* **61,** 2296 (1990)

[40] U. Stahl, C. W. Yuan, A. L. Delozanne, M. Tortonese *Appl Phys Lett* **65**, 2878 (1994)

[41] C. M. Mate, G. M. McClelland, R. Erlandsson, S. Chiang *Phys Rev Lett* **59**, 1942 (1987)

[42] T. R. Albrecht, P. Grutter, D. Rugar, D. P. E. Smith *Ultramicroscopy* **42–44**, 1638 (1992)

[43] O. Marti, J. Colchero, J. Mlynek *Nanotechnol* **1**, 141 (1990)

[44] D. Anselmetti, R. Lüthi, E. Meyer, H. J. Güntherodt *Nanotechnol* **5**, 87 (1994)

[45] F. J. Giessibl *Science* **267**, 68 (1995)

[46] Y. Martin, C. C. Williams, H. K. Wickramasinghe *J Appl Phys* **61**, 4723 (1987)

[47] Y. Martin, C. C. Williams, H. K. Wickramasinghe *J Appl Phys* **61**, 4723 (1987)

[48] Q. Zhong, D. Imniss, K. Kjoller, V. B. Elings *Surf Sci* **290**, L688 (1993)

[49] D. Anselmetti, R. Lüthi, E. Meyer, T. Richmond, M. Dreier, J. E. Frommer, H.–J. Güntherodt *Nanotechnol* **5**, 87 (1994)

[50] W. Han, S. M. Lindsay, T. Jing, *Appl Phys Lett* **69**, 4111 (1996)

[51] H. J. Butt, M. Jaschke *Nanotechnol* **6**, 1 (1995)

[52] J. E. Sader, *J Appl Phys* **84**, 64 (1998)

[53] R. W. Stark, W. M. Heckl, *Surf Sci* **457**, 219 (2000)

[54] T. Gotszalk, P. Grabiec, I. W. Rangelow *Ultramicroscopy* **82**, 39 (2000)

[55] I. Reviakine, , W. Bergsma–Schutter, A. Brisson *J Struct Biol* **121**, 356 (1998)

[56] E. Meyer, H. Heinzelmann, P. Grütter, Th. Jung, Th. Weisskopf H–R. Hidber, R. Lapka, H. Rudin, J. Güntherodt *J Microscopy* **152**, 269 (1988).

[57] G. S. Blackman, C. M. Mate, M. R. Philpott *Phys Rev Lett* 2270 (1990)

[58] H. A. Mizes, K.–G. Loh, R. J. D. Miller, S. K. Ahuja, E. F. Grabowski *Appl Phys Lett* **59**, 2901 (1991)

[59] E.–L. Florin, V. T. Moy, H. E. Gaub *Science* **264**, 415 (1994).

[60] H. W. Hao, A. M. Barò, J. J. Saenz, *J Vac Technol B* **9**, 1323 (1991)

[61] A. C. Fischer–Cripps *Nanoindentation* 1st ed., Mechanical Engineering Series, F.F. Ling ed., Springer–Verlag, New York, NY, p. 197 (2002)

[62] S. Turner "Creep of Polymeric Materials" in *Encyclopedia of Materials: Science and Technology*, Elsevier Science Ltd., Oxford, pp. 1813–1817 (2001)

[63] V. Domnich, Y. Gogotsi, S. Dub *Appl Phys Lett* **76**(16), 2214 (2000)

[64] T. F. Page, W. C. Oliver, C. J. McHargue *J Mater Res* **7**(2), 450 (1992)

[65] A. Gouldstone, H. J. Koh, K. Y. Zeng, A. E. Giannakopoulos, S. Suresh *Acta Mater* **48**, 2277 (2000)

[66] A. B. Mann, J. B. Pethica *Philos. Mag. A* **79**(3), 577 (1999)

[67] S. Zhang, C. Lockshin, R. Cook, A. Rich *Biopolymer* **34**, 663 (1994)

[68] B. C. Isenberg, J. Y. Wong *Mat Today* **9** (12), 54 (2006)

[69] B. Bhushan, "Nanomechanical Properties of Solid Surfaces and This Films", in *Handbook of Micro/Nano Tribology*, B. Bhushan ed., CRC Press, Inc.: Boca Raton, FL. p. 321–396 (1995)

[70] D. Tabor *The hardness of metals* Oxford Univ. Press: Oxford (1951)

[71] X. Li, B. Bhushan, *Mater Charact.* **48**, 11 (2002)

[72] J. L. Hutter *Langmuir* **21**, 2630 (2005)

[73] S. A.Tabor *Phys Proc Soc* **78**(2), 169 (1961)

[74] R. W. Armstrong, W. H. Robinson *New Zealand J Sci* **17**, 429(1974)

[75] M. F. Doerner, W. D. Nix *J Mat Res* **1**(4), 601 (1986)

[76] G. M. Pharr, W. C. Oliver, D. R. Clarke *J. Elect. Mate.* **19**, 881 (1990)

[77] I. N.Sneddon *Int. J. Engin. Sci..* **3**, 47 (1965)

[78] J. R. Tuck, A.M. Korsunsky, S. J. Bull, R. I. Davidson *Surf Coating Tech* **137**, 217 (2001)

[79] Support note from Balzer Gmbh

[80] B. Bhushan, B. K. Gupta *Handbook of Tribology: Materials, Coatings and Surface Treatments* Krieger, Malabar (1997)

[81] P. Hinterdorfer, W. Baumgartner, H. Gruber, K. Schilcher, H. Schindler *PNAS* **93**, 3477 (1996)

[82] H Gao, Y. Huang, W.D. Nix, J.W. Hutchinson *J. Mechan. Phys. Solids* **47**, 1239 (1999)

[83] C. Friedsam, M. Seitz, H.E. Gaub *J Phys: Condens Matter* **16**, S2369 (2004)

[84] J. March *Advanced Organic Chemistry*, 5th Ed., J. Wiley and Sons, New York, 1992